Thesis

# Dynamical and Statistical Properties on Desiccation Crack Pattern

Shin-ichi Ito

Department of Earth and Space Science,
Graduate School of Science, Osaka University

# Abstract

We investigate dynamical and statistical properties on desiccation crack pattern that we can observe when we make a mixture of water and powder desiccated. The statistical properties of the crack pattern vary slowly in general and depend on how we make the material desiccated. In other words, the statistical properties depend on time. In the previous studies, however, the time-dependent statistical properties have not been investigated so much, whereas the statistical properties of the pattern at the time when the paste is dried out have been extensively investigated. When we understand the properties of crack pattern and control the fragmentation, the time-dependent properties are significantly important.

To investigate the time-dependent statistical properties of the desiccation crack patterns, we design a continuum model based on the Kelvin-Voigt model, taking contraction into account. The contraction is described by a stress named "desiccation stress". The desiccation stress depends on time linearly. According to the numerical simulations of the continuum model by means of the smoothed particle hydrodynamics method, we realize the realistic time evolution of the crack patterns. By means of a clustering analysis, the time series of fragment areal size distribution and average areal size of fragments are obtained. The average size decays in inverse proportion to time. In addition, by scaling the size with the average size, the time series of fragment size distribution can be reduced to a time-independent curve as time passes. We call this property "dynamical scaling law" of fragment size distribution on desiccation crack pattern. To understand the scaling law, we remodel the continuum model into a stochastic model named "modified Gibrat process" on the basis of the Gibrat model. The modified Gibrat process is constructed by introducing the lifetime of a single fragment into the Gibrat process. The lifetime is derived analytically and numerically as a function of the fragment size. In general, the lifetime is described by an inverse function of the desiccation stress. According to the numerical simulations, the modified Gibrat process reproduces the dynamical scaling law when we choose a power function as the lifetime. The modified Gibrat process is markovianized in order to investigate it analytically, and then we obtain a master equation. According to the scaling analysis of the master equation, we find that the scaling law is realized only in the case that the desiccation stress is given by a power function. Furthermore, we carry out the actual experiments of the desiccation crack patterns to compare with our theoretical results. As a result, we confirm that the size distribution obeys the dynamical scaling just like our theoretical results.

# Contents

# Chapter 1

# Introduction

Material fracture is a familiar phenomenon to us and it can be widely observed in various situations: fragments of a broken glass cup, desiccation crack of a paddy field in a drought, and so on. The fracture occurs by the various causes and involves the complicated dynamics. The patterns owing to the fracture are also various and depend on the properties of material and the external conditions: For example, a glass crack pattern owing to a collision which looks like a spider web, a gigantic columnar joint that appears when lava cools and solidifies, a cell crack pattern of a paddy field in a drought, and so on. The various crack patterns are attractive to researchers and have been investigated by many researchers.

Fragmentation processes are ubiquitous and significantly important phenomena for the fields of physics, chemistry, and biology [1–22]. In order to understand the behavior, the statistical properties, for instance, size distribution of fragments, are often investigated. The statistical properties are the macroscopic properties. What determines the macroscopic properties? This is an important question when we try to understand the properties and control the fragmentation. The statistical mechanics suggests the macroscopic properties are determined by the microscopic properties. Microscopic property is the property of elementary process. Thus all we have to do to know and understand the statistical properties is to know the elementary process.

There is the collision process widely observed. In the collision process, the collided materials may break into the fragments. The sizes of the fragments distribute, and the size distribution is often investigated for understanding the elementary process. There are many experimental and theoretical studies for the collision process [1–9, 23–30]. There is also the fragmentation process owing to the contraction [13–22, 31–40]. The fragmentation process of desiccation crack pattern [13–22, 37–40] is one of example. The sizes of the fragments also distribute; However, the size distribution has not been investigated well in

spite of the importance for the understanding the elementary process. In this chapter, we review various kind of material fragmentations and the statistical properties.

## 1.1 Fragmentation owing to collision

When we apply shock to a material or collide two materials, the material fragments. This phenomenon can be observed universally around us. When we drop or throw a material to another material, the materials breaks if it has an enough momentum. When we break the materials, the size of fragments is believed to distribute in the two typical distribution roughly.

### 1.1.1 Lognormal law

The first of the categories of characteristic distributions is a lognormal distribution [9, 41–43]. This is observed when we breaks the material with weak shock. Ishii and Matsushita [9] performed the experiment of dropping long, thin glass rods. If the falling height is lower, the size distribution of broken glass rods can be described by the lognormal distribution. However, with increasing the falling height, the size distribution of broken glass rods can be described by the power-law distribution.

The physical background of the reason why the lognormal distribution appears can be explained by the Gibrat process [44]. In the Gibrat process, the fragments are subdivided like a cascade (see Fig. 1.1). Let $S$ denote a size of a fragment. It represents the length of a rod in this case. The fragment breaks in every stage. When the fragments go to the next stage, the fragment breaks into two pieces with the dividing ratio $r$. In order to conserve the fragment size in the event, $r$ takes the value between 0 and 1. $r$ is chosen from a given probability density function $g(r)$. Let us focus on a dividing history of a certain fragment. Let $S_n$ and $r_n$ denote the size and dividing ratio on $n$-th stage of a certain fragment, respectively. Immediately, it is found that $S_n$ is given by

$$S_n = S_{n-1} \times r_{n-1} = \cdots = S_0 \Pi_{i=0}^{n-1} r_i. \tag{1.1}$$

Here let us change a variable into $Z_i = \log(S_i/S_0)$. Then Eq. (1.1) is rewritten to

$$Z_n = \sum_{i=0}^{n-1} \log r_i. \tag{1.2}$$

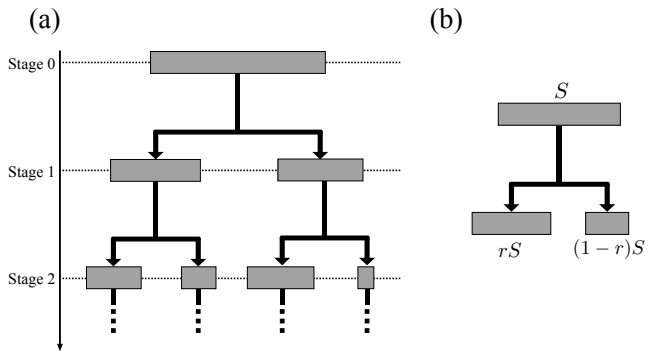


Figure 1.1: Schematic diagram of the Gibrat process. (a) shows the flow of process. Starting with one fragment at stage 0, the fragment breaks into two pieces every stage. (b) shows the elementary subdividing process. A fragment is subdivided into two pieces with the dividing ratio $r$. Namely, a fragment with the size $S$ is subdivided into fragments with the sizes $rS$ and $(1-r)S$.

After enough stages passes, it is found that $Z$ distributes normally and the average $E_n$ and variance $V_n$ are given by

$$E_n = nm, \tag{1.3}$$

and

$$V_n = ns^2, \tag{1.4}$$

respectively, according to the central limit theorem. Here $m$ and $s^2$, are defined as follows:

$$m = \int dr g\left(r\right) \log r, \tag{1.5}$$

and

$$s^2 = \int dr g\left(r\right) \left(\log r\right)^2 - m^2. \tag{1.6}$$

Using Eqs. (1.3) and (1.4), it is found that the fragment size $S$ obeys the following lognormal distribution as

$$P\left(S, n\right) \sim \frac{S_0}{\sqrt{2\pi n s^2} S} \exp\left[-\frac{\left(\log\left(S/S_0\right) - nm\right)^2}{2ns^2}\right], \tag{1.7}$$

where $P(S, n)$ denotes the probability density function of the size $S$ existing at the stage $n$. This is called the Gibrat law. The average size $\langle S \rangle =$

$\int_0^\infty dS\ SP(S,n)$ becomes the exponential function of $n$ as $\langle S\rangle = S_0 \exp\left[n\left(m + s^2/2\right)\right]$. Remarkably, Eq. (1.7) does not contain the functional form of $g\left(r\right)$ explicitly. This result suggests that all fragmentation processes following the Gibrat process which have common $m$ and $s^2$ make a common functional form of size distribution.

### 1.1.2 Power law

The second type of the fragment distribution is a power-law distribution which is described by

$$C\left(S\right) \sim S^{-b}, \tag{1.8}$$

where $C(S)$ denotes the cumulative distribution function of the size $S$, and $b$ is a constant value characterizing the power law. This is observed generally when we breaks the material with strong shock [1–8]. Ref. [9], which is referred to as an example that the size distribution can be described by the lognormal distribution, also shows that the size distribution of glass rods can be described by the power-law distribution in the case that the rods are fallen from the higher height. Namely, Ref. [9] shows the transition between the lognormal law and the power law in the size distribution. The size distribution of the Itokawa regolith particles also follows the power law [12]. Some numerical simulations of the material collision have been carried out and obtained the power law of the size distribution [23–30, 45]. The direct numerical simulation of the brittle continuum material which breaks due to the shock wave is performed, and the size distribution of the fragments follows the power law [25].

Some statistical models reproducing the power law in the fragmentation were proposed [46, 47]. Yamamoto and Yamazaki [47] proposed a stochastic model by modifying the Gibrat process. In their model, the fragment ceases fracture with a constant probability $p$. Then the model reproduces the power law with the constant exponent $b$ $(0 < b < 1)$. In the model, $b$ is calculated exactly as a function of $p$ and the probability density function of dividing ratio $g(r)$. In addition, they proposed the stochastic model in which the fragment ceases fracture with a probability $p(S)$ that depends on the fragment size $S$ and is given by

$$p(S) = \begin{cases} \left(\frac{\tilde{S}}{S}\right)^a, & \text{for} \quad S \geq \tilde{S} \\ 1, & \text{for} \quad S < \tilde{S}, \end{cases} \tag{1.9}$$

where $\tilde{S}$ denotes a characteristic size and $a$ denotes a positive constant. The model shows the power law of cumulative distribution function in which $b =$

$1 + a$, which is independent of $g(r)$. In the Ishii's experimental study [9], the functional form of the fragment size distribution in the experiment of the fracture of glass rods depends on the falling height; When the glass rods is fallen from the lower (higher) height, the size distribution is the lognormal (power-law) distribution, respectively. Yamamoto and Yamazaki [47] suggested the reason why the functional form of size distribution depends on the falling height may be explained as follows: The falling height corresponds to the impact energy injected at first. If the impact energy is smaller, a fracture process corresponds to a cascade limited to the first several stages, because $S$ does not become smaller than $\tilde{S}$, then $p(S)$ becomes almost zero.

The power-law of size distribution appears on not only fragmentation process but also various phenomena: the word frequency (Zipf's law) [48], the family name frequency [49–52] , the size distribution of population [53], the size distribution of magnitude of earthquake (Gutenberg-Richter law) [54–56], the size distribution of number of access to website [57], and so on.

Yamamoto and Yamazaki have reproduced the power-law of the size distribution of the material fragmentation by modifying the Gibrat process. The Gibrat process is convenient for describing the material fragmentation, and it has been applied for not only the material fragmentation but also other phenomena [58–60].

## 1.2 Fragmentation owing to contraction

The fragmentation process owing to contraction is observed in the desiccation cracking process as shown in Fig. 1.2. The desiccation crack pattern can be observed on lakes or paddy fields suffering a drought. The fracture develops relatively slower than the fracture owing to the collision. Because of slow development of fracture, the dynamics of crack pattern may be affected by the external environment. Thus the statistical properties also may be affected by the external environment. The desiccation crack pattern of the mixture composed of liquid and powder, which is called paste, is classified into the two types; The difference appears in the spatial structure of crack. The crack runs on the surface of the paste. In addition to the horizontal crack, when the thickness is larger than the linear dimension of the top surface, the crack also grows slowly from the top surface toward the bottom of container, and makes the prismal structure [31–36] just like the columnar joint [61]. Another type of crack structure can be observed when the thickness is smaller than the linear dimension of the top surface. In this case, the crack immediately approaches to the bottom, and the columnar structure does not form. This type of crack can be observed in the paint or the thin mud crack. The crack growth is affected

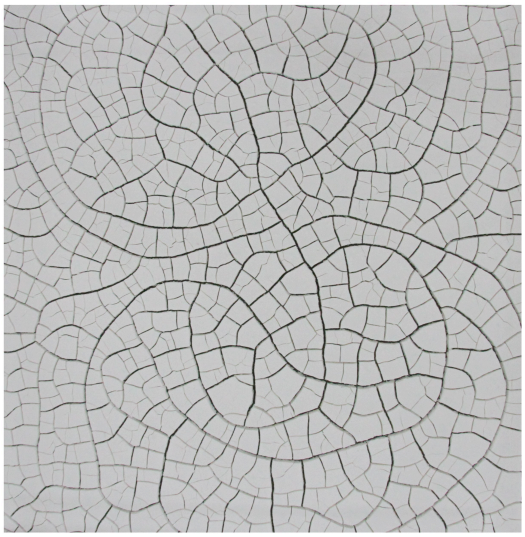

Figure 1.2: A typical desiccation crack pattern of the mixture composed of water and powder of magnesium carbonate hydroxide.

by the friction owing to the sticking to the substrate because the thickness is thin. The peeling of the material from the substrate can be observed.

In this study, we focus on the later case. There are many studies for such desiccation crack patterns. However, it seems that most of the experimental investigations on them have focused on the final state of the drying paste. We review the studies of desiccation crack pattern in this section.

### 1.2.1 Statistical property

Some statistical properties of desiccation crack pattern are reported by Refs. [13–22]. Groisman and Kaplan [13] reported the experimental study of desiccation crack pattern using the thin layer of the paste composed of water and coffee powder. The average of fragment area observed from top of the surface is proportional to the square of the paste thickness of the layer (see Fig. 1.3). Namely, the linear dimension of fragment size of top surface is proportional to the paste thickness. The authors suggested that the reason can be explained as follows: The inner stress required to make crack is originated from the resistance owing to the friction on the bottom against the contraction. The spatial stress distribution should be maximal at the center of the fragment. The maximum stress $\sigma$ is described by the ratio of stretching force $f$ acting on the unit length to the paste thickness $d$, $\sigma \sim f/d$. The stretching force is the resistance owing to the friction on the bottom; Therefore it should be roughly proportional to the linear dimension of the fragment areal size $l$ in the direction of the force, $f \sim l$.

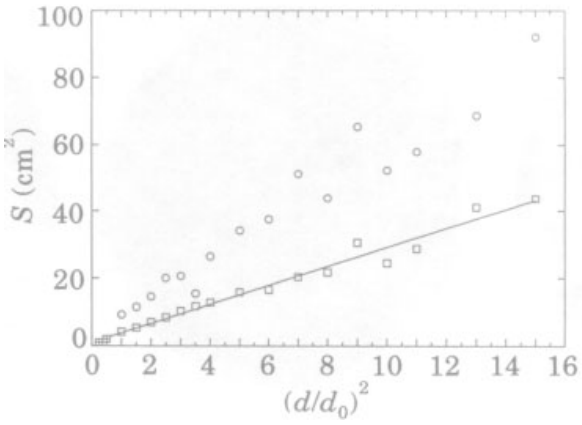


Figure 1.3: The paste thickness dependency of the average areal size of fragments on the final crack pattern of the paste of coffee powder. The circle indicates the maximal size of fragment in the final crack pattern. The square indicates the average size on the final crack pattern. The vertical axis indicates the size. The horizontal axis indicates square of the paste thickness $d$ normalized by $d_0 = 4$ mm. This figure is taken from Ref. [13] with permission of EPL (Europhysics Letters).

Thus, the stress in this direction is $\sigma \sim l/d$. Therefore, the length $l_{cr}$ required to provide the critical stress $\sigma_{cr}$ under which the material breaks is proportional to $d$, $l_{cr} \sim \sigma_{cr} d$. The fragmentation process must finish when the linear dimensions of the fragment sizes become less than $l_{cr}$. Therefore the linear dimension of fragment size should have the linear relation with the thickness of the paste. Furthermore, they investigated the inner angle distribution which characterizes the shape of fragment (see Fig. 1.4) in Ref. [13]. It is reported that the inner angle distributes between $70° \sim 120°$ and the center of the distribution is at $93.1° \pm 8°$. Namely the shape of the fragment is nearly convex polygon. Colina and Roux [15] performed the experiment of desiccation crack pattern of the clay paste desiccated in a square container with dimensions of $L \times L$. They investigated the relationship between the characteristic length of fragments in the final pattern, $\Phi_f$, and the ratio $L/d$, where $d$ denotes the thickness of the paste. The result is that the relationship is given by, $\Phi_f/d = A + K \exp(-cL/d)$, where $A$, $K$, and $c$ are dimensionless constants, and then it implies that the final size of fragment depends on not only the thickness of the paste but also the horizontal size of the system. The few studies of the size distribution of the desiccation crack patterns is reported [17]. Lecocq and Vandewalle [17] carried out the experiment of quasi one dimensional desiccation crack pattern. They disposed the clay paste in a long rectangular polyhedral container and

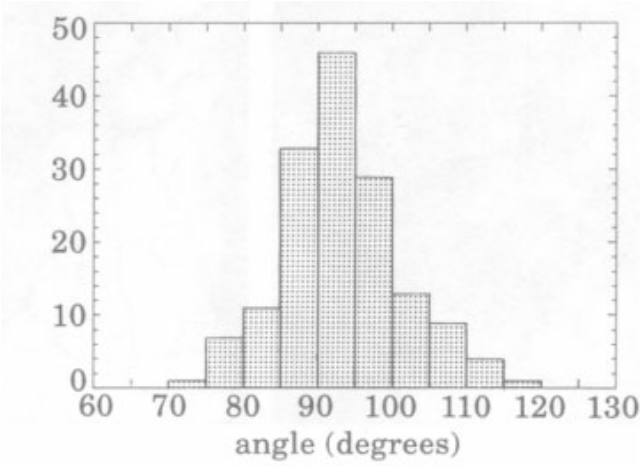


Figure 1.4: A typical distribution of inner angles of polygonal fragment. The thickness is about 6 mm when the paste is dried out. This figure is taken from Ref. [13] with permission of EPL (Europhysics Letters).

obtained the size distribution shown in Fig. 1.5. The size distribution was evaluated by the two fitting functions, a lognormal distribution and the Weibull distribution [62]:

$$P(S) = c\beta S^{\beta-1} \exp\left(-cS^{\beta}\right), \tag{1.10}$$

where $c$ and $\beta$ are the fitting parameters, respectively. The both functions can fit the experimental data well; Therefore, the authors did not conclude the functional form of the size distribution.

### 1.2.2 Memory effect

Some kind of paste remembers the direction of dynamical motion by the external field, such as vibration and flow suffering before the desiccation, as the desiccation crack patterns. Nakahara and Matsuo [37, 38] reported the paste, which is composed of water and powder of calcium carbonate, imprints the force that the paste is received before the desiccation on the crack pattern; If the paste of calcium carbonate is vibrated before dried, the cracks run firstly in the direction perpendicular to the direction of the force of vibration before the appearances of cracks parallel to the force direction. Whether the memory is remained or not corresponds to whether the shear stress owing to the vibration exceeds the yield stress of the paste, which depends on the volume fraction of the calcium carbonate powder. This phenomenon is called type-I memory effect. The theoretical studies for the type-I memory effect are reported in Refs. [39, 40]. The Bingham plasticity [63] is assumed in the both

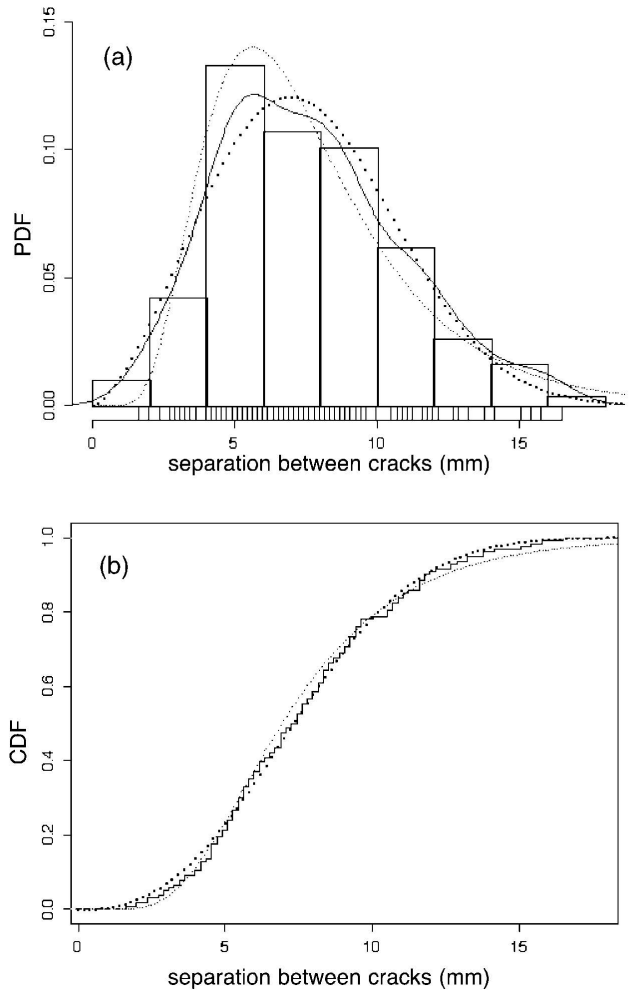


Figure 1.5: The size distribution of quasi one dimensional desiccation crack pattern. The top figure corresponds to the probability density function of fragment size (i.e., separation between cracks). The bottom figure corresponds to the cumulative distribution function of fragment size. This figure is taken from Ref. [17] with permission of Springer (The European Physical Journal E).

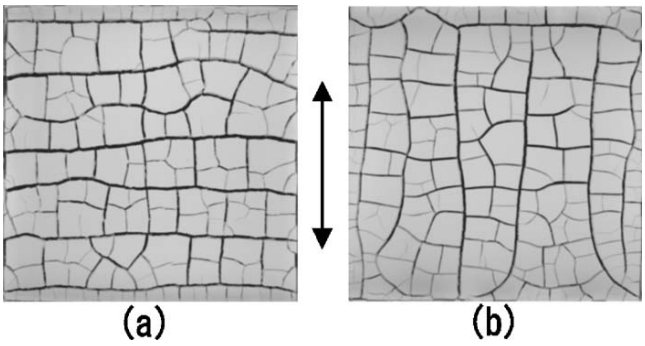


Figure 1.6: The crack patterns resulting the memory effect in the desiccated paste of the magnesium carbonate hydroxide. The double-headed arrow at the center of figure indicates the direction of the vibration before the desiccation. (a) and (b) indicate the type-I pattern and the type-II pattern, respectively. This figure is taken from Ref. [64] with permission of Physical Review E.

studies. The plasticity basically causes the memory of force. In these theories, the mechanism that the memory is remained is assumed to be owing to the strong viscosity in Ref. [39] or the nonlinearity of strain in Ref. [40]. In addition, Ref. [64] reported that the paste, which is composed of water and powder of magnesium carbonate hydroxide, can imprint not only the direction of the vibration that the paste is received before the desiccation but also the direction of the flow on the crack pattern. When the paste is vibrated, the surface flow appears if the volume fraction of the powder is small. According to the surface flow, the crack runs firstly in the direction parallel to the direction of the the surface flow. This type of crack is called type-II memory effect. Depending on the acceleration of the vibration or the volume fraction of the magnesium carbonate hydroxide, the paste of magnesium carbonate hydroxide can show both the type-I memory effect and the type-II memory effect. There is no theoretical study for the type-II memory effect.

### 1.2.3 Numerical simulation

Some numerical studies for reproducing the desiccation crack pattern were carried out [22,65–70]. Kitsunezaki [65] reported that the analysis of the model of crack in the desiccated mud layer. In this model, the layer is described by a two dimensional viscoelastic continuum sticking on the ground. The viscoelasticity is described by the Kelvin-Voigt model [71]. The sticking force is described by the force proportional to the displacement field. In addition to the sticking effect, the slipping displacement on the bottom of the layer is taken into ac-

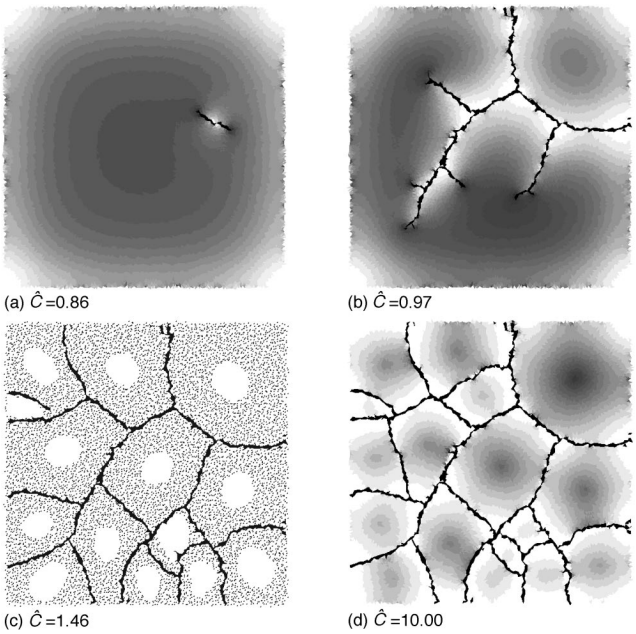


Figure 1.7: The time evolution of the crack pattern of the model of the desiccated mud layer. $\hat{C}$ describes the increasing stress induced by the evaporation of the inner liquid, and the value of $\hat{C}$ corresponds to the elapsed time. The gray scale in (a), (b), and (d) indicates the energy density field. The dots in (c) indicate the slipping element. This figure is taken from Ref. [65] with permission of Physical Review E.

count. In order to describe the contraction owing to the desiccation, the linear increasing function is introduced in the diagonal part of the elastic stress. The continuum model is described by the energy density field including the elastic energy and the energy owing to the sticking. The author have carried out the numerical simulations of the continuum model discretized into a random triangular lattice and obtained the time evolution of the crack pattern as shown in Fig. 1.7. The author has reported that the growth of the crack pattens exhibits qualitative differences depending on the elastic constants and relaxation time of the Kelvin-Voigt model. When the relaxation time is smaller, the growth of the fingering patterns with the tip splitting have been observed rather than the growth of the side branching cracks. Kitsunezaki [70] performed the numerical simulation of the spring network model introducing the plastic strain and investigated the effects of increasing negative pore pressure owing to the evaporation of the inner water and plastic deformation on crack growth. In desiccation, a thin layer of paste may be observed to crack while it remains attached to the substrate, or alternatively it may peel off the substrate first instead of cracking. Sadhukhan *et al.* [69] carried out the numerical simulation of a two dimensional spring model in order to investigate the competition between cracking and peeling, and obtained the phase diagram showing the cross-over from the peeling to the cracking, depending on the breaking threshold of the spring attached to the substrate and the time scale characterizing the propagation speed of the desiccation from the top surface toward the bottom.

## 1.3 Purpose of the study

As we reviewed in the previous part of this chapter, there are many studies of the fragmentation process. Especially, the studies of the desiccation crack pattern are carried out by many researchers. However, the studies of the statistical properties of the desiccation crack pattern when the material is desiccating are few, whereas the studies of the statistical properties of the crack pattern dried out exist richly. The statistical properties of desiccation crack pattern dried out are determined by the statistical properties when the paste is desiccated. Namely, we can not understand the statistical properties of desiccation crack pattern dried out without the understanding the time dependent statistical properties. There are few studies focusing on the time dependent statistical properties of the desiccation crack patterns in spite of the importance. The time dependent properties may enable us to predict the future statistical properties. For this reason, the investigation of the time dependent statistical properties is significantly important. This study contributes for helping us to understand the dynamics of the desiccation crack patterns and discovering new properties.

The purpose of this thesis is to understand the dynamical and statistical properties of the desiccation crack pattern. In order to achieve the purpose, we carry out the following investigations.

### 1.3.1 Reproduction of the desiccation crack pattern

We reproduce the realistic desiccation crack patterns and investigate the statistical properties. In order to reproduce the realistic pattern, we carry out the simulations of desiccation crack patterns. We propose a simple continuum model of desiccating and cracking paste on the basis of the elastic theory. Furthermore, we investigate the statistical properties of the patterns. We investigate the time evolution of crack pattern, the time evolution of the average size of fragments, and the time series of the size distribution of fragments.

### 1.3.2 Origin of the statistical properties

We investigate the statistical properties of the desiccation crack patterns, which are obtained by the simulations of continuum model. The direct simulation of the material fragmentation using the continuum model is straightforward for describing the crack pattern; However, it is difficult to understand the origin of the statistical properties. That is because the fragmentation process of the continuum model involves the complicated dynamics. Therefore we structure a theory describing the fragmentation process of the desiccation crack pattern as a stochastic model. The stochastic model will enable us to investigate the statistical properties theoretically. In order to construct the stochastic model, we have to investigate the dynamics of the fragment of the paste being desiccated, because the dynamics are related with the elementary process of the desiccation crack pattern. When the fragmentation progresses, there are many isolated fragments. If we were to investigate the dynamics of an isolated fragment theoretically and then construct a stochastic model, we could understand the origin of the statistical properties of the desiccation crack pattern.

### 1.3.3 The properties on the actual desiccation crack pattern

We carry out actual experiments of desiccation crack patterns. The purpose is to investigate the statistical properties of experimental desiccation crack pattern. The time-dependent statistical properties of desiccation crack pattern have not been investigated well. Therefore this study is significantly important for understanding the origin of the statistical properties. A paste composed of

water and powder of magnesium carbonate hydroxide is used for the experiment. The time evolution of crack pattern is taken by an interval photography and analyzed by an image processing. By the image processing, we investigate the time evolution of the areal size distribution and the time evolution of the average areal size. Comparing the experimental results with the theoretical results, the validity of the theory is discussed.

## 1.4 Outline of this thesis

This thesis is organized as follows: In Chapter 2, we propose a continuum model which reproduces a realistic desiccation crack patterns and investigate the statistical properties of the crack pattern. The continuum model is based on the three dimensional Kelvin-Voigt model and is approximated to a quasi two dimensional model in order to be simplified for the computation. The smoothed particle hydrodynamics method is used for solving the equations of continuum model. By using the crack patterns we obtained by the computation, we investigate the time evolution of fragment size distribution and average size of fragments. In Chapter 3, we remodel the continuum model into a stochastic model in order to express the time dependent properties of the statistical quantities obtained by the simulation of continuum model. The stochastic model is based on the Gibrat process because it is convenient for describing the fracturing process statistically. The dynamical properties of a single specimen are investigated and are introduced into the Gibrat process. In Chapter 4, we carry out the actual experiments of desiccation crack patterns and analyze it by using an image analysis in order to compare with our theoretical results. Chapter 5 summarizes the results of this study and concludes this thesis.

# Chapter 2

# Continuum model

In this chapter, we investigate the time-dependent statistical properties of desiccation crack patterns by the numerical simulation. First, we propose a three dimensional continuum model on the basis of the continuum theory. The stress equation used in the model is based on the Kelvin-Voigt model and is composed of the elastic term, viscous term, and contraction term. The contraction term corresponds to the effect of the evaporation of inner liquid from the top surface. Next, we approximate the three dimensional model into the thin layer model which can be regarded as the quasi two dimensional model in order to reduce the calculation cost. The quasi two dimensional model is calculated by using the smoothed particle hydrodynamics method [72–78]. The smoothed particle hydrodynamics method belongs to the Lagrangian method, in which the calculation point can migrate with following the velocity field, and is expected to be able to capture the complicated migration of crack; The cracks are reproduced by the removal of the calculation point at which the stress exceeds the yield stress. Finally, we investigate the time-dependent statistical properties, such as the time evolution of average size and the time series of size distributions. [1]

## 2.1 Basic equations

Let us start with a thin layer of paste with thickness $H$. The surface is a rectangular with dimensions of $L_x \times L_y$ as shown in Fig. 2.1. The paste sticks on the bottom of the vessel. We take $z = 0$ as the bottom.

[1] Section 2.4, 2.5, 2.6, 2.7, and 2.8 in this chapter are taken from Ref. [79] with the appropriate modifications. The parts we take from Ref. [79] are copyrighted materials of APS.

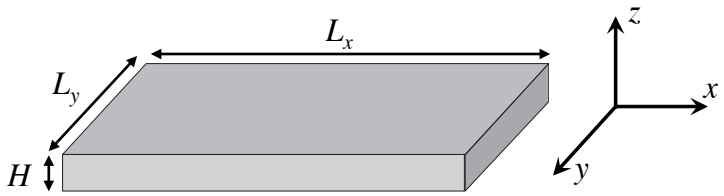


Figure 2.1: The schematic view of the paste. The geometry of the paste in simulation is a rectangular parallelepiped with dimensions of $L_x \times L_y \times H$.

### 2.1.1 Equations

Let $\boldsymbol{v} = (u_x, u_y, u_z)$, $\boldsymbol{u} = (u_x, u_y, u_z)$, $\rho$ and $\boldsymbol{\sigma} = \begin{pmatrix} \sigma_{xx} & \sigma_{xy} & \sigma_{xz} \\ \sigma_{yx} & \sigma_{yy} & \sigma_{yz} \\ \sigma_{zx} & \sigma_{zy} & \sigma_{zz} \end{pmatrix}$ denote the velocity field, the displacement field, the density and stress field, respectively. The equation of motion, the continuity equation, and the relation between displacement and velocity of a three dimensional continuum are described as follows:

$$\rho \frac{d\boldsymbol{v}}{dt} = \nabla \cdot \boldsymbol{\sigma}, \tag{2.1}$$

$$\frac{d\rho}{dt} = \rho \nabla \cdot \boldsymbol{v}, \tag{2.2}$$

$$\frac{d\boldsymbol{u}}{dt} = \boldsymbol{v}, \tag{2.3}$$

where $\dfrac{d}{dt} = \dfrac{\partial}{\partial t} + \boldsymbol{v} \cdot \nabla$ is a time differential operator in the Lagrangian description. In addition to Eqs. (2.1), (2.2) and (2.3), the constitutive equation of $\boldsymbol{\sigma}$ is required to close the equations.

### 2.1.2 Boundary conditions

In order to solve the equations, the boundary conditions are required. The paste sticks on the bottom and has the free surfaces. Therefore the boundary conditions are described by

$$\boldsymbol{\sigma} \cdot \boldsymbol{n} = \boldsymbol{0} \qquad \text{at the free surfaces,} \tag{2.4}$$

and

$$\boldsymbol{u} = \boldsymbol{v} = \boldsymbol{0} \qquad \text{at the bottom,} \tag{2.5}$$

where $\boldsymbol{n}$ denotes a normal vector at the free surfaces.

## 2.2 Constitutive equation

To describe the property of desiccating paste, the constitutive equation of stress is determined. In this study, we use the Kelvin-Voigt model modified to describe the effect of desiccation. Our modified Kelvin-Voigt model consists of three terms:

$$\boldsymbol{\sigma} = \boldsymbol{\sigma}_{\mathrm{el}} + \boldsymbol{\sigma}_{\mathrm{vis}} + \boldsymbol{\sigma}_{\mathrm{dry}}, \tag{2.6}$$

where $\boldsymbol{\sigma}_{\mathrm{el}}$, $\boldsymbol{\sigma}_{\mathrm{vis}}$ and $\boldsymbol{\sigma}_{\mathrm{dry}}$ denote the elastic, viscous and desiccation terms.

### 2.2.1 Elasticity

$\boldsymbol{\sigma}_{\mathrm{el}}$ represents the elastic term. According to the generalized Hooke's law, $\boldsymbol{\sigma}_{\mathrm{el}}$ is described by

$$\boldsymbol{\sigma}_{\mathrm{el}} = \lambda \mathrm{Tr}\left(\boldsymbol{\epsilon}\right) \boldsymbol{I} + 2\mu\boldsymbol{\epsilon}, \tag{2.7}$$

where $\lambda$ and $\mu$ denote the first and second Lamé constants, respectively. $\mathrm{Tr}\left(\boldsymbol{A}\right)$ describes a trace of tensor $\boldsymbol{A}$. $\boldsymbol{\epsilon}$ is the strain tensor given by

$$\boldsymbol{\epsilon} = \frac{1}{2}\left(\nabla \otimes \boldsymbol{u} + \nabla \otimes \boldsymbol{u}^T\right), \tag{2.8}$$

where $\otimes$ describes a tensor product and $\boldsymbol{A}^T$ means the transpose tensor of $\boldsymbol{A}$. Alternatively, instead of Eq. (2.7), we can also use the time derivative form of $\boldsymbol{\epsilon}$ that is given by

$$\frac{d\boldsymbol{\sigma}_{\mathrm{el}}}{dt} - \boldsymbol{\Omega} \cdot \boldsymbol{\sigma}_{\mathrm{el}} + \boldsymbol{\sigma}_{\mathrm{el}} \cdot \boldsymbol{\Omega} = \lambda \mathrm{Tr}\left(\dot{\boldsymbol{\epsilon}}\right) \boldsymbol{I} + 2\mu\dot{\boldsymbol{\epsilon}}, \tag{2.9}$$

where $\dot{\boldsymbol{\epsilon}}$ and $\boldsymbol{\Omega}$ denote the strain rate tensor and spin tensor given by

$$\dot{\boldsymbol{\epsilon}} = \frac{1}{2}\left(\nabla \otimes \boldsymbol{v} + \nabla \otimes \boldsymbol{v}^T\right), \tag{2.10}$$

and

$$\boldsymbol{\Omega} = \frac{1}{2}\left(\nabla \otimes \boldsymbol{v} - \nabla \otimes \boldsymbol{v}^T\right). \tag{2.11}$$

The left-hand side in Eq. (2.9) describes the Jaumann stress rate [76]. Jaumann stress rate is an objective stress rate. It originates from the removal of the effect of rigid rotations. Usefulness of Eq. (2.9) is that we do not need to compute the strain tensor.

### 2.2.2 Viscosity

$\boldsymbol{\sigma}_{\text{vis}}$ represents the viscous term. We simply assume $\boldsymbol{\sigma}_{\text{vis}}$ is described by the Newtonian friction as

$$\boldsymbol{\sigma}_{\text{vis}} = \eta \dot{\boldsymbol{\epsilon}}, \tag{2.12}$$

where $\eta$ denotes a viscosity coefficient.

### 2.2.3 Desiccation

$\boldsymbol{\sigma}_{\text{dry}}$ represents the desiccation term. Desiccation enhances the inner stress. That is because the loss of water content due to the evaporation generates the negative hydrodynamic pressure. $\boldsymbol{\sigma}_{\text{dry}}$ describes this effect. When the material is desiccated uniformly, $\boldsymbol{\sigma}_{\text{dry}}$ is a function independent of the coordinate but it depends on time. The function must be an increasing function to describe the effect of desiccation. In consequence, $\boldsymbol{\sigma}_{\text{dry}}$ is given by

$$\boldsymbol{\sigma}_{\text{dry}} = F(t)\boldsymbol{I}, \tag{2.13}$$

where $F(t)$ denotes an increasing function of time. In the previous works, $F(t)$ is often given by a linear or exponential function [22, 39, 65–70].

### 2.2.4 Contribution of the three stresses

These stresses describe the basic property of a desiccating paste. Some model including the effect of plastic strain have been proposed [39, 70]. However the effect of plastic strain is not necessary to reproduce a simple desiccation crack pattern. The three stresses contribute toward reproducing the crack pattern as follows: When a viscous paste is fractured, it is expected that there is few fracture due to the shock wave resulting from cracking. This is because the shock wave is absorbed by the viscosity. The viscous term works as a damper that absorbs the shock wave of cracking. The viscous term is necessary; However it becomes negligible compared to the elastic term and the desiccation term. If the paste does not stick on the bottom, the paste can deform freely. In this case, the stress owing to the desiccation term is relaxed by the elastic deformation. As a result, there is no stress concentration. In our model, there are spatial regions where the paste can not deform freely because the paste sticks on the bottom. In consequence, stress concentration appears. The three stresses play important roles in reproducing the desiccation crack pattern.

## 2.3 Approximation to a thin layer

We can simulate the behavior of desiccating paste by using Eqs. (2.1)∼(2.13). The three dimensional equations are solved by an appropriate solver of continuum with the discretization of spatial coodinates. However it is hard to compute the three dimensional equations, because the huge number of discretized points is required in a three dimensional problem. Therefore it is necessary to reduce the the number of discretized points in order to solve the equations. The simplest way to achieve the reduction is to reduce the spatial dimension. Because we are fortunately focusing on a thin layer of paste, we can reduce the spatial dimension to two from three. We achieve the reduction as in the following way. We eliminate the depth dependence of the quantities from the equation of motion. The approximation is introduced by Otsuki [39]. If the thickness of the paste $H$ is small enough, then the motion along the $z$ direction can be negligible, that is, $u_z \sim 0$ and $v_z \sim 0$. In addition, it is assumed that the depth derivative is approximated as the difference between the top ($z = H$) and the bottom ($z = 0$) of the paste. Under the approximation, the strain along $z$ direction at $(x, y, 0)$, $\epsilon_{iz}(x, y, 0)$ $(i = x, y)$ and $\epsilon_{zz}(x, y, 0)$, are given by

$$\begin{aligned}
\epsilon_{iz}(x, y, 0) &= \frac{1}{2}\left(\frac{\partial u_i}{\partial z}(x, y, 0) + \frac{\partial u_z}{\partial x_i}(x, y, 0)\right) \\
&= \frac{1}{2}\frac{\partial u_i}{\partial z}(x, y, 0) \\
&\sim \frac{1}{2}\frac{u_i(x, y, H) - u_i(x, y, 0)}{H} \\
&= \frac{1}{2}\frac{u_i(x, y, H)}{H},
\end{aligned} \tag{2.14}$$

and

$$\begin{aligned}
\epsilon_{zz}(x, y, 0) &= \frac{\partial u_z}{\partial z}(x, y, 0) \\
&\sim \frac{u_z(x, y, H) - u_z(x, y, 0)}{H} \\
&\sim 0.
\end{aligned} \tag{2.15}$$

In these expressions, we use the boundary condition Eq. (2.5). $\dot{\epsilon}_{iz}(x, y, 0)$ and $\dot{\epsilon}_{zz}(x, y, 0)$ are expressed similarly:

$$\dot{\epsilon}_{iz}(x, y, 0) \sim \frac{1}{2}\frac{v_i(x, y, H)}{H}, \tag{2.16}$$

$$\dot{\epsilon}_{zz}(x, y, 0) \sim 0. \tag{2.17}$$

On the surface of the paste, the equation of motion Eq. (2.1) is expressed as

$$\rho \frac{dv_i}{dt} = \frac{\partial \sigma_{ij}}{\partial x_j} + \frac{\partial \sigma_{iz}}{\partial z}, \tag{2.18}$$

for $i, j = x, y$ at the coordinate $(x, y, H)$. For the motion along $i$-th direction, the second term of right-hand side represents the resistance force due to sticking on the bottom. It is given by

$$\begin{aligned} \frac{\partial \sigma_{iz}(x, y, H)}{\partial z} &\sim \frac{\sigma_{iz}(x, y, H) - \sigma_{iz}(x, y, 0)}{H} \\ &= -\frac{\sigma_{iz}(x, y, 0)}{H} \\ &\sim -\frac{\mu}{H^2} u_i(x, y, H), \end{aligned} \tag{2.19}$$

where we ignore the viscous term in $\sigma_{iz}$ because it is very small compared with the elastic term when the system shrinks slowly. Therefore Eq. (2.18) is reduced to the closed form at the coordinate $(x, y, H)$, which is given by

$$\rho \frac{dv_i}{dt} = \frac{\partial \sigma_{ij}}{\partial x_j} - \frac{\mu}{H^2} u_i. \tag{2.20}$$

Here we find that the second term of the right-hand side in Eq. (2.20) corresponds to the resistant force owing to the adhesion to the bottom.

### 2.3.1 Quasi two dimensional continuum model

We obtain the equations of the quasi two dimensional model as follows:

$$\rho \frac{d\boldsymbol{v}}{dt} = \nabla \cdot \boldsymbol{\sigma} - \frac{\mu}{H^2} \boldsymbol{u}, \tag{2.21}$$

$$\frac{d\rho}{dt} = \rho \nabla \cdot \boldsymbol{v}, \tag{2.22}$$

$$\frac{d\boldsymbol{u}}{dt} = \boldsymbol{v}, \tag{2.23}$$

$$\boldsymbol{\sigma} = \boldsymbol{\sigma}_{\mathrm{el}} + \boldsymbol{\sigma}_{\mathrm{vis}} + \boldsymbol{\sigma}_{\mathrm{dry}}, \tag{2.24}$$

$$\frac{d\boldsymbol{\sigma}_{\mathrm{el}}}{dt} - \boldsymbol{\Omega} \cdot \boldsymbol{\sigma}_{\mathrm{el}} + \boldsymbol{\sigma}_{\mathrm{el}} \cdot \boldsymbol{\Omega} = \lambda \mathrm{Tr}\left(\dot{\boldsymbol{\epsilon}}\right) \boldsymbol{I} + 2\mu \dot{\boldsymbol{\epsilon}}, \tag{2.25}$$

$$\boldsymbol{\sigma}_{\mathrm{vis}} = \eta \dot{\boldsymbol{\epsilon}}, \tag{2.26}$$

$$\boldsymbol{\sigma}_{\mathrm{dry}} = F(t)\boldsymbol{I}, \tag{2.27}$$

$$\dot{\boldsymbol{\epsilon}} = \frac{1}{2}\left(\nabla \otimes \boldsymbol{v} + \nabla \otimes \boldsymbol{v}^T\right), \tag{2.28}$$

and

$$\boldsymbol{\Omega} = \frac{1}{2}\left(\nabla \otimes \boldsymbol{v} - \nabla \otimes \boldsymbol{v}^T\right). \tag{2.29}$$

where $\boldsymbol{u} = (u_x, u_y)$, $\boldsymbol{v} = (v_x, v_y)$, $\boldsymbol{\sigma} = \begin{pmatrix} \sigma_{xx} & \sigma_{xy} \\ \sigma_{yx} & \sigma_{yy} \end{pmatrix}$, $\dot{\boldsymbol{\epsilon}} = \begin{pmatrix} \dot{\epsilon}_{xx} & \dot{\epsilon}_{xy} \\ \dot{\epsilon}_{yx} & \dot{\epsilon}_{yy} \end{pmatrix}$, and $\boldsymbol{\Omega} = \begin{pmatrix} \Omega_{xx} & \Omega_{xy} \\ \Omega_{yx} & \Omega_{yy} \end{pmatrix}$ denote the two dimensional displacement, velocity, stress, strain rate tensor, and spin tensor. $\boldsymbol{I} = \begin{pmatrix} 1 & 0 \\ 0 & 1 \end{pmatrix}$ denotes the two dimensional unit tensor. As the desiccation stress $F(t)$, we assume a linear function given by

$$F(t) = v_\tau t, \tag{2.30}$$

where $v_\tau$ denotes the increasing of the desiccation stress per time. The linear increasing function of the desiccation stress is used in some previous works [39, 65, 70].

## 2.4 Yield condition

When we simulate fracture with the continuum model, we have to impose a yield criterion. There are many yield criteria depending on the kind of material. In this chapter, we use the criterion by using the local averaged stress [80]

$$\bar{\sigma} = \frac{1}{2}\left(\sigma_{xx} + \sigma_{yy}\right), \tag{2.31}$$

which corresponds to the local pressure. The local averaged stress criterion is described as follows: (1) $\bar{\sigma}$ at all positions in the material is calculated. (2) If $\bar{\sigma}$ is greater than the threshold yield stress $\sigma_Y$, then the stress at the position is assumed to be zero. Another stress criterion also gives the same quantitive results. We have confirmed them when we use the maximum principal stress [81]

$$\sigma_m = \frac{1}{2}\left(\sigma_{xx} + \sigma_{yy}\right) + \frac{1}{2}\sqrt{\left(\sigma_{xx} - \sigma_{yy}\right)^2 + 4\sigma_{xy}^2}, \tag{2.32}$$

instead of the local averaged stress as the yield criterion. This is because the local average stress is greater than the deviatoric stress in the parameter set used in this chapter.

## 2.5 Continuum equations in smoothed particle hydrodynamics

Smoothed particle hydrodynamics (SPH) is a method for solving equations of continuum by using a movable mesh point, that is, a "particle" [72, 73]. All particles have physical quantities. Let the upper index represented by the uppercase letter of the physical quantities denote the label of particles. For instance, $\boldsymbol{r}^I$ is the position of the particle $I$. In the SPH formula, a general physical quantity $f^I$ of the particle $I$ is given by

$$f^I = \sum_{J \in \mathcal{S}} f^J W\left(\left|\boldsymbol{r}^I - \boldsymbol{r}^J\right|; h\right) \frac{m^J}{\rho^J}, \tag{2.33}$$

where $m^J$ and $\rho^J$ are the mass and density of particle $J$, respectively. The set of $J$ in the summation, $\mathcal{S}$, is determined from the non-zero region of the function $W(x; h)$. This function is a kernel function with a positive parameter $h$, which is known as the "effective length". $W(x; h)$ is required to be a Dirac delta function under the limit of $h \searrow 0$. The accuracy of the simulation is related to the choice of the kernel function $W(x; h)$. In previous works on SPH simulation [74, 75], this function is given by

$$W(x; h) = \frac{63}{478\pi h^2} W_5\left(\frac{x}{h}\right) \quad , \tag{2.34}$$

where $W_5(x)$ is a quintic spline function,

$$W_5(x) = \begin{cases} q_3(x) - 6q_2(x) + 15q_1(x) & (|x| \leq \frac{1}{3}) \\ q_3(x) - 6q_2(x) & (\frac{1}{3} < |x| \leq \frac{2}{3}) \\ q_3(x) & (\frac{2}{3} < |x| \leq 1) \\ 0 & (1 < |x|), \end{cases}$$

with

$$q_k(x) = (k - 3|x|)^5 \quad (k = 1, 2, 3).$$

In other works, various functions such as a cubic spline function [76, 77], a Gaussian function, and a cubic function [78] are used. In this work, we use a quintic spline function because it is often used in previous works.

In the SPH description, a gradient of the physical quantity $\nabla f^I$ is given by

$$\nabla f^I = \sum_J f^J \nabla W\left(\left|\boldsymbol{r}^I - \boldsymbol{r}^J\right|; h\right) \frac{m^J}{\rho^J}. \tag{2.35}$$

By using Eq. (2.35), the elemental terms of the continuum equations, $\nabla \cdot \boldsymbol{\sigma}$, $\nabla \otimes \boldsymbol{v}$, and $\nabla \cdot \boldsymbol{v}$ are discretized as follows:

$$\left(\frac{\nabla \cdot \boldsymbol{\sigma}}{\rho}\right)^I = \sum_J m^J \nabla W^{IJ} \cdot \left\{\frac{\boldsymbol{\sigma}^I}{(\rho^I)^2} + \frac{\boldsymbol{\sigma}^J}{(\rho^J)^2}\right\}, \tag{2.36}$$

$$(\nabla \otimes \boldsymbol{v})^I = \sum_J \frac{m^J}{\rho^I} \nabla W^{IJ} \otimes \left(\boldsymbol{v}^J - \boldsymbol{v}^I\right), \tag{2.37}$$

$$(\nabla \cdot \boldsymbol{v})^I = \mathrm{Tr}\left((\nabla \otimes \boldsymbol{v})^I\right), \tag{2.38}$$

where $\nabla W^{IJ}$ denotes $\nabla W\left(\left|\boldsymbol{r}^I - \boldsymbol{r}^J\right|; h\right)$.

When we compute the time evolution of Eqs. (2.21), (2.22), (2.23) and (2.25) in the SPH description, we do not calculate the advection term because SPH is based on the Lagrangian description. Instead of calculating the advection term, we must calculate the time evolution of the positions of particles as follows:

$$\frac{d\boldsymbol{r}^I}{dt} = \boldsymbol{v}^I. \tag{2.39}$$

To avoid numerical instability, we use a velocity averaging method. In SPH simulations, interaction between particles has no repulsive component. Therefore, under extreme conditions, there is a case in which particles are close to each other. This condition causes numerical instability. To avoid this, the velocity averaging method was proposed by Monaghan [76, 82]. According to Monaghan 's description, the velocity of particle $I$ is modified as follows:

$$\boldsymbol{v}^I \to \boldsymbol{v}^I + \tilde{\epsilon} \sum_J \frac{m^J}{\rho^{IJ}} \left(\boldsymbol{v}^J - \boldsymbol{v}^I\right) W\left(\left|\boldsymbol{r}^I - \boldsymbol{r}^J\right|; h\right), \tag{2.40}$$

where $\rho^{IJ}$ denotes $\frac{1}{2}\left(\rho^I + \rho^J\right)$ and $\tilde{\epsilon}$ is a tuning parameter. In this study, we choose $\tilde{\epsilon} = 0.5$.

In the subsequent simulation, Eqs. (2.21)-(2.30) are discretized by using Eqs. (2.36)-(2.40), which are taken as the basic equations of the computational model.

In the present model, we use the local average stress criterion in SPH to examine the nucleation of the crack. It is plausible to treat the fractures of the drying paste as brittle fractures. According to the principles of continuum modeling, we should set the stress of a particle to zero when the stress becomes greater than the yield stress, $\sigma_Y$. However, we cannot reproduce a brittle fracture with the above procedure because stress relaxes rapidly. Stress on the surfaces of cracks relaxes as long as both faces of the cracks are within the effective length, $h$. In the SPH description, there are different treatments

| Parameter | Symbol | Value | Dimensionless value |
|---|---|---|---|
| First Lame's constant | $\lambda$ | $1.0 \times 10^9$ Pa | 1.0 |
| Second Lame's constant | $\mu$ | $1.0 \times 10^8$ Pa | 0.1 |
| Yield stress | $\sigma_Y$ | $5.0 \times 10^6$ Pa | $5.0 \times 10^{-3}$ |
| Viscosity | $\eta$ | $1.0 \times 10^5$ Pa·s | 1.0 |
| Thickness of paste | $H$ | 3.16 cm | 0.316 |
| Drying speed | $v_\tau$ | $2.2 \times 10^8$ Pa/s | $2.2 \times 10^{-5}$ |
| Length of a side | $L$ | 100 cm | 10.0 |
| Effective length | $h$ | 2 cm | 0.2 |
| Number of SPH particles | N | | $4.0 \times 10^4$ |
| Intial density | $\rho_0$ | 1.0 g/cm$^3$ | 1.0 |
| Intial stress | $\boldsymbol{\sigma}_0$ | | -0.01∼0.01×$\sigma_Y$ |

Table 2.1: List of parameters and initial quantities used in the simulation.

for brittle fractures [80, 83]. In this study, we meet the local average stress criterion by removing particles from the simulated paste described by SPH; This procedure has the same effect of resetting the stress of particle to zero. In this case, the distance between two created surfaces becomes large, preventing stress relaxation.

## 2.6 Numerical setting for computation

In the actual simulation, we prepare a square paste with dimensions $L \times L$. We impose a periodic boundary condition on the paste. Values of the parameters and initial physical quantities are summarized in TABLE 2.1. It is difficult to fit these parameters to the experimental parameters exactly because it is difficult to measure the actual material constants. We performed simulations by using other values of $H$, $\sigma_Y$, and elastic constants. As far as we have searched, the statistical properties do not change qualitatively. The accuracy of our results depends on the parameter $\epsilon$, the functional form of $W$, and the number of particles. We choose appropriate parameters for measuring the statistical properties. For instance, the parameter $h$ is required to be smaller than the minimum-length scale imposed by the material constants. We choose a value of $h$ that satisfies the condition.

These values are non-dimensionalized by $\rho_0$, $\lambda$ and $\eta$. The units of time and space are given by $\eta/\lambda$ and $\eta/\sqrt{\rho_0\lambda}$, respectively. Initial positions of particles are located randomly to avoid anisotropic patterns. The initial displacement and velocity are taken to be zero. The initial density, $\rho_0$, which is a unit of dimension, is the constant shown in TABLE 2.1. The initial stress, $\boldsymbol{\sigma}_0$, is

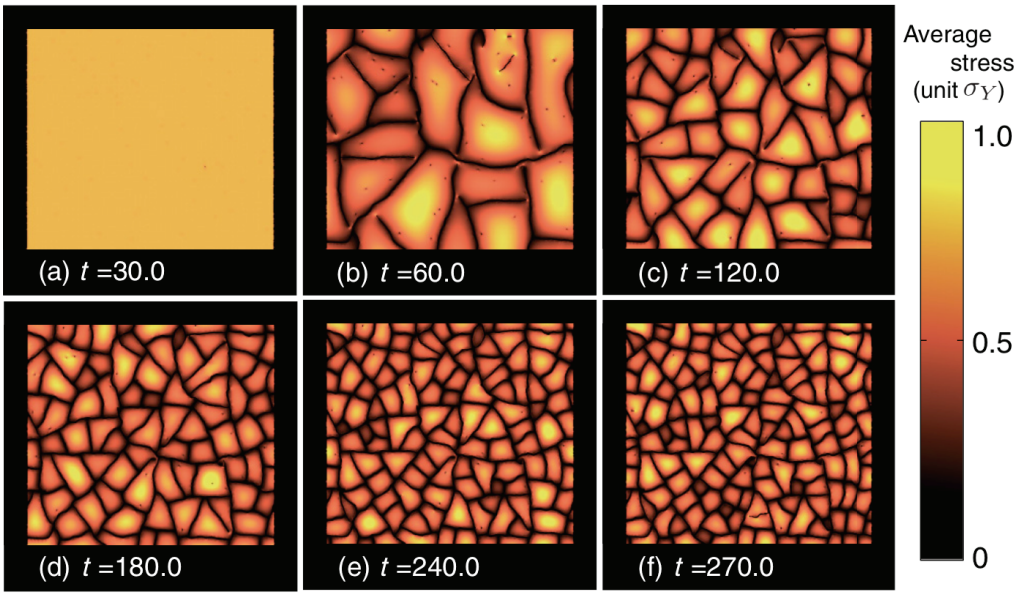


Figure 2.2: Time evolution of the crack patterns reproduced by the SPH simulation. This figure is taken from Ref. [79].

randomly chosen from the uniform distribution shown in TABLE 2.1. The mass, $m$, of the particle is calculated from the initial density, $\rho_0$, and the initial position, $\boldsymbol{r}$, by using the consistent condition:

$$\rho_0 = \sum_J m^J W\left(\left|\boldsymbol{r}^I - \boldsymbol{r}^J\right|; h\right). \tag{2.41}$$

Equation (2.41) is a linear simultaneous equation, which is a large sparse matrix problem. In order to solve Eq. (2.41), we use the conjugate gradient method [84]. We calculate the time evolution of quantities by using the fourth-order RungeKutta (RK4) method [85] and the fourth-order predictorcorrector (PC4) method [86]. RK4 is used for a few initial time steps and in several time steps after the removal of particles, and PC4 is used for the main time steps. This is because the physical quantities become discontinuous particles are removed, and the calculation may become unstable if we use only PC4.

## 2.7 Result

### 2.7.1 Crack pattern

Figure 2.2 shows snapshots of stress in the paste. The color shows the magnitude of the local average stress normalized according to the yield stress. The

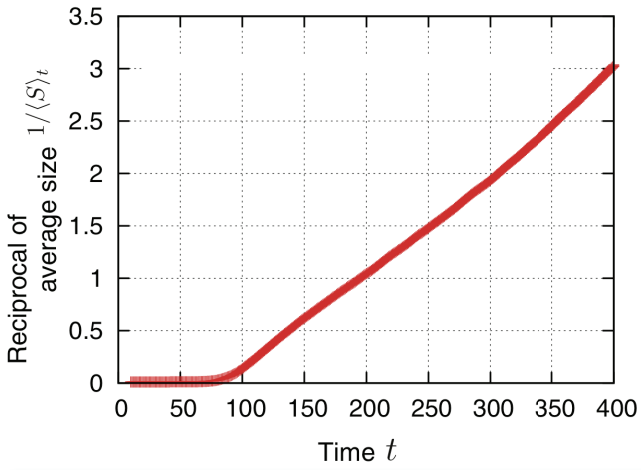


Figure 2.3: Time evolution of the average areal size. This figure is taken from Ref. [79].

black region represents cracks. Nucleation of some cracks before the cracks run could be observed. There are some cases in which the cracks do not grow. The reason for such phenomena is unclear. In the simulation, the velocity of the crack tip decreases during growth; It is highest at the beginning of growth and decays upon approaching another crack. This behavior is similar to the real dynamics of cracks in drying paste.

In this figure, we can see that the local average stress is almost zero along the edge of each fragment, and it reaches a maximum near the center of the fragments. In general, stress along the edge is relieved more easily than stress in the bulk because the material along the edges can migrate freely. This effect tends to occur in cases in which the fragment shape is nearly isotropic. In cases with complex fragment shapes, stress concentration can occur. However, our results indicate that such cases are rare.

### 2.7.2 Average size

In order to investigate the time evolution of the average area of fragments, we simulate samples with various initial conditions of stress. To calculate the area of a fragment, we binarize the image of the snapshot of the stress as follows: We discretize the image of the snapshot with a square mesh. On each mesh point, $\boldsymbol{x}$, a binary quantity $\phi(\boldsymbol{x})$ is calculated using

$$\phi(\boldsymbol{x}) = \begin{cases} 1 & \text{for } \phi_0 \leq \sum_J \dfrac{m^J}{\rho^J} W\left(\boldsymbol{x} - \boldsymbol{r}^J; h\right) \\ 0 & \text{otherwise,} \end{cases}$$

where $\phi_0$ is a threshold value. When a sufficient number of particles surround the mesh point $\boldsymbol{x}$, $\phi(\boldsymbol{x})$ equals 1. We then identify that the position $\boldsymbol{x}$ is inside a fragment. Conversely, if few particles surround the point $\boldsymbol{x}$, then $\phi(\boldsymbol{x})$ is 0. This means that the point is outside of the fragment, and is included in the region of the cracks. In this manner, we identify whether the position is inside of the fragment. After binarization, we apply cluster analysis and calculate the area of each fragment by summing up the value of $\phi$. Here, we assume that the threshold value is equal to 0.8 ($\phi_0 = 0.8$) and that the length of the square mesh may be expressed as $\Delta x = 0.01h$.

Let $\langle S \rangle_t$ denote the average area of fragments at time $t$. Figure 2.3 shows the time evolution of $\langle S \rangle_t$. As we observe in this figure, the reciprocal of $\langle S \rangle_t$ evolves proportionally with time except during initial relaxation. In other words, $\langle S \rangle_t$ is asymptotically inversely proportional to time. In the actual experiments, the decay of the average area stops at times because the desiccation stress becomes saturated. In the present model, however, the decay of the average cannot stop because of the linear dependence of the desiccation stress $\boldsymbol{\sigma}_{\mathrm{dry}}$ on time; This result is an artifact of the model.

The power-law decay of the average area may be explained by dimensional analysis. We consider the quasi-static situation of the dynamics. In this case, dependence of the term on the velocity may be negligible. The equation of motion, Eq. (2.21), then becomes:

$$\frac{\partial \sigma_{ij}}{\partial x_j} = \frac{\mu}{H^2} u_i. \tag{2.42}$$

Furthermore, the constitutive equation, Eq. (2.24), in which the viscous term is ignored in the quasi-static situation with a general form of desiccation stress, $F(t)$, is given by

$$\sigma_{ij} = \left\{ \lambda \frac{\partial u_k}{\partial x_k} + F(t) \right\} I_{ij} + \mu \left( \frac{\partial u_i}{\partial x_j} + \frac{\partial u_j}{\partial x_i} \right). \tag{2.43}$$

Let $U(t)$, $\Xi(t)$ and $L(t)$ denote a characteristic displacement, stress, and length of the fragment, respectively. In addition, the differential operator $\partial/\partial x$ is replaced by $1/L(t)$. With these characteristic quantities, Eqs. (2.42) and (2.43) are rewritten as follows:

$$-\frac{\Xi(t)}{L(t)} = \frac{\mu}{H^2} U(t), \tag{2.44}$$

$$\Xi(t) = (\lambda + 2\mu) \frac{U(t)}{L(t)} + F(t), \tag{2.45}$$

where the negative sign on the left side of the first equation is caused by stress, which is measured at the center of the fragment. The displacement is measured

at the edge of the fragment. Eliminating $U(t)$ from these equations, we obtain the relationship between $\Xi(t)$, $L(t)$ and $F(t)$:

$$L^2(t) = \frac{\lambda_D^2}{F(t)/\Xi(t) - 1}, \tag{2.46}$$

where $\lambda_D = H\sqrt{(\lambda + 2\mu)/\mu} = H\sqrt{2(1-\nu)/(1-2\nu)}$ and $\nu$ denotes a Poisson's ratio. The value of $\Xi(t)$ is limited by the yield stress. Thus, $\Xi(t)$ may be replaced by the yield stress in the time evolution of $L^2(t)$. Therefore $\langle S \rangle_t$ varies with $1/F(t)$. In the case of linear increment desiccation stress, $\langle S \rangle_t$ is asymptotically proportional to $1/t$.

We now discuss the effect of $\lambda_D$. $\lambda_D$ describes how the influence of the boundary condition of stress affects the inner stress. The details are discussed in Chapter 3. An incompressible limit ($\nu \to 1/2$) gives a diverging $\lambda_D$. Therefore, a value of $\lambda_D$ that is greater than the characteristic length of the fragment shape causes a strong stress concentration at the center of a fragment. As a result, the cracks tend to nucleate from the center of fragment. The Poisson's ratio that we use describes nearly incompressible materials. We may consider that the incompressibility is one of the causes of crack nucleation from the center of a fragment.

Equation. (2.46) corresponds to the time evolution of $\langle S \rangle_t$; However, the slope of $L(t)^2$ is nearly twice as small as that of $\langle S \rangle_t$ (Fig. 2.3). We believe that this is because Eq. (2.46) only gives the relationship between the variables of length and time.

### 2.7.3 Size distribution

Next, we investigate the time evolution of area distributions of the fragments. Let $\mathrm{P}(S;t)$ denote the area, $S$, and the distribution at time $t$. Figure 2.4 (a) shows the time evolution of the area distribution. The peak of the distribution moves to a smaller area with time. This shift is trivial. In the present model, this peak approaches zero with time, since drying is not terminated.

We find that the distribution can be scaled according to the individual averages of the area. The result is shown in Fig. 2.4 (b). In other words, by using a dimensionless variable,

$$X = S/\langle S \rangle_t \quad , \tag{2.47}$$

and the original distribution, $\mathrm{P}(S;t)$ may be transformed into a time-independent distribution $\widetilde{\mathrm{P}}(X)$:

$$\langle S \rangle_t \mathrm{P}(S;t) = \widetilde{\mathrm{P}}(X), \tag{2.48}$$

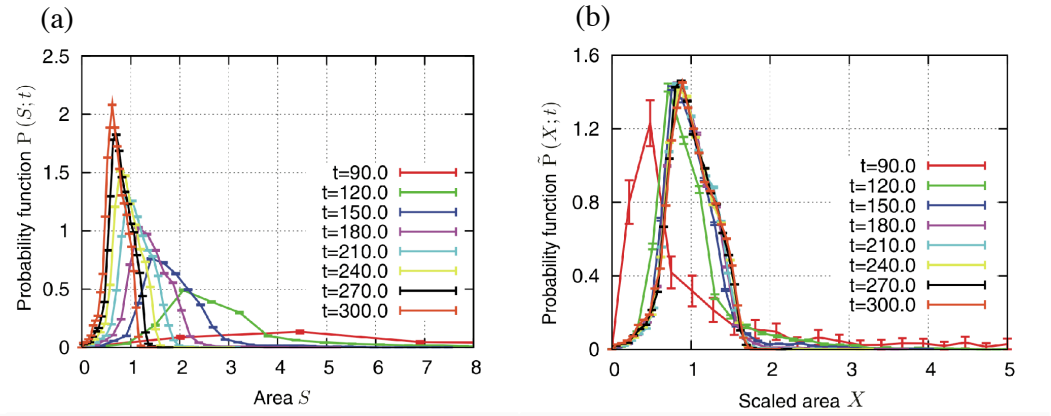


Figure 2.4: Time evolution of the areal size distribution. This figure is taken from Ref. [79].

where the factor $\langle S \rangle_t$ on the left side arises from the normalization of the distribution. This property does not hold in the initial relaxation; However, it is clearly observed in the case before $t = 180.0$ in Fig. 2.4 (b). After the initial stage, the distribution is well scaled.

The duration of the initial relaxation of the time evolution of $\langle S \rangle_t$ corresponds to a distribution that cannot be scaled. Using Eq. (2.46), we estimate the cross-over time between the initial relaxation and the power-law decay. This is determined by the time when $F(t)/\Xi(t)$ becomes greater than 1 in Eq. (2.46); If $F(t)/\Xi(t)$ is greater than 1, then the average area decays in proportion to $\Xi(t)/F(t)$. The upper limit of $\Xi(t)$ is the yield stress, $\sigma_Y$. The lower limit is estimated to be greater than zero because the paste had shrunk and effectively experienced tension. This rough estimate is reached by assuming that $\Xi(t)$ equals $\sigma_Y$. The time scale, $t_0$, of the crossover is found to be $t_0 \sim \sigma_Y / v_\tau \sim 227$. The actual time scale might be smaller than this value because $\Xi(t)$ is a characteristic stress in the fragments, which is smaller than $\sigma_Y$.

## 2.8 Summary

In this chapter, we have modeled a thin drying paste and reproduced crack patterns by SPH. We have found two properties through the power-law decay of the average area with the power function of the desiccation stress, as well as the scaling law for the area distributions. According to our dimensional analysis, we analyzed the relationship between the average area of the fragments and the desiccation stress.

In our model, the number of fragments increases in proportion to time, since the average area behaves inversely with time. This result shows that drying fracture is not a simple dividing process, as in the case of cell division in which the number of cells increases exponentially. To understand this result, it is necessary to consider the dividing process and to consider the dynamics of drying fractures. Most of the typical distributions of the fragment size of the dividing process, such as normal and log-normal distributions, have two characteristic parameters, the average and variance. They can be scaled according to two parameters. The distribution in our model, however, may be scaled according to only one parameter, the average area of the fragments. Therefore, the present distribution is not described by typical distributions. The functional form of the present distribution has not been identified yet. In one study, the mass distribution is scaled according to the average mass in the simulation of fragmentation of hard-core granular gases using various restitution coefficients [87]. The result does not have a direct relation to our results. However, they have properties that are analogous to the present scaled distribution.

We used a linear function for desiccation stress. However, the validity of the functional form is completely unknown. On the other hand, it appears to be a simple and reasonable functional form because the desiccation stress is related to the amount of the inner liquid of the material. When the inner liquid evaporates from the material, the local density decreases, thereby decreasing hydrostatic pressure. The decrease in hydrostatic pressure corresponds to the increase in desiccation stress. In particular, the increase in desiccation stress is expected to be proportional to the decrease in the amount of the inner liquid. Therefore, the desiccation stress is proportional to time if the loss of the inner liquid per time due to the evaporation is constant. Unfortunately, there is no experimental study on the functional form of desiccation stress.

Because of the difficulty of computation, we could not check the type of the functional form of $F(t)$ that can play a dynamical scaling law. However, a simplified model of our SPH model, which is proposed in the next chapter, suggests that the scaling law is obeyed when the desiccation stress is a power function of time.

# Chapter 3

# Stochastic modeling of time dependent desiccation crack pattern

In the previous chapter, we have investigated the statistical properties of the desiccation crack pattern of the continuum model. The average areal size decays in inverse proportion to time. The time series of areal size distribution collapses into a master curve by scaling with the average size. How is the behavior determined? In this chapter, we elucidate the cause. To investigate the statistical properties, we remodel the continuum model into a stochastic model on the basis of the Gibrat process. First, we investigate the dynamics of a single fragment by the analytical and numerical calculations. Next, we introduce this dynamics into the Gibrat process. The stochastic model reproduces the dynamical scaling law of the size distribution, and the power-law of the average size. Finally, we find the condition to realize the dynamical scaling law by the scaling analysis of the master equation of the stochastic model.

## 3.1 Lifetime of fragment

Let us consider the dynamical behavior of a single specimen. The properties of the specimen may depend on time. In this section, we investigate the dynamics of a single specimen in order to obtain the information which is necessary to reproduce the statistical properties of the desiccation crack pattern. In the fragmentation process, one of important things is the interval between events of breaking. The interval reflects on the time-dependent statistical properties. We call the time interval "lifetime" of the fragment and investigate it first.

In this section, the lifetime of fragment is derived by the theoretical and

numerical calculations. To simplify the calculation, we assume the dynamics of the layer of paste is over-damped because of the strong viscosity. In this case, the inner velocity is expect to be very slow. Thus we ignore the effect of deformation velocity. As a consequence, the over-damped equation of motion and the constitutive equation are given by

$$\nabla \cdot \boldsymbol{\sigma} = \frac{\mu}{H^2}\boldsymbol{u}, \tag{3.1}$$

and

$$\boldsymbol{\sigma} = \left[\lambda \nabla \cdot \boldsymbol{u} + F(t)\right] \boldsymbol{I} + \mu \left(\nabla \otimes \boldsymbol{u} + \nabla \otimes \boldsymbol{u}^T\right), \tag{3.2}$$

from Eqs. (2.20) and (2.6). For the simplicity of the following analysis, we assume that the desiccation stress $F(t)$ is described by

$$F(t) = F_0 f\left(\frac{t}{\tau}\right), \tag{3.3}$$

where $F_0$ and $\tau$ denote the characteristic stress and the time scale, respectively. $f$ is a dimensionless arbitrary increasing function.

We assume that the fragmentation of paste starts to break when the inner stress exceeds a threshold stress $\sigma_Y$ determined by a yield criterion. The lifetime is defined by the interval between the time when the fragment is created and the time when it starts to break. In this section, we assume that the shape of fragment is convex polygonal for simplifying the analysis. We calculate the lifetime in cases that the shape of fragment is characterized by a single length or a couple of lengths. In the case that the shape of fragment is characterized by a single length, such as disk-shaped and square fragment, the area dependency of lifetime can be investigated analytically. In the case that the shape of fragment is characterized by a couple of lengths, such as rectangular fragment, the aspect ratio dependency of lifetime can also be investigated. If the fragment shape is a complicated polygon, there may be other quantities characterizing the shape of fragments in much detail; However, we do not take them into account. The purpose of this section is to obtain the lifetime as the function of the area or the aspect ratio.

First we investigate the lifetime by a dimensional analysis in the case that the shape of fragment can be characterized by a single length scale. In addition, its validity is confirmed by the exact solution of the lifetime in the case that the shape of fragment is described by a disk. Furthermore, the results are compared with the lifetime calculated numerically in the case that the shape of fragment is square. The numerical calculation is carried out by the two dimensional finite element method [88]. Finally the lifetime in the case that the shape of fragment is described by a rectangular is calculated numerically and compered with the previous results.

### 3.1.1 Dimensional analysis

We derive the lifetime by a dimensional analysis. We take a paste with thickness $H$. The surface area is characterized with $L^2$, where $L$ is a linear dimension. We assume the characteristic scale of changing the displacement and stress can also be expressed with the same scale $L$. Namely, the spatial differential operator is replaced by $1/L$. Let $\mathcal{U}$ and $\mathcal{S}$ denote the characteristic scale of displacement and stress, respectively. Then Eqs. (3.1) and (3.2) can be expressed as follows:

$$-\frac{\mathcal{S}}{L} = \frac{\mu}{H^2}\mathcal{U}, \tag{3.4}$$

and

$$\mathcal{S} = (\lambda + 2\mu)\frac{\mathcal{U}}{L} + F(t). \tag{3.5}$$

The negative sign on the left-hand side of the first equation results from that the spatial differential of stress is evaluated by the difference between the stress at the edge and at the center of fragment (see Fig. 3.1). Eliminating $\mathcal{U}$ from Eqs. (3.4) and (3.5), $\mathcal{S}$ is obtained as

$$\mathcal{S} = \frac{F(t)}{1 + (\lambda_D/L)^2}, \tag{3.6}$$

where $\lambda_D = H\sqrt{(\lambda + 2\mu)/\mu} = H\sqrt{2\,(1-\nu)\,/\,(1-2\nu)}$ is a length scale of the stress, which is discussed later. $\nu$ denotes the Poission's ratio. The lifetime is defined as the elapsed time between $t = 0$ and the time when $\mathcal{S}$ exceeds $\sigma_Y$. As a result, the lifetime $T_b$ satisfies

$$\frac{F(T_b)}{\sigma_Y} = 1 + \left(\frac{\lambda_D}{L}\right)^2. \tag{3.7}$$

When $L \gg \lambda_D$, the second term of the right-hand side becomes smaller than 1. Inversely, when $L \ll \lambda_D$, the second term of the right-hand side becomes larger than 1 and the right-hand side depends on $L$. Therefore, by using $F(t) = F_0 f\,(t/\tau)$, the lifetime satisfies the following asymptotic form as

$$\begin{aligned} T_b &= \tau f^{-1}\left(\frac{\sigma_Y}{F_0}\left[1 + \left(\frac{\lambda_D}{L}\right)^2\right]\right) \\ &= \begin{cases} \tau f^{-1}\left(\dfrac{\sigma_Y}{F_0}\right) = \text{const.}, & \text{if} \quad L \gg \lambda_D, \\ \tau f^{-1}\left(\dfrac{\sigma_Y}{F_0}\dfrac{\lambda_D^2}{L^2}\right), & \text{if} \quad L \ll \lambda_D, \end{cases} \end{aligned} \tag{3.8}$$

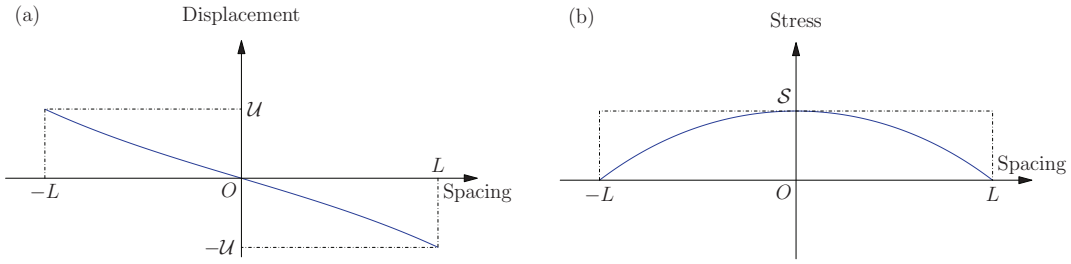


Figure 3.1: Schematic picture of spatial distribution of characteristic displacement and stress. The horizontal axis indicates the spatial coordinate. (a) shows the characteristic displacement field. (b) shows the characteristic stress field.

where $f^{-1}$ denotes the inverse function of $f$.

The validity of the dimensional analysis can be confirmed by an exact calculation of lifetime of a disk-shaped fragment. We consider the disk-shaped fragment with a radius $R$. As the initial condition, we assume that $\boldsymbol{u} = 0$ and $\boldsymbol{\sigma} = 0$ at time $t = 0$. As the boundary condition, the normal stress on the boundary is taken to be zero. The equation of motion and the constitutive equation are reduced to the axisymmetric Navier equation in the polar coordinate, which is given by

$$\frac{\partial^2 u_r}{\partial r^2} + \frac{1}{r}\frac{\partial u_r}{\partial r} - \frac{u_r}{r^2} = \frac{u_r}{\lambda_D^2}, \tag{3.9}$$

with the normal stress

$$\sigma(r,t) = (\lambda + \mu)\left(\frac{\partial u_r}{\partial r} + \frac{u_r}{r}\right) + F(t), \tag{3.10}$$

where $u_r$ is the displacement along the radical direction. Solving Eqs. (3.9) and (3.10), we obtain the normal stress $\sigma$ as

$$\sigma(r,t) = F(t)\left[1 - \frac{I_0\left(r/\lambda_D\right)}{I_0\left(R/\lambda_D\right)}\right], \tag{3.11}$$

where $I_0(z)$ is the modified Bessel function of the first kind.

Then we obtain the lifetime in the disk-shaped fragment, which is given by

$$T_b = \tau f^{-1}\left(\frac{\sigma_Y}{F_0}\left[\frac{1}{1 - 1/I_0\left(R/\lambda_D\right)}\right]\right). \tag{3.12}$$

Equation (3.12) behaves asymptotically as

$$T_b = \begin{cases} \tau f^{-1}\left(\dfrac{\sigma_Y}{F_0}\right) = \text{const.}, & \text{if} \quad R \gg \lambda_D, \\ \tau f^{-1}\left(\dfrac{4\sigma_Y}{F_0}\dfrac{\lambda_D^2}{R^2}\right), & \text{if} \quad R \ll \lambda_D, \end{cases} \tag{3.13}$$

where we use the asymptotic behavior of $I_0(z)$, that is, $I_0(z) \to \infty$ as $z \to \infty$ and $I_0(z) \sim 1 + 4/z^2$ as $z \sim 0$. This result is consistent with the dimensional analysis.

**Physical meaning of $\lambda_D$**

Let us discuss the physical meaning of the length scale $\lambda_D$. We consider a one dimensional system of Eqs. (3.1) and (3.2) in order to understand the meaning of $\lambda_D$,

$$\frac{\partial \sigma}{\partial x} = \frac{\mu}{H^2} u, \tag{3.14}$$

and

$$\sigma = (\lambda + 2\mu) \frac{\partial u}{\partial x} + F(t), \tag{3.15}$$

where $\sigma(x,t)$ and $u(x,t)$ are the one dimensional stress and displacement. The boundary condition is $\sigma = 0$ at $x = \pm L$. From Eqs. (3.14) and (3.15), $\sigma$ is obtained as

$$\sigma(x,t) = F(t) \left[ 1 - \frac{\cosh(x/\lambda_D)}{\cosh(L/\lambda_D)} \right]. \tag{3.16}$$

The behavior of $\sigma(x,t)$ is shown in Fig. 3.2. The horizontal axis indicates the spatial coordinate and the vertical axis indicates the stress. The length of double-headed arrow shows the scale of $\lambda_D$. Figure 3.2 (a) shows the case of $L \ll \lambda_D$ and Fig. 3.2 (b) shows the case of $L \gg \lambda_D$. The stress has a maximum at the center of fragment and the stress at the boundary is restricted to be zero. In the case of $L \gg \lambda_D$, the stress at the center of fragment is not affected by the effect of boundary. As a result, the stress at the center of fragment grows following the growth of $F(t)$. In the case of $L \ll \lambda_D$, the stress of the center of fragment is affected by the effect of boundary and it is stunted the growth. As a consequence, the growth of the stress at the center of fragment in the case of $L \ll \lambda_D$ becomes slower than one in the case of $L \gg \lambda_D$. Thus the scale $\lambda_D$ represents a penetration depth of the boundary stress.

### 3.1.2 Numerical setting for computation

In order to check the result of the lifetime in other shapes, we calculate it numerically. The stress $\boldsymbol{\sigma}(\boldsymbol{x},t)$ and the displacement $\boldsymbol{u}(\boldsymbol{x},t)$ are normalized by the thickness $H$ and the Young's modulus $E = \mu(3\lambda - 2\mu)/(\lambda + \mu)$ and given by

$$\boldsymbol{\sigma}(\boldsymbol{x},t) = E\hat{\boldsymbol{\sigma}}(\boldsymbol{x},t), \tag{3.17}$$

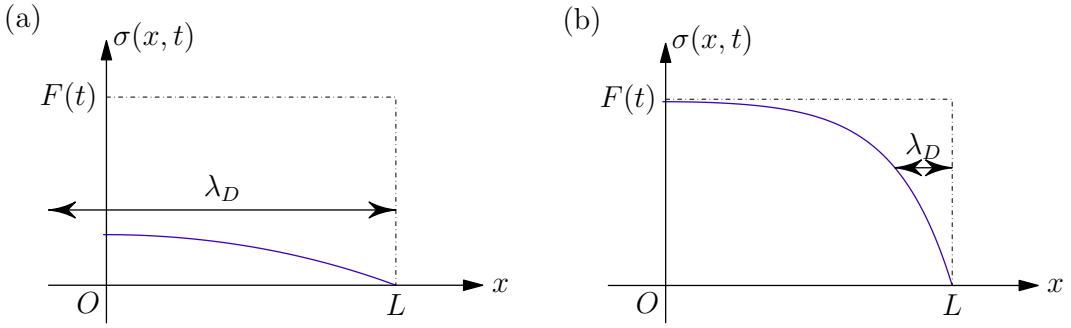


Figure 3.2: The stress distribution in the one dimensional system. The horizontal axis indicates the spatial coordinate. The vertical axis indicates the stress. The length of the double-headed arrow corresponds the length of $\lambda_D$. (a) shows the case of $L \ll \lambda_D$. (b) shows the case of $L \gg \lambda_D$.

and

$$\boldsymbol{u}\left(\boldsymbol{x},t\right) = H\hat{\boldsymbol{u}}\left(\boldsymbol{x},t\right), \tag{3.18}$$

where $\hat{\boldsymbol{\sigma}}\left(\boldsymbol{x},t\right)$ and $\hat{\boldsymbol{u}}\left(\boldsymbol{x},t\right)$ are the dimensionless stress and displacement, respectively. The spatial coordinate $\boldsymbol{x}$ is also normalized by $H$. The desiccation stress $F(t)$ is normalized by $E$, $F(t) = E\hat{F}(t)$, where $\hat{F}(t)$ denotes the dimensionless desiccation stress. Furthermore, from the exact calculation, we assume a product form of stress and the displacement, $\hat{\boldsymbol{\sigma}}(\boldsymbol{x},t) = \hat{F}(t)\tilde{\boldsymbol{\sigma}}(\boldsymbol{x})$ and $\hat{\boldsymbol{u}}(\boldsymbol{x},t) = \hat{F}(t)\tilde{\boldsymbol{u}}(\boldsymbol{x})$. We obtain the simplified forms of Eqs. (3.1) and (3.2) as

$$\nabla\cdot\tilde{\boldsymbol{\sigma}} = \frac{1}{2(1+\nu)}\tilde{\boldsymbol{u}}, \tag{3.19}$$

and

$$\tilde{\boldsymbol{\sigma}} = \left[\frac{\nu}{(1+\nu)(1-2\nu)}\nabla\cdot\tilde{\boldsymbol{u}}+1\right]\boldsymbol{I} + \frac{1}{2(1+\nu)}\left(\nabla\otimes\tilde{\boldsymbol{u}}+\nabla\otimes\tilde{\boldsymbol{u}}^T\right), \tag{3.20}$$

where we use the relations of the elastic constants, $\lambda = E\nu/(1+\nu)/(1-2\nu)$ and $\mu = E/(1+\nu)/2$. Let $\sigma_m(t)$ denote the spatially maximal value of the maximum principal stress of fragment. $T_b$ is calculated by

$$\begin{aligned}
&\sigma_m(T_b) = F(T_b)\tilde{\sigma}_m = \sigma_Y \\
&\Leftrightarrow \frac{F(T_b)}{\sigma_Y} = \frac{F_0}{\sigma_Y} f\left(\frac{T_b}{\tau}\right) = \frac{1}{\tilde{\sigma}_m} \\
&\Leftrightarrow T_b = \tau f^{-1}\left(\frac{\sigma_Y}{F_0}\frac{1}{\tilde{\sigma_m}}\right),
\end{aligned} \tag{3.21}$$

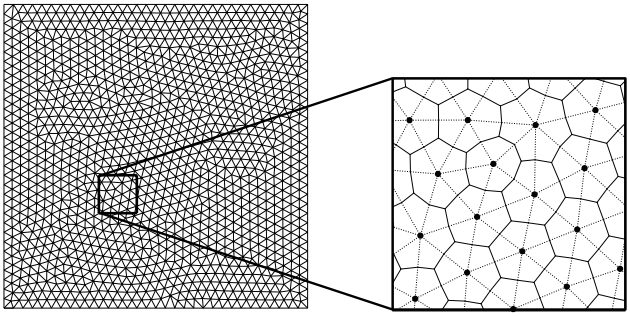

Figure 3.3: The triangular mesh and the cell decomposition. The triangular mesh is obtained by the Delaunay triangulation [90,91]. The vertices of cell are determined by the middle points of side of triangles and the centroids of triangles.

where $\tilde{\sigma}_m$ denotes the dimensionless quantity of $\sigma_m$ which is calculated by Eqs. (3.19) and (3.20). Equations (3.19) and (3.20) are described by the time independent balanced equations. Thus it is easy to analyze them, because there is only one parameter, the Poisson's ratio $\nu$. Changing the Poisson's ratio $\nu$, we observe the $\nu$ dependency of the lifetime. The spatial differential is discretized by a finite volume method [88] with a random triangular lattice, and the balanced equation is calculated by a gradient conjugate method [84]. The calculation points of finite volume method are positioned by a Bossen and Heckbert algorithm [89].

### Finite volume method

We investigate $\tilde{\sigma}_m$ with solving Eqs. (3.19) and (3.20) by a two dimensional finite volume method. We consider a material discretized by a triangular mesh. By connecting the centroid and the middle point of the edge of the triangle, we obtain the group of cells (see Fig. 3.3). Each cell includes just one vertex of the triangle. The cell is called "finite volume". The material is composed of the group of cells. The displacement field in a cell is assumed to be constant. Let us derive the equation of the displacement of a cell from Eqs. (3.19) and (3.20). Let $V_I$ and $\tilde{\boldsymbol{u}}_I$ denote the area and displacement of the cell $I$. Integrating Eq. (3.19) in the cell $I$, we obtain the integral equation given by

$$\int_{S^I} dS\boldsymbol{n}\cdot\tilde{\boldsymbol{\sigma}} = \frac{1}{2(1+\nu)}V_I\tilde{\boldsymbol{u}}_I, \tag{3.22}$$

where $\int_{S^I} dS$ denotes the surface integral around the cell $I$. $\boldsymbol{n}$ denotes the normal vector at the surface toward the outside of the cell. The left-hand side

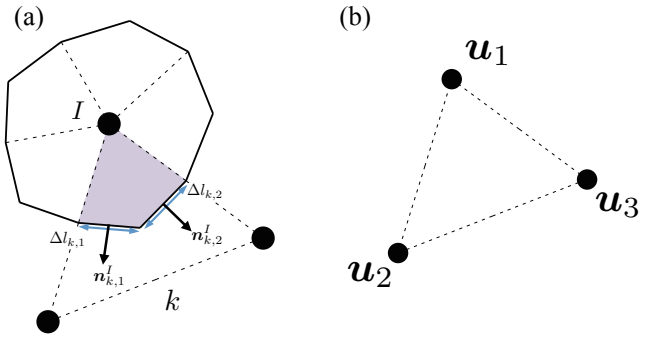


Figure 3.4: The configuration of finite volume method. (a) shows the geometric relationship between a cell and a triangle. They own the common region shown the colored region. (b) shows the positions of three nodes which compose a triangle. The inner stress of the triangle is calculated by the displacement of the three nodes, $\boldsymbol{u}_1$, $\boldsymbol{u}_2$, and $\boldsymbol{u}_3$.

is evaluated by the inner stresses of triangles surrounding cell $I$. Let consider the relationship between the cell $I$ and a triangle $k$ which surrounding the cell $I$. As shown in Fig. 3.4 (a), the two segments of surface of $I$ are included in the triangle $k$. Let $\Delta l_{k,1}$ and $\Delta l_{k,2}$ denote the lengths of the two segments of surface. And $\boldsymbol{n}_{k,1}$ and $\boldsymbol{n}_{k,2}$ denote the normal vectors of the segments toward the outside of the cell. Using this relationship we can evaluate Eq. (3.22) as

$$\sum_{k\in\mathcal{K}}\sum_{i=1,2}\Delta l_{k,i}\boldsymbol{n}^I_{k,i}\cdot\tilde{\boldsymbol{\sigma}}^k=\frac{1}{2(1+\nu)}V_I\tilde{\boldsymbol{u}}^I, \tag{3.23}$$

where $\mathcal{K}$ denotes the group of index of triangles surrounding the cell $I$. $\tilde{\boldsymbol{\sigma}}^k$ is the stress in the triangle $k$. The boundary condition is satisfied by vanishing $\boldsymbol{n}^I_{k,i}\cdot\tilde{\boldsymbol{\sigma}}^k$ when the segment belongs to the surface of the material. The stress of triangle $k$, $\tilde{\boldsymbol{\sigma}}^k$, is evaluated by the displacement of three cells which compose the triangle. As shown in Fig. 3.4 (b), we denote the displacement of three cells, $\boldsymbol{u}_1$, $\boldsymbol{u}_2$, and $\boldsymbol{u}_3$, and we denote the positions of three cells, which are the vertices of the corresponding triangle, $\boldsymbol{x}_1=(x_1,y_1)$, $\boldsymbol{x}_2=(x_2,y_2)$, and $\boldsymbol{x}_3=(x_3,y_3)$, respectively. Using given $\boldsymbol{u}_1$, $\boldsymbol{u}_2$, and $\boldsymbol{u}_3$, the displacement in the triangle $k$, $\boldsymbol{u}^k(x,y)$, is interpolated as

$$\boldsymbol{u}^k(x,y)=N_1(x,y)\boldsymbol{u}_1+N_2(x,y)\boldsymbol{u}_2+N_3(x,y)\boldsymbol{u}_3, \tag{3.24}$$

with the interpolating function

$$
\begin{aligned}
N_1(x,y) &= \frac{1}{2D}\left[(y_2-y_3)x+(x_3-x_2)y+x_2y_3-x_3y_2\right], \\
N_2(x,y) &= \frac{1}{2D}\left[(y_3-y_1)x+(x_1-x_3)y+x_3y_1-x_1y_3\right], \\
N_3(x,y) &= \frac{1}{2D}\left[(y_1-y_2)x+(x_2-x_1)y+x_1y_2-x_2y_1\right],
\end{aligned}
\tag{3.25}
$$

where $D$ is the area of triangle $k$. This method of interpolation is same as the finite element method using the first order triangular finite element [92, 93]. The inner stress of triangle $k$, $\tilde{\boldsymbol{\sigma}}^k$, is calculated by using $\boldsymbol{u}^k$ and given by

$$
\tilde{\boldsymbol{\sigma}}^k = \left[\frac{\nu}{(1+\nu)(1-2\nu)}\nabla\cdot\boldsymbol{u}^k+1\right]\boldsymbol{I}+\frac{1}{2(1+\nu)}\left(\nabla\otimes\boldsymbol{u}^k+(\nabla\otimes\boldsymbol{u}^k)^T\right) \tag{3.26}
$$

Substituting Eq. (3.26) into Eq. (3.23), the linear equations of displacement of cells are obtained. The linear equations are solved by means of a conjugate gradient method [84]. Substituting the solution of the displacement into Eq. (3.23), the stress field is obtained. Then we can evaluate the maximum principal stress field. $\tilde{\sigma}_m$ is searched from the maximum principal stress field.

### 3.1.3 Numerical result

Numerical results are shown in this section. First we confirm the validity of the numerical results by comparing with the analytical solution of the lifetime of the disk-shaped fragment. Next, we carried out the calculation of the lifetime of square fragment and rectangular fragment.

#### Disk-shaped fragment

In order to confirm the numerical result, we compare the lifetime of the disk-shaped fragment calculated numerically and the analytic result of Eq. (3.12). We show the numerical result and that of Eq. (3.12) in Fig. 3.5. The horizontal axis indicates $R^2/\lambda_D^2$. The vertical axis indicates $F(T_b)/\sigma_Y$. The points correspond to the lifetime with $R = 10$ and 20. The different shape of point indicates the difference of $R$. The dotted line is the analytical solution given by Eq. (3.12). The behaviors of lifetime coincide completely. Thus the numerical result is valid.

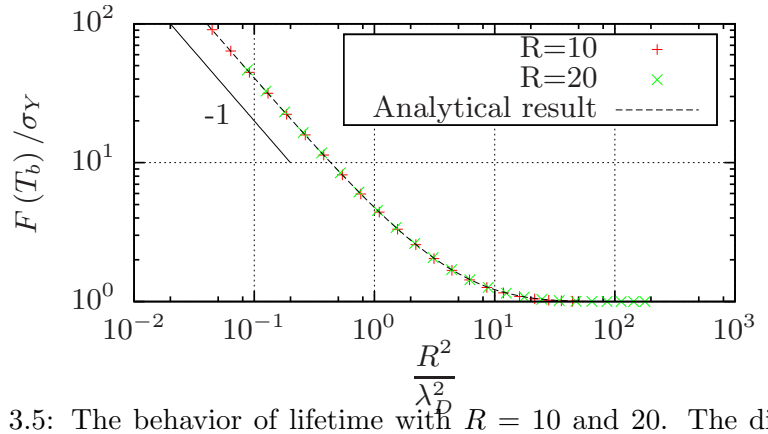


Figure 3.5: The behavior of lifetime with $R = 10$ and 20. The difference of point shape indicates the difference of $R$. The dotted line indicates the analytical solution given by Eq. (3.12). The solid line indicates a power function with the exponent $-1$. The horizontal axis indicates $R^2/\lambda_D^2$. The vertical axis indicates $F(T_b)/\sigma_Y$.

### Square fragment

We show the lifetime of the square fragment with the dimension $L \times L = 16 \times 16$, $32 \times 32$, and $64 \times 64$ in Fig. 3.6. The horizontal axis indicates $L^2/\lambda_D^2$. The vertical axis indicates $F(T_b)/\sigma_Y$. The difference of color indicates the difference of $L$. The solid line indicates a power function with the exponent $-1$. The behavior of the lifetime is qualitatively same with the behavior of the lifetime of the disk-shaped fragment.

### Rectangular fragment

We show the lifetime of the rectangular fragment with the dimension $L_x \times L_y = 20 \times 20$, $30 \times 20$, $40 \times 20$, and $60 \times 20$ as in Fig. 3.7. The horizontal axis indicates $2L_x^2 L_y^2 / \left(L_x^2 + L_y^2\right) / \lambda_D^2$. The vertical axis indicates $F(T_b)/\sigma_Y$. The factor 2 of the horizontal variable is given in order to compare the result with that of the square fragment. We find that the lifetime seems to collapse into a universal curve. And we find that $F(T_b)/\sigma_Y$ diverges in inverse proportion to the horizontal variable at zero. This result predicts the existence of a universal function in the lifetime, which is given by

$$\frac{F(T_b)}{\sigma_Y} = \mathcal{F}\left(\frac{2L_x^2 L_y^2}{L_x^2 + L_y^2}\frac{1}{\lambda_D^2}\right), \tag{3.27}$$

where $\mathcal{F}(z)$ is a scaling function and $\mathcal{F}(z) \sim 1/z$ as $z \to 0$ and $\mathcal{F}(z) \sim 1$ as $z \to \infty$. The general form of lifetime of a rectangular fragment is predicted to

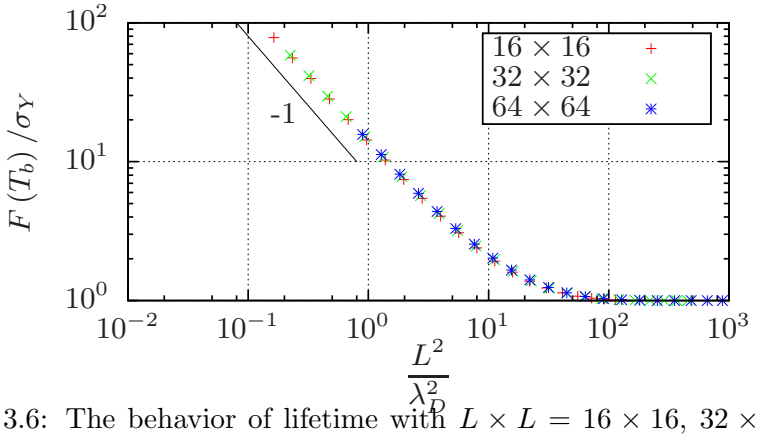


Figure 3.6: The behavior of lifetime with $L \times L = 16 \times 16$, $32 \times 32$, and $64 \times 64$. The difference of color indicates the difference of $L$. The solid line indicates a power function with the exponent $-1$. The horizontal axis indicates $L^2/\lambda_D^2$. The vertical axis indicates $F(T_b)/\sigma_Y$.

be described as

$$T_b = \tau f^{-1}\left(\frac{\sigma_Y}{F_0}\mathcal{F}\left(\frac{2L_x^2L_y^2}{L_x^2+L_y^2}\frac{1}{\lambda_D^2}\right)\right). \tag{3.28}$$

### 3.1.4 Description of lifetime

The above expression of the lifetime is the function of the lengths of the specimen. To simplify the analysis in the following, we choose the description of the lifetime using the fragment size, $S = L_xL_y$, and aspect ratio of fragment, $\varphi = L_</L_>$, where $L_<$ ($L_>$) is shorter (longer) length of the edge in $L_x$ and $L_y$. Using $S$ and $\varphi$, we can rewrite Eq. (3.28) into

$$T_b(S,\varphi) = \tau f^{-1}\left(\frac{\sigma_Y}{F_0}\mathcal{F}\left(\frac{2\varphi}{1+\varphi^2}\frac{S}{\lambda_D^2}\right)\right). \tag{3.29}$$

When the shape of fragments is approximated to be isotropic, $\varphi \sim 1$, Eq. (3.29) is reduced to

$$T_b(S) = \tau f^{-1}\left(\frac{\sigma_Y}{F_0}\mathcal{F}\left(\frac{S}{\lambda_D^2}\right)\right). \tag{3.30}$$

Equation (3.29) describes the lifetime as the function of the size and the aspect ratio. The actual lifetime may depend on other quantities characterizing the shape of fragments in much detail. However, when we consider the

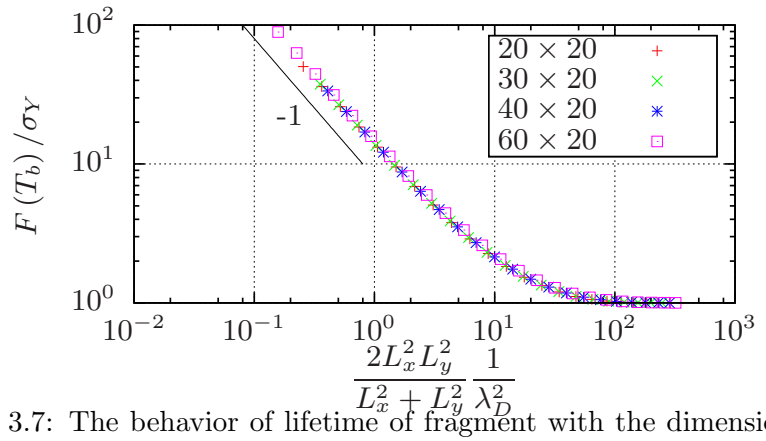


Figure 3.7: The behavior of lifetime of fragment with the dimension $L_x \times L_y = 20 \times 20$, $30 \times 20$, $40 \times 20$, and $60 \times 20$. The difference of color indicates the difference of pairs of $L_x$ and $L_y$. The solid line indicates a power function with the exponent $-1$. The horizontal axis indicates $2L_x^2L_y^2/\left(L_x^2+L_y^2\right)/\lambda_D^2$. The vertical axis indicates $F(T_b)/\sigma_Y$.

fragmentation process taking into account the detail of the shape of fragment except for the size, the investigation may be complicated. As the first step of the investigation of the time evolution of the size distribution, we consider the fragmentation process taking into account the lifetime of Eq. (3.30).

## 3.2 Modified Gibrat process

In the SPH simulations, we found that the dynamical scaling law seems to exist. In this section, let us consider the reason why the dynamical scaling law is obeyed. The SPH simulation is suitable for reproducing the realistic crack pattern. It is, however, not suitable for analyzing the statistical property. It tells the existence of the dynamical scaling law; However, it does not tell the reason. In order to understand the origin of the dynamical scaling law, we propose a stochastic model. The stochastic model also enables us to discuss the statistical property in detail. For this purpose, we modify the Gibrat process. In Chap. 1, we have shown that the size distribution of the original Gibrat process is the lognormal distribution asymptotically and its average size decays exponentially. It is obviously found that the size distribution can not collapse into a master curve by scaling with only the average. That is because the functional form includes two independent parameters of the average and the variance. Therefore the size distribution can not be scaled by using the average alone. However, the Gibrat process is convenient for describing the property of fracturing process. Actually, the Gibrat process is used to describe

the property of collisional process [47], and it describes the power-law distribution which is observed generally in the experiment. We guess that the origin of the dynamical scaling is in the desiccation process of the fragment, especially the lifetime of the fragment. In the desiccation process, the individual fragment has the lifetime depending on the size of fragment as shown in Sect. 3.1. Therefore, the Gibrat process is modified by replacing the constant interval of the breaking event with the size-dependent lifetime, $T_b$. We call the Gibrat process taking into account the size-dependent lifetime the "modified Gibrat process". When we choose the lifetime as a constant function, the modified Gibrat process is completely equivalent to the Gibrat process. Therefore the modified Gibrat process is an extended model of the Gibraat process. The modified Gibrat process is carried out by the numerical computation with a dividing ratio distribution $g(r)$. To simplify the following analysis, we assume the functional form of $T_b$ depending on the size $S$ only. Furthermore, we do not take into account the region of the lifetime where the lifetime becomes constant. That is because the modified Gibrat process with a constant lifetime is completely equivalent to the original Gibrat process. In this section, we describe the modified Gibrat process initially, and analyze it. The time evolutions of average size and size distribution are calculated with the various functions of $T_b$ and $g(r)$. We propose a power function and logarithmic function as the functional form of $T_b(S)$ and the beta distribution as the functional form of $g(r)$. We show the dynamical scaling property on the size distribution in the case that the lifetime is given by a power function.

### 3.2.1 Stochastic modeling

In this section, we describe the modified Gibrat process. First, we define the functional form of the lifetime $T_b(S)$. Second, we propose the functional form of the probability density function of the dividing ratio $g(r)$. Finally, we explain the procedure of the modified Gibrat process.

#### Lifetime of fragment

We derived the lifetime of fragment as a function of size $S$, depending on the functional form of $F(t)$. In this section, we use the functional form of $T_b$ as

$$T_b(S) = \tau \mathcal{T}\left(\frac{S}{\theta}\right), \tag{3.31}$$

where $\mathcal{T}(z)$ is an arbitrary decreasing function. Parameters $\tau$ and $\theta$ are the characteristic time scale and the size scale, respectively. The functional form is chosen to give $\tau$ for the size $\theta$. $\theta$ corresponds to the initial size of the fragment.

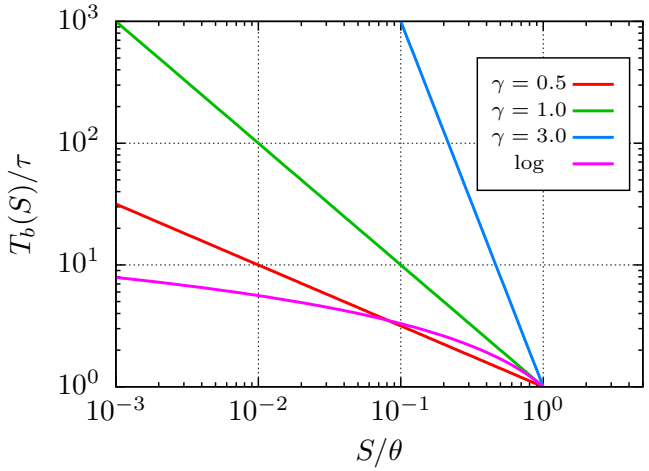


Figure 3.8: The functional form of lifetime $T_b$. The horizontal axis indicates the size $S$ scaled by the characteristic size scale $\theta$. The vertical axis indicates the lifetime $T_b$ scaled by the characteristic time scale $\tau$. The difference of color corresponds to the difference of the functional form of the lifetime. Red, green, and blue lines correspond to the lifetime given by the power function $T_b(S) = \tau (S/\theta)^{-\gamma}$ with $\gamma = 0.5$, 1.0, and 3.0, respectively. The magenta line corresponds to the lifetime given by the logarithmic function $T_b(S) = \tau [1 - \log(S/\theta)]$. This figure is taken from Ref. [94] with permission of Journal of Physical Society of Japan.

As the functional form of $T_b$, we use a power function and a logarithmic function (see Fig. 3.8):

$$T_b(S) = \tau \left(\frac{S}{\theta}\right)^{-\gamma}, \tag{3.32}$$

and

$$T_b(S) = \tau \left[1 - \log\left(\frac{S}{\theta}\right)\right]. \tag{3.33}$$

The modified Gibrat process using $T_b(S) = \tau (S/\theta)^{-\gamma}$ with $\gamma = 0$ is equivalent to the Gibrat process. In the following analysis, we use $\gamma = 0.5$, 1.0, and 3.0 for the exponent of the power function.

### Probability density function of dividing ratio

In the modified Gibrat process, it is required to determine a functional form of the probability density function $g(r)$ of the fragment dividing ratio $r$. In this

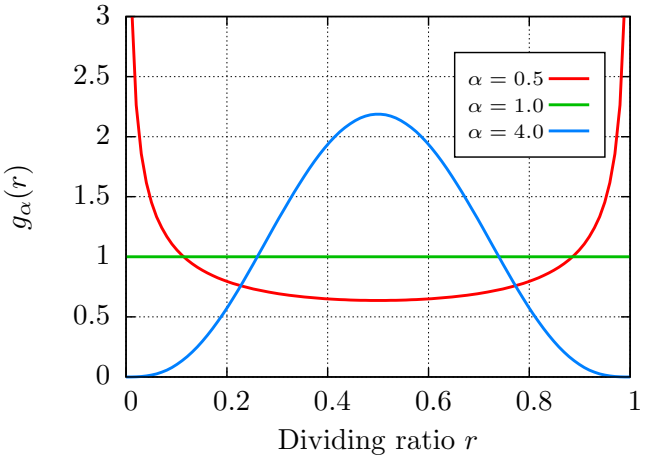


Figure 3.9: Beta distribution as fragment dividing ratio distribution. Red, green, and blue lines correspond to the case of $\alpha = 0.5$, 1.0, and 4.0, respectively. This figure is taken from Ref. [94] with permission of Journal of Physical Society of Japan.

section, we use the probability density function as the beta distribution,

$$g(r) = \frac{1}{B(\alpha,\alpha)} r^{\alpha-1}(1-r)^{\alpha-1}, \tag{3.34}$$

where $r$ is the dividing ratio and $B(\alpha,\alpha) = \int_0^1 dx x^{\alpha-1}(1-x)^{\alpha-1}$ is the beta function for normalization of the distribution (see Fig. 3.9). To simplify the following numerical simulation, we restrict the domain of $g(r)$ to the open interval $r \in (0,1)$. The beta distribution is chosen because the probability density function of the fragment dividing ratio is required to be symmetry with respect to $r = 1/2$ for the conservation of the sum of total fragments. Using the beta distribution as the dividing ratio distribution, we can control the functional form by a single parameter $\alpha$. A uniform distribution is represented for $\alpha = 1$ and a Gaussian-like distribution is represented for much larger $\alpha$. In the following analysis, we use $\alpha = 0.5$, 1.0, and 4.0.

### Model description

The modified Gibrat process is carried out with the following procedure (see Fig. 3.10). There is an initial fragment whose size $S_0$. The fragment has the lifetime $T_b(S_0)$ determined by $S_0$. When $T_b(S_0)$ has passed, the fragment breaks into two fragments with the dividing ratio $r$. The dividing ratio $r$ is randomly chosen from the distribution $g(r)$. The sizes of two fragments are given by $rS_0$ and $(1-r)S_0$ and they have the lifetimes which are given by

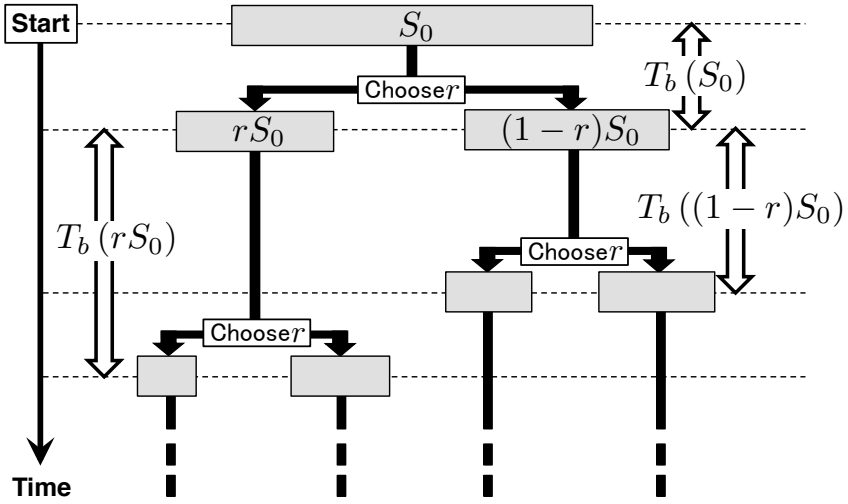


Figure 3.10: Schematic flow diagram of the modified Gibrat process. Initially there is a fragment whose size is $S_0$. The lifetime of the fragment is given by $T_b(S_0)$. When $T_b(S_0)$ has passed, the fragment breaks into two pieces with a random dividing ratio $r$. $r$ is chosen from the probability density function of fragment dividing ratio, $g(r)$. As a result, two fragments whose sizes are $rS_0$ and $(1-r)S_0$ are created. The procedure is iterated for the new fragments with size $rS_0$ whose lifetime is given by $T_b(rS_0)$, and size $(1-r)S_0$ whose lifetime is given by $T_b\,((1-r)S_0)$. This figure is taken from Ref. [94] with permission of Journal of Physical Society of Japan.

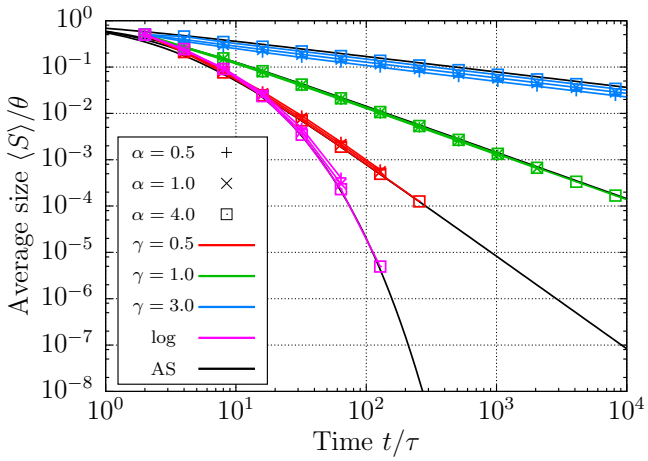


Figure 3.11: Time evolutions of the average size $\langle S\rangle$. The difference of color indicates the difference of the types of functional form of lifetime. Types of point represent the difference of parameter $\alpha$. The black solid lines labeled "AS" show the approximated solutions derived by solving Eq. (3.45) with an appropriate initial condition. This figure is taken from Ref. [94] with permission of Journal of Physical Society of Japan.

$T_b\left(rS_0\right)$ and $T_b\left((1-r)S_0\right)$, respectively. The procedure is repeated to the each new fragment. The statistical properties are calculated on the same time slice.

### 3.2.2 Numerical result

The modified Gibrat process is numerically carried out in this section. As $T_b(S)$, we choose the functional forms given by Eqs. (3.32) and (3.33). In the case that the lifetime is given by a power function, $T_b\left(S\right) = \tau\left(S/\theta\right)^{-\gamma}$, we choose $\gamma = 0.5$, 1.0, and 3.0. And the probability density function of the dividing ratio, $g(r)$, is given by Eq. (3.34) with $\alpha = 0.5$, 1.0, and 4.0. As the initial condition of size $S_0$, we take $S_0 = \theta$. The time evolution of average size and size distribution, which are the average of the independent 50000 samples, are shown in this section.

#### Average size

We define the average size $\langle S\rangle$ obtained by averaging the sizes of the fragments that exist at time $t$. We show the time evolution of average size $\langle S\rangle$ in Fig. 3.11. The difference of color indicates the difference of the types of functional form of lifetime. Types of point represent the difference of parameter $\alpha$. The functional forms of time evolution of average size seem independent of the functional form

of $g(r)$. In addition, the time series of average size can be fitted by

$$\langle S \rangle \propto t^{-1/\gamma}, \tag{3.35}$$

for large $t$, if the lifetime is given by the power function whose exponent is $\gamma$. If the lifetime is given by the logarithmic function, the time series of average size can be fitted by

$$\langle S \rangle \propto \exp\left(-C\sqrt{t}\right), \tag{3.36}$$

where $C$ is a positive fitting parameter, for large $t$. This behavior will be discussed in Sect. 3.2.3.

### Size distribution

Figures 3.12, 3.13, and 3.14 show the time series of size distributions in the case of $T_b(S) = \tau (S/\theta)^{-\gamma}$ with $\gamma = 0.5$, 1.0, and 3.0, respectively. The horizontal axises indicate the scaled size $S/\langle S \rangle$. The vertical axises indicate the probability density function. (a), (b), and (c) in each figure correspond to the cases of $\alpha = 0.5$, 1.0 and 4.0, respectively. Because the dividing ratio $r$ is restricted in the open interval $(0, 1)$, the probability density functions become the obvious form that corresponds to the shape of $g(r)$ at the first break ($t = 2\tau$). We find that the scaled probability density function converges the specific form that is time-invariant as enough time passed. The results predicts the existence of the dynamical scaling law, in which the probability density function $P(S, t)$ can be collapsed into the time-invariant function $\tilde{P}(X)$ with the scaled variable $X = S/\langle S \rangle$:

$$P(S,t)dS = \tilde{P}(X)dX \qquad \text{with} \qquad X = \frac{S}{\langle S \rangle}. \tag{3.37}$$

Figure 3.15 shows the time series of size distributions in the case of $T_b(S) = \tau [1 - \log(S/\theta)]$. The horizontal axises indicate the scaled size $S/\langle S \rangle$. The vertical axises indicate the probability density function. (a), (b), and (c) in each figure correspond to the cases of $\alpha = 0.5$, 1.0 and 4.0, respectively. Because of the same reason in the previous cases, the probability density functions become the obvious form that corresponds to the shape of $g(r)$ at the first break ($t = 2\tau$). We find that the time series of distributions cannot be collapsed into a time-invariant curve in this case. Thus the existence of the dynamical scaling law is denied in this logarithmic lifetime case.

In the original Gibrat process, the asymptotic behavior of size distribution does not depend on the detail of the shape of $g(r)$ but the average and variance; However, we have found that the shape of size distribution in the modified

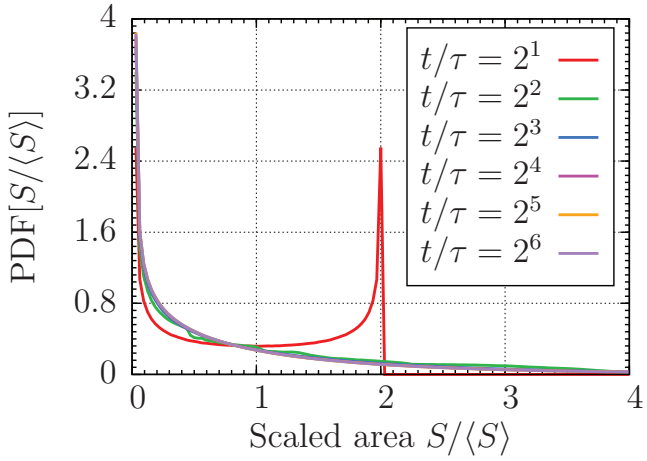


(a) $\alpha = 0.5$

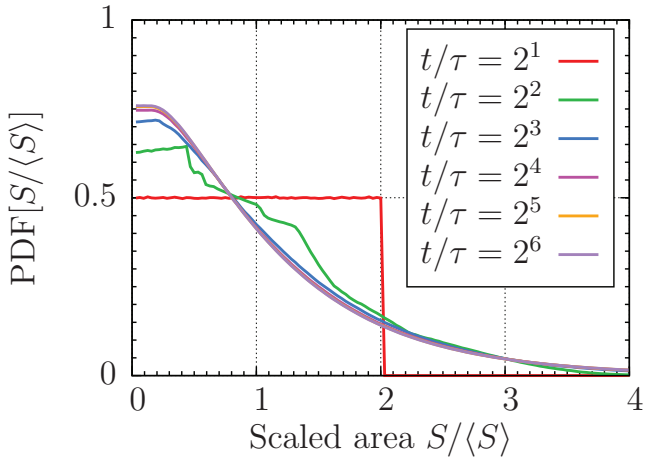


(b) $\alpha = 1.0$

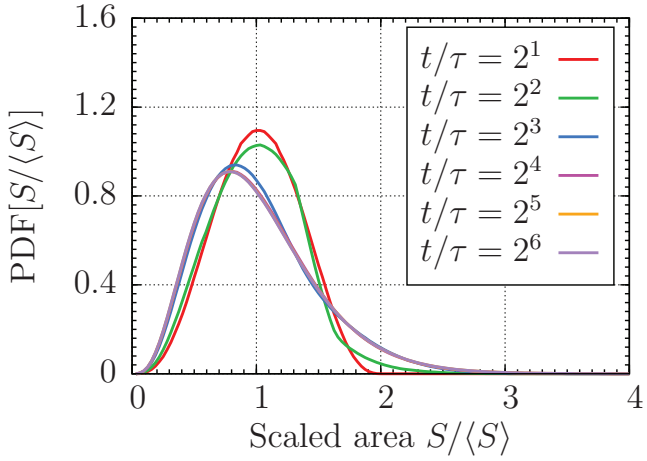


(c) $\alpha = 4.0$

Figure 3.12: The time evolutions of probability density functions (PDFs) of scaled size $S/\langle S\rangle$ with lifetime $T_b(S) = \tau (S/\theta)^{-\gamma}$ and $\gamma = 0.5$. (a), (b) and (c) show the PDFs in the cases of $\alpha = 0.5$, 1.0 and 4.0, respectively. This figure is taken from Ref. [94] with permission of Journal of Physical Society of Japan.

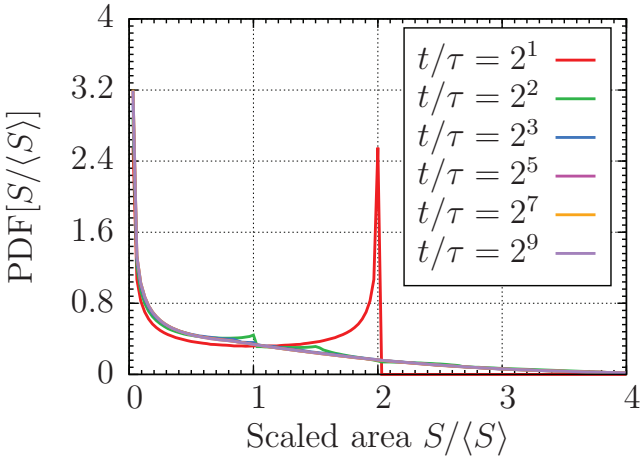


(a) $\alpha = 0.5$

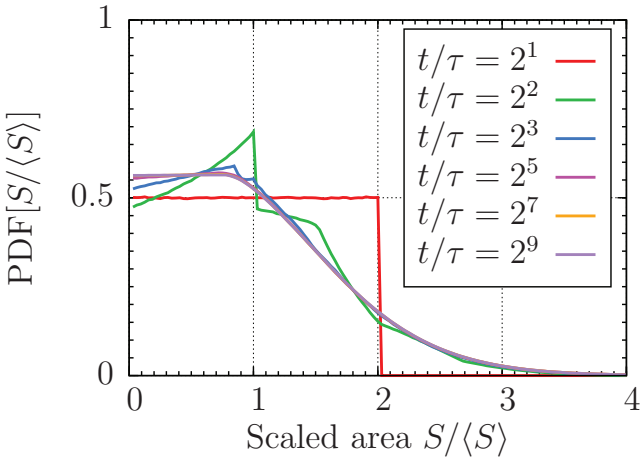


(b) $\alpha = 1.0$

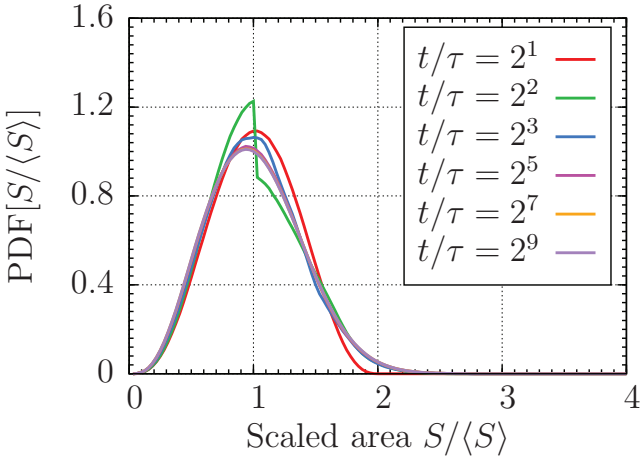


(c) $\alpha = 4.0$

Figure 3.13: The time evolutions of PDFs of scaled size $S/\langle S\rangle$ with lifetime $T_b(S) = \tau (S/\theta)^{-\gamma}$ and $\gamma = 1.0$. (a), (b) and (c) show the PDFs in the cases of $\alpha = 0.5$, 1.0 and 4.0, respectively. This figure is taken from Ref. [94] with permission of Journal of Physical Society of Japan.

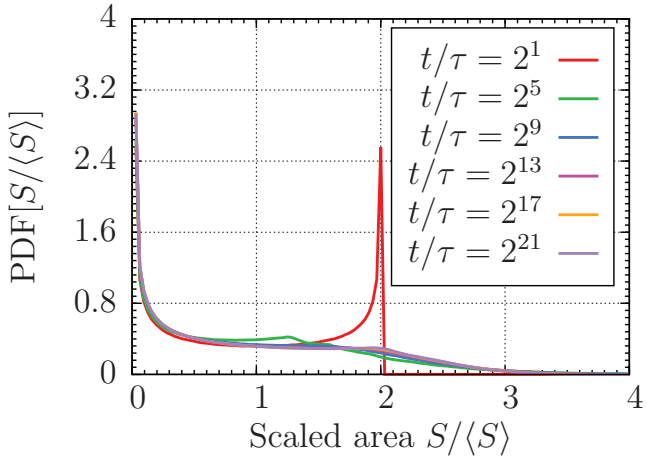


(a) $\alpha = 0.5$

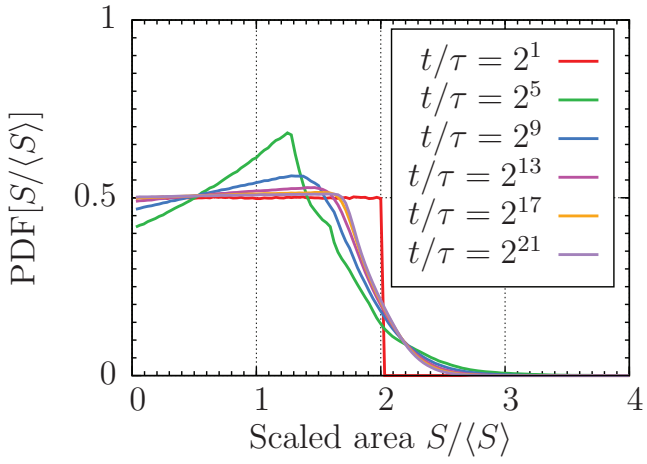


(b) $\alpha = 1.0$

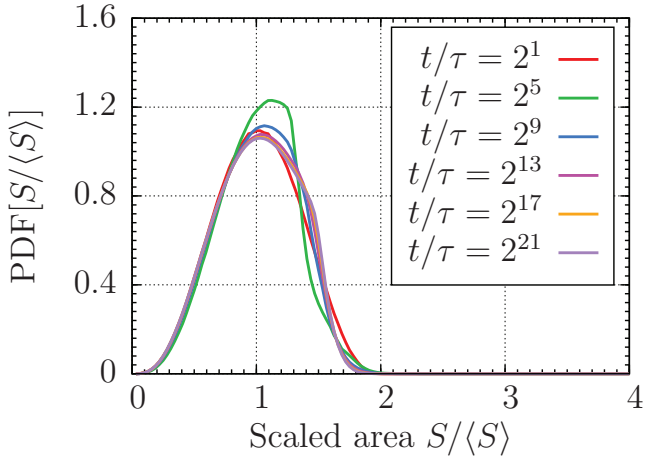


(c) $\alpha = 4.0$

Figure 3.14: The time evolutions of PDFs of scaled size $S/\langle S\rangle$ with lifetime $T_b(S) = \tau (S/\theta)^{-\gamma}$ and $\gamma = 3.0$. (a), (b) and (c) show the PDFs in the cases of $\alpha = 0.5$, 1.0 and 4.0, respectively. This figure is taken from Ref. [94] with permission of Journal of Physical Society of Japan.

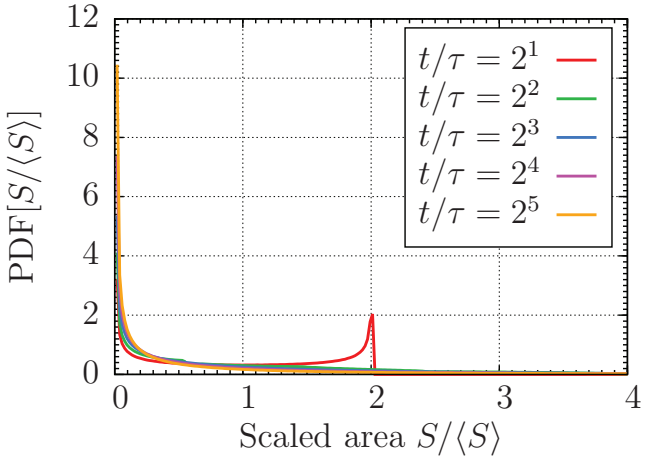


(a) $\alpha = 0.5$

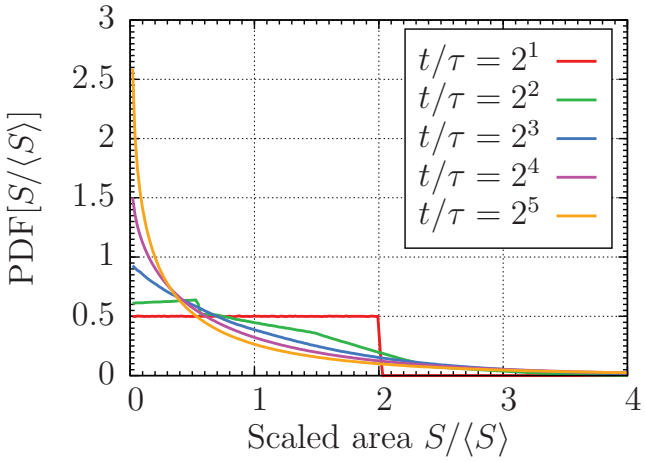


(b) $\alpha = 1.0$

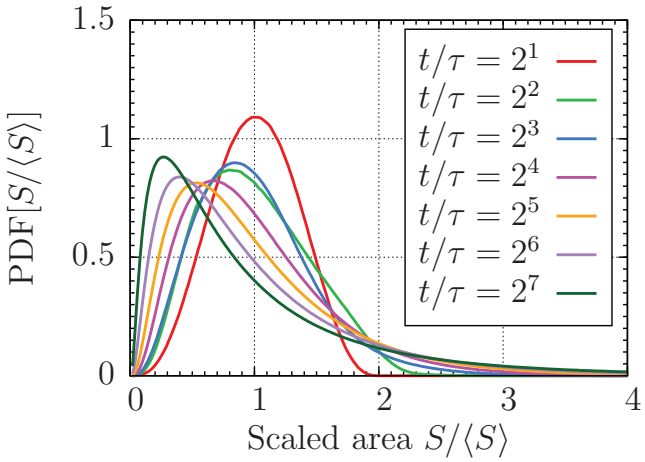


(c) $\alpha = 4.0$

Figure 3.15: The time evolutions of PDFs of scaled size $S/\langle S\rangle$ with lifetime $T_b(S) = \tau[1 - \log(S/\theta)]$. (a), (b) and (c) show the PDFs in the cases of $\alpha = 0.5$, 1.0 and 4.0, respectively. This figure is taken from Ref. [94] with permission of Journal of Physical Society of Japan.

Gibrat process depends on the shape of $g(r)$. Therefore we need to choose carefully the shape of $g(r)$ when we compare the theoretical results with the experimental results. According to the using another shape of $g(r)$, we have confirmed that the existence of the dynamical scaling property is independent of the shape of $g(r)$. The reason is explained analytically in Sect. 3.3.

### 3.2.3 Analysis

Behavior of the time evolution of the average size is understood by the following analysis. Let $n$ denote the number of breaking event that a fragment is experienced from the beginning until the time $t$. Let $S_n$ and $t_n$ the size and the elapsed time when the $n$-th breaking event has finished, respectively. When the $n$-th breaking event has finished, the size of the fragment $S_n$ can be described by

$$S_n = r_n S_{n-1} = \cdots = S_0 \Pi_{i=0}^{n-1} r_i, \tag{3.38}$$

where $r_i$ denotes the dividing ratio of $i$-th breaking event. $S_0$ denotes the initial size. In addition, the elapsed time $t_n$ can be described by as sum of the lifetime as

$$t_n = \sum_{i=0}^{n-1} T_b\left(S_i\right). \tag{3.39}$$

Let us change the variable $S_i$ to $Z_i = \log S_i$. And we write $T_b(S_i)$ as a function of $Z_i$, which is denoted by $W(Z_i)$. Then the size $S_n$ and the elapsed time $t_n$ are rewritten as

$$\log S_n = Z_n = \log r_n + Z_{n-1} = \cdots = Z_0 + \sum_{i=0}^{n-1} \log r_i, \tag{3.40}$$

and

$$t_n = \sum_{i=0}^{n-1} W\left(Z_i\right). \tag{3.41}$$

Here we approximate $r_i$ to its average $1/2$ for all $i$. As $|Z_{i+1} - Z_i| = |\log\left(S_{i+1}/S_i\right)| \sim \log 2$, Eq. (3.41) can be approximated by the following integral:

$$\begin{aligned} t_n &\sim \int_{Z_0}^{Z_n} \frac{dZ}{-\log 2} W(Z) \\ &= -\frac{1}{\log 2} \int_{S_0}^{S_n} \frac{dS}{S} T_b\left(S\right). \end{aligned} \tag{3.42}$$

Assuming the discrete variables $(t_n, S_n)$ to be the continuous variables $(t, S)$, we obtain

$$t = -\frac{1}{\log 2}\int_{S_0}^{S}\frac{dS}{S}T_b\left(S\right). \tag{3.43}$$

Differentiating Eq. (3.43) with respect to $S$, the following equation is obtained:

$$\frac{dS}{dt} = -\log 2\frac{S}{T_b\left(S\right)}. \tag{3.44}$$

Equation (3.44) is obtained by approximating the dividing ratio $r$ to $1/2$. $S$ is originally a stochastic variable. Here, however, $S$ should be treated as the average $\langle S\rangle$ because of the approximation $r_i \sim 1/2$. As a consequence, $\langle S\rangle$ evolves approximatelly with the following equation:

$$\frac{d\left\langle S\right\rangle}{dt} = -\log 2\frac{\left\langle S\right\rangle}{T_b\left(\left\langle S\right\rangle\right)}. \tag{3.45}$$

With the initial condition $\langle S\rangle = \theta$ at $t = 0$, Eq. (3.45) is solved analytically. The time evolution of average size $\langle S\rangle$ is also given by

$$\left\langle S\right\rangle = \theta\left[\gamma\log 2\left(\frac{t}{\tau}\right)+1\right]^{-1/\gamma}, \tag{3.46}$$

if the lifetime is given by $T_b\left(S\right) = \tau\left(S/\theta\right)^{-\gamma}$ for positive $\gamma$. For the logarithmic lifetime $T_b\left(S\right) = \tau\left[1-\log\left(S/\theta\right)\right]$, the time evolution of average size $\langle S\rangle$ is given by

$$\left\langle S\right\rangle = \theta\exp\left[1-\sqrt{1+2\log 2\left(\frac{t}{\tau}\right)}\right]. \tag{3.47}$$

The black solid lines labeled "AS" in Fig. 3.11 are described by Eq. (3.46) for $\gamma = 0.5$, 1.0, and 3.0 and Eq. (3.47). They are quantitatively consistent with the numerical results.

## 3.3 Markovianized modified Gibrat process

Using the modified Gibrat process, it is found that the dynamical scaling law is obeyed in the case that the lifetime is given by a power function of the fragment size. And, in the case that the lifetime is given by a logarithmic function, there is no dynamical scaling property in the time series of the size distributions. If we

could investigate the modified Gibrat process analytically, we could understand the origin of the dynamical scaling property in the case that the lifetime is given by a power function. However, the modified Gibrat process is not suitable to analyze the origin of the scaling. That is because the modified Gibrat process has a strong non-Markovian property. Here we make the modified Gibrat process be a much simpler model in order to investigate the origin of the dynamical scaling. In this section, we "markovianize" the modified Gibrat process by approximating to the Poisson process. In the Poisson process, the characteristic time scale is given by a constant. The lifetime $T_b(S)$ represented in the previous section can be regarded as the characteristic time of decreasing of the probability $P(S,t)$. Replacing the characteristic time scale with the present lifetime $T_b(S)$, we make the markovianized modified Gibrat process.

In this section, we show the theoretical and numerical results of the investigation of the markovianized modified Gibrat process. First, we propose the markovianized modified Gibrat process as the master equation. Using the master equation, we perform a scaling analysis which expresses the dynamical scaling propertsy in the size distribution. Next, we show the exact calculation of the markovianized modified Gibrat process with a constant lifetime. In the process, the size distribution becomes a lognormal distribution just like the original Gibrat process. Finally, we investigate the size distribution and the average size numerically, and predict the scaling form of the size distribution. The validity of the functional form is confirmed by the exact solution of the markovianized modified Gibrat process over a power function of lifetime and a uniform distribution for the probability density function of dividing ratio.

### 3.3.1 Modeling of master equation

Let us consider an elementary process of the fragmentation (see Fig. 3.16). In Fig. 3.16, the circles mean the groups of fragments which have same fragment size. The existence probability of fragment with the size $S'$ transits to that of fragment with the size $S$ by dividing with the ratio $r$ in the average interval $T_b(S')$. This corresponds to the inflow of probability. In addition, the existence probability of fragment with the size $S$ decays in the average interval $T_b(S)$. This corresponds to the outflow of probability.

The existence probability of fragment with the size $S$ at time $t$ denoted as $P(S,t)$ decays with the characteristic time $T_b(S)$. Therefore the outflow of $P(S,t)$ can be described by

$$-\frac{P\left(S,t\right)}{T_b\left(S\right)}. \tag{3.48}$$

The inflow of $P(S,t)$ is represented by summing up the contributions of outflow

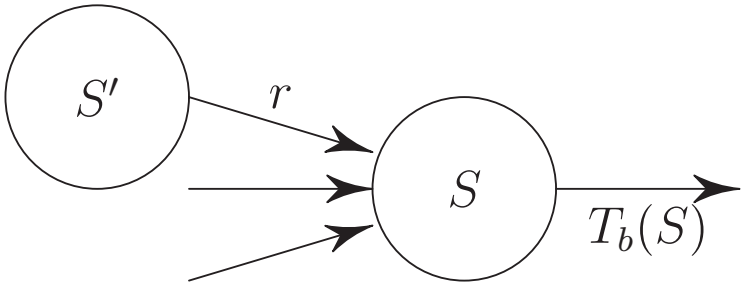


Figure 3.16: Schematic diagram of markovianized modified Gibrat process. The circles mean the existence of probability of fragments with the size $S$ or $S'$. The existence probability of fragment with the size $S'$ contributes to that of fragment with the size $S$ with the weight of the dividing ratio $r$ in the average interval $T_b(S')$. This corresponds to incoming probability to the one of $S$. In addition, the existence probability of fragment with the size $S$ decays in the average interval $T_b(S)$. This corresponds to outgoing probability from the one of $S$.

of the existence probabilities of fragments having other sizes as

$$\int_0^\infty dS' w_{S'\to S} \frac{P\left(S',t\right)}{T_b\left(S'\right)}, \tag{3.49}$$

where $w_{S'\to S}$ is the transition probability from the size $S'$ to $S$. The transition probability must satisfy a conservation of probability:

$$\int_0^\infty dS' w_{S'\to S} = 1. \tag{3.50}$$

Let $r$ and $g(r)$ denote the dividing ratio and the probability density function of the dividing ratio. Because $r$ describes the dividing ratio, $r$ should be defined in the open interval $(0,1)$. $g(r)$ should be satisfied the conservation law:

$$\int_0^1 drg(r) = 1. \tag{3.51}$$

Using $g(r)$, $w_{S'\to S}$ is described by

$$w_{S'\to S} = \int_0^1 drg(r)\delta(rS' - S), \tag{3.52}$$

where $\delta(z)$ is the delta function. The conservation of probability, Eq. (3.50), is satisfied by the expression of Eq. (3.52).

Using Eqs. (3.48), (3.49) and (3.52), the master equation is described by

$$\frac{\partial P\left(S,t\right)}{\partial t} = -\frac{P\left(S,t\right)}{T_b\left(S\right)} + \int_0^\infty dS' \int_0^1 drg\left(r\right)\delta\left(rS' - S\right)\frac{P\left(S',t\right)}{T_b\left(S'\right)}. \tag{3.53}$$

The conservation of probability of $P(S,t)$ is easily checked as follows:

$$\begin{aligned}
&\int_0^\infty dS \frac{\partial P\left(S,t\right)}{\partial t} \\
&= -\int_0^\infty dS \frac{P\left(S,t\right)}{T_b\left(S\right)} + \int_0^\infty dS \int_0^\infty dS' \int_0^1 drg\left(r\right)\delta\left(rS'-S\right)\frac{P\left(S',t\right)}{T_b\left(S'\right)} \\
&= -\int_0^\infty dS \frac{P\left(S,t\right)}{T_b\left(S\right)} + \int_0^\infty dS' \int_0^1 drg\left(r\right)\frac{P\left(S',t\right)}{T_b\left(S'\right)} \\
&= -\int_0^\infty dS \frac{P\left(S,t\right)}{T_b\left(S\right)} + \int_0^\infty dS' \frac{P\left(S',t\right)}{T_b\left(S'\right)} = 0.
\end{aligned} \tag{3.54}$$

### 3.3.2 Scaling analysis

Let us consider the condition to realize a dynamical scaling law in Eq. (3.53) by using a scaling analysis. We require that Eq. (3.53) is invariant under the scaling transformation $P(S,t) \to P(\xi S, \zeta t) = \bar{P}(S,t)$. Replacing $S$ and $t$ with $\xi S$ and $\zeta t$ in Eq. (3.53), we obtain a time evolution of $\bar{P}(S,t)$ as

$$\frac{\partial \bar{P}\left(S,t\right)}{\partial t} = -\zeta\frac{\bar{P}\left(S,t\right)}{T_b\left(\xi S\right)} + \zeta\int_0^\infty dS' \int_0^1 drg\left(r\right)\delta\left(rS'-S\right)\frac{\bar{P}\left(S',t\right)}{T_b\left(\xi S'\right)}. \tag{3.55}$$

From Eq. (3.55), the condition of invariance of Eq. (3.53) under the scaling transformation is obtained as

$$\frac{\zeta}{T_b(\xi S)} = \frac{1}{T_b(S)}. \tag{3.56}$$

This is the necessary and sufficient condition of the invariance and implies

$$T_b(S) \propto S^{-\gamma}, \tag{3.57}$$

where $\gamma \equiv -T_b'(1)/T_b(1)$ and

$$\zeta = \xi^{-\gamma}. \tag{3.58}$$

Therefore the dynamical scaling law comes from the power-function lifetime $T_b(S)$. In addition, it is independent of the functional form of $g(r)$.

The similarity solution is given by as follows: First we start the distribution is invariant under the scaling transformation:

$$P(S,t)dS = \xi P(\xi S, \zeta t)dS. \tag{3.59}$$

Substituting Eq. (3.58) into Eq. (3.59), for non zero $\gamma$, we obtain

$$P(S,t)dS = \zeta^{-1/\gamma} P(\zeta^{-1/\gamma} S, \zeta t)dS. \tag{3.60}$$

Eliminating the second argument by taking $\zeta = 1/t$ in Eq. (3.60), we obtain the similarity solution as

$$P(S,t)dS = t^{1/\gamma}P(t^{1/\gamma}S,1)dS. \tag{3.61}$$

Next, let us discuss the average size $\langle S\rangle = \int_0^\infty dS\ SP(S,t)$ by using a scaling analysis. Substituting the scaling relation, Eq. (3.59), into the definition of $\langle S\rangle$, we obtain

$$\langle S\rangle = \xi \int_0^\infty dSSP(\xi S,\zeta t) = \mathcal{A}(t), \tag{3.62}$$

where $\mathcal{A}(t)$ represents that $\langle S\rangle$ is a function of $t$, explicitly. Replacing $\xi S$ with $z$ and taking $t = 1$, Eq. (3.62) gives

$$\mathcal{A}(1) = \xi^{-1} \int_0^\infty dzzP(z,\zeta) = \zeta^{1/\gamma}\mathcal{A}(\zeta), \tag{3.63}$$

where we use the relation, Eq. (3.58), for non-zero $\gamma$. Thus $\langle S\rangle$ is given by

$$\langle S\rangle = \mathcal{A}(1)t^{-1/\gamma}. \tag{3.64}$$

Eliminating $t$ of Eq. (3.61) by Eq. (3.64), the dynamical scaling law is obtained as follows:

$$\begin{aligned} P(S,t)dS &= \mathcal{A}(1)P\left(\mathcal{A}(1)\frac{S}{\langle S\rangle},1\right)\frac{dS}{\langle S\rangle} \\ &= \tilde{P}\left(X\right)dX \qquad \text{with } X = \frac{S}{\langle S\rangle}. \end{aligned} \tag{3.65}$$

### 3.3.3 Markovianized modified Gibrat process with a constant lifetime

When the lifetime is constant, $T_b(S) = \tau$, the master equation can be solved exactly. The markovianized modified Gibrat process with a constant lifetime corresponds to the original Gibrat process, We assume the initial condition of $P(S,t)$ is given by $P(S,0) = \delta(S - S_0)$. The variables, $S$ and $t$, are normalized by $S_0$ and $\tau$.

#### Exact solution

The master equation of the markovianized modified Gibrat process with a constant lifetime is given by

$$\frac{\partial P(S,t)}{\partial t} = -P(S,t) + \int_0^1 \frac{dr}{r}g(r)P\left(\frac{S}{r},t\right). \tag{3.66}$$

With an initial condition, $P(S,0) = \delta(S-1)$, its exact solution is given by

$$P(S,t) = \frac{1}{2\pi S}\int_{-\infty}^{\infty} dk\ \exp\left[ik\log S + (w(k)-1)\,t\right], \tag{3.67}$$

where

$$w(k) = \int_0^1 drg(r)\exp\left(-ik\log r\right). \tag{3.68}$$

The derivation is shown in App. A.1. Note that the exact solution can include the arbitrary functional form of $g(r)$. Equation (3.67) can describes the transient of the solution from the initial distribution to the asymptotic one. However, Eq. (3.67) includes the integral in the complex domain which is difficult to solve in general. We may have to rely on the numerical computation to evaluate the complex integral.

### Asymptotic behavior

Let us consider the asymptotic behavior of Eq. (3.67). In order to derive the asymptotic solution of Eq. (3.67), we assume the following normalization between $S$ and $t$:

$$y = \frac{\log S - tm_1}{\sqrt{tm_2}}, \tag{3.69}$$

where

$$m_1 = \int_0^1 drg(r)\log r, \tag{3.70}$$

and

$$m_2 = \int_0^1 drg(r)(\log r)^2. \tag{3.71}$$

Then we can obtain the normal distribution of $y$ as the asymptotic behavior of $P(S,t)$ with $t\to\infty$. Thus

$$P(S,t) = \frac{1}{\sqrt{2\pi tm_2}S}\exp\left[-\frac{(\log S - tm_1)^2}{2tm_2}\right]. \tag{3.72}$$

The details are shown in App. A.2. Equation (3.72) describes a lognormal distribution just like the original Gibrat process; However, the parameters characterizing the functional form are slightly different.

### 3.3.4 Preparation for numerical computation

The master equation for the size distribution of desiccation crack pattern is given by Eq. (3.53) or the form that we evaluate the $r$ integral as

$$\frac{\partial P(S,t)}{\partial t} = -\frac{P(S,t)}{T_b(S)} + \int_S^\infty \frac{dS'}{S'} g\left(\frac{S}{S'}\right) \frac{P(S',t)}{T_b(S')}. \tag{3.73}$$

In general, $T_b(S)$ and $g(r)$ are nonlinear functions. It is difficult to solve Eq. (3.53) or Eq. (3.73) analytically. Therefore it is necessary to analyze them numerically for understanding the behavior of their solutions. To compute Eq. (3.73), we first nondimensionalize it. Next we discretize the integral with the double exponential formula.

As the functions of $T_b$, power functions and logarithm function are used as follows:

$$T_b(S) = \tau \left(\frac{S}{S_0}\right)^{-\gamma}, \tag{3.74}$$

and

$$T_b(S) = \tau \left[1 - \log\left(\frac{S}{S_0}\right)\right]. \tag{3.75}$$

As the function of $g(r)$, we use the beta distribution:

$$g(r) = \frac{1}{B(\alpha,\alpha)} r^{\alpha-1}(1-r)^{\alpha-1}, \tag{3.76}$$

where $B(\alpha,\alpha) = \int_0^1 dr\, r^{\alpha-1}(1-r)^{\alpha-1}$ is the beta function.

#### Non-dimensionalization

Let us start with Eq. (3.73). We define $S_0$ as the largest size whose existence probability is non-zero at the initial state. According to the form of Eq. (3.73), we understand immediately that the probability at the larger size than $S_0$ is always zero. Thus we can change the integral region of Eq. (3.73) from $(S,\infty)$ to $(S,S_0)$. Furthermore when we use non dimensional variable, $x = S/S_0$, we can rewrite Eq. (3.73) to

$$\frac{\partial P(x,t)}{\partial t} = -\frac{P(x,t)}{\tilde{T}_b(x)} + \int_x^1 \frac{dx'}{x'} g\left(\frac{x}{x'}\right) \frac{P(x',t)}{\tilde{T}_b(x')}, \tag{3.77}$$

where $P(x,t) = S_0 P(xS_0,t)$ and $\tilde{T}_b(x) = T_b(xS_0)/\tau$. The time $t$ is nondimensionalized by $\tau$. $x$ is defined in the open interval $(0,1)$. Here we note that there are some cases that the integrand becomes singular at $x = 0$ or 1.

### The double exponential formula

The double exponential formula [95] is one of the most effective formulation for numerically integrating a function which has the singularity at the edge of integral region. When we integrate a function $f(x)$ defined by $x \in (0,1)$, the variable transformation of the double exponential formula is given by

$$x = \phi(z) = \frac{1}{2}\tanh\left(\frac{\pi}{2}\sinh(z)\right) + \frac{1}{2} \qquad \text{for} \quad z \in (-\infty, \infty). \tag{3.78}$$

This formula realizes the super-exponential increasing of the number of integral points near the edge of integral region. Therefore it is effective and efficient for the integration of the singular function.

Using Eq. (3.78), we can describe an integral of $f(x)$ as follows:

$$\begin{aligned}\int_0^1 dx f(x) &= \int_{-\infty}^{\infty} dz \phi'(z) f(\phi(z)) \\ &= \int_{-\infty}^{\infty} dz \frac{\pi}{4} \frac{\cosh(z)}{\cosh^2\left(\frac{\pi}{2}\sinh(z)\right)} f\left(\frac{1}{2}\tanh\left(\frac{\pi}{2}\sinh(z)\right) + \frac{1}{2}\right) \\ &= \int_{-\infty}^{\infty} dz \mathcal{F}(z),\end{aligned} \tag{3.79}$$

where we write the integrand as $\mathcal{F}(z)$. When we deal with Eq. (3.79) numerically, we have to discretize Eq. (3.79) by using a discretization length $\Delta z$. Thus Eq. (3.79) is approximated by

$$\begin{aligned}\int_0^1 dx f(x) &\sim \sum_{k=-\infty}^{\infty} \mathcal{F}(k\Delta z)\Delta z \\ &\sim \sum_{k=-k_m}^{k_m} \mathcal{F}(k\Delta z)\Delta z\end{aligned} \tag{3.80}$$

where $k_m$ is a cutoff number to change the infinite sum to finite one.

### Discretization of master equation

Using the discretization formula Eq. (3.80), we can discretize Eq. (3.77) to

$$\frac{\partial P_i(t)}{\partial t} = -\frac{P_i(t)}{\tilde{T}_b(\phi(z_i))} + \Delta z \sum_{k=i}^{k_m} \omega_i^{k_m}(k) \frac{\phi'(z_k)}{\phi(z_k)} g\left(\frac{\phi(z_i)}{\phi(z_k)}\right) \frac{P_k(t)}{\tilde{T}_b(\phi(z_k))}, \tag{3.81}$$

where $z_k = k\Delta z$ and $P_k(t) = P(\phi(z_k), t)$. The integer $i$ is defined in the closed interval $[-k_m, k_m]$. $\omega$ is a weight function introduced to decrease the error of numerical integration to $O(\Delta z^2)$ from $O(\Delta z)$ and defined by

$$\omega_i^j(k) = \begin{cases} \frac{1}{2} & \text{for } k = i \text{ or } j \\ 1 & \text{otherwise} \end{cases}. \tag{3.82}$$

This is called the trapezoidal rule [96].

### 3.3.5 Numerical result

In this section, we show the numerical results of time evolution of Eq. (3.77). In the following calculation, we use $k_m \Delta z = 3.16$ and $k_m = 2^8$. Time evolution is calculated by means of Jameson-Baker's Runge-Kutta method [85] by using a time step $\Delta t = 0.1$. The time step is determined by $0.1 \times \min\left[\tilde{T}_b(x); x \in (0,1)\right] = 0.1$. The conservation of probability of $P(x,t)$ is exactly satisfied according to Eq. (3.53); However the discretized formula, Eq. (3.81), may not be satisfied in the actual computation because of the accumulation of error. To keep the conservation law, we renormalize artificially $P_i(t)$ in the every time step as

$$P_i(t) \to \frac{P_i(t)}{\Delta z \sum_{k=-k_m}^{k_m} \omega_{-k_m}^{k_m}(k)\, \phi'(z_k)\, P_k(t)}. \tag{3.83}$$

#### Average size

An average size is defined by

$$\langle x \rangle = \int_0^1 dx x P(x,t) \sim \Delta z \sum_{k=-k_m}^{k_m} \omega_{-k_m}^{k_m}(k)\, \phi(z_k)\, P_k(t)\, \phi'(z_k). \tag{3.84}$$

We show the time evolution of the average size in Fig. 3.17. Difference in color indicates difference of the types of the functional form of the lifetime. Types of line represent results of the different parameter $\alpha$. They correspond qualitatively to the behaviors of the average size of the modified Gibrat process. In the modified Gibtat process, the behaviors of the average size with the same function of the lifetime are nearly independent of $\alpha$. However, in the markovianized modified Gibrat process, the behaviors of the average size are systematically dependent on $\alpha$. In the same function of lifetime, the larger $\alpha$ seems to represent the larger average size.

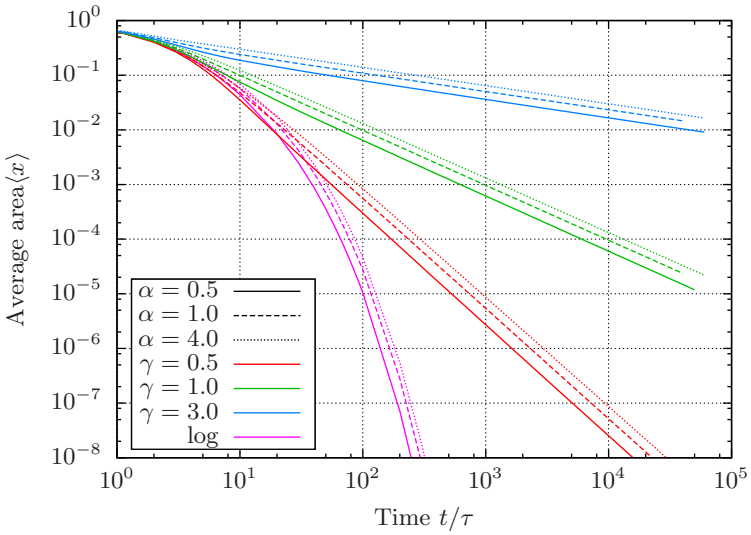


Figure 3.17: Time evolutions of average size $\langle x \rangle$. Difference in color indicates difference of the functional form of lifetime. Types of line represent the parameter $\alpha$.

### Size distribution

We show the time evolutions of size distributions in Figs. 3.18, 3.19 and 3.20, in the cases of $\tilde{T}_b(x) = x^{-\gamma}$ and $\gamma = 0.5$, 1.0 and 3.0. (a), (b) and (c) in each figure correspond to the cases of $\alpha = 0.5$, 1.0 and 4.0. Difference of colors of lines indicate the difference of elapsed time $t/\tau$. All distributions in Figs. 3.18, 3.19 and 3.20 can be observed that they obey the dynamical scaling law as time passes:

$$P(x,t)dx = \mathcal{P}(X)dX \quad \text{with} \quad X = \frac{x}{\langle x \rangle}. \tag{3.85}$$

In addition, as the asymptotic behavior, the distribution obeys the following form:

$$\mathcal{P}(X) \propto \begin{cases} X^{\alpha-1} & \text{for} \quad X \ll 1 \\ \exp\left(-CX^{\gamma}\right) & \text{for} \quad X \gg 1, \end{cases} \tag{3.86}$$

where $C$ is a positive fitting parameter depending on $\gamma$ and $\alpha$.

In Fig. 3.21, the time evolutions of size distributions are shown in the cases of $\tilde{T}_b(x) = 1 - \log x$. Difference of colors of lines indicate the difference of elapsed time $t/\tau$. (a), (b) and (c) in Fig. 3.21 correspond to the cases of $\alpha = 0.5$, 1.0 and 4.0. All distributions grow divergently at the small size. Therefore they do not obey the dynamical scaling law.

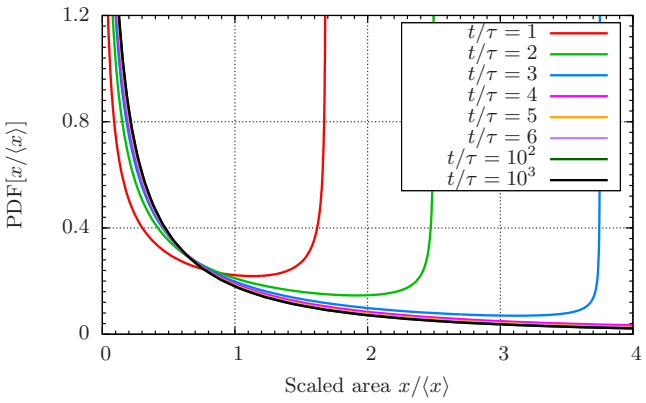


(a) $\alpha = 0.5$

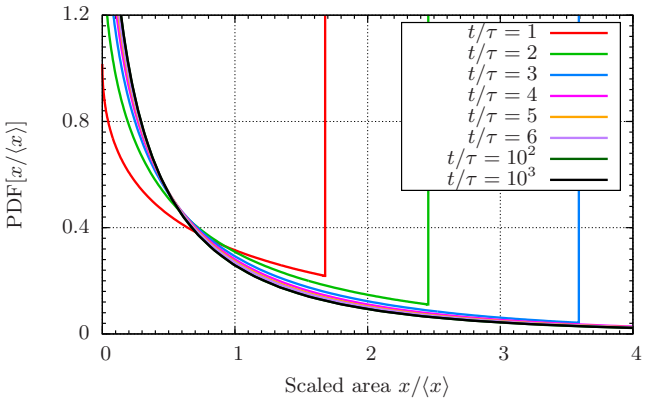


(b) $\alpha = 1.0$

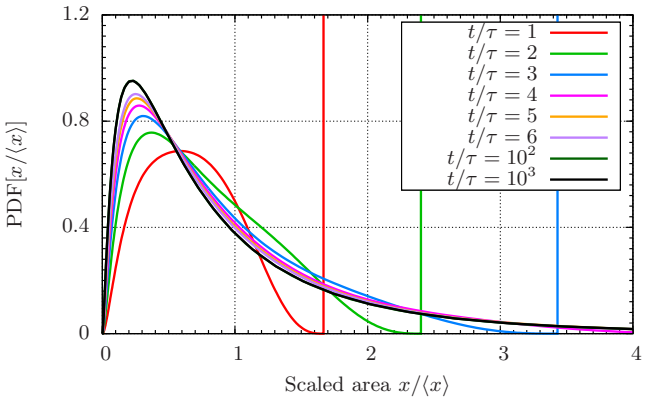


(c) $\alpha = 4.0$

Figure 3.18: The time evolutions of the probability density functions (PDFs) of the scaled size $x/\langle x\rangle$ with the lifetime $\tilde{T}_b(x) = x^{-\gamma}$ and $\gamma = 0.5$. (a), (b) and (c) show the PDFs in the cases of $\alpha = 0.5$, 1.0 and 4.0, respectively.

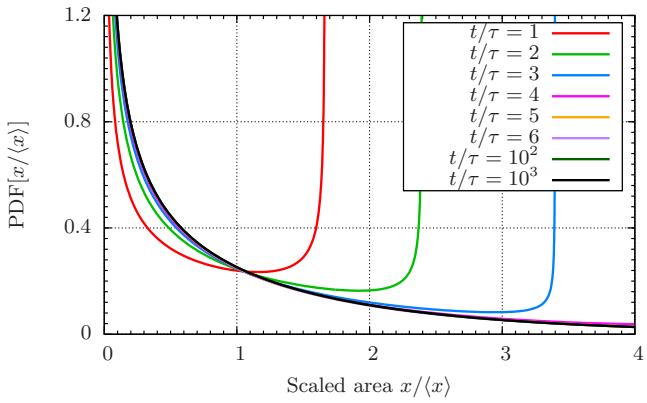


(a) $\alpha = 0.5$

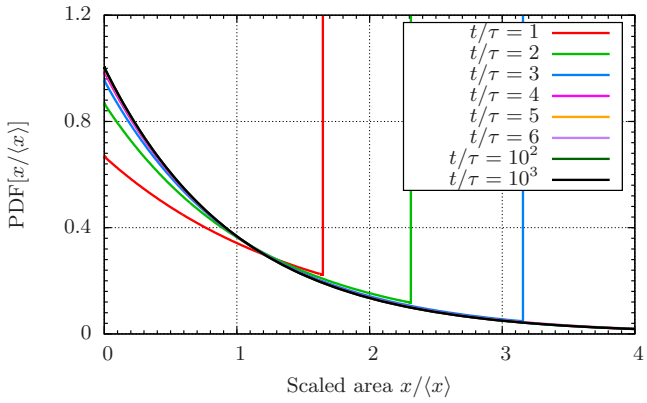


(b) $\alpha = 1.0$

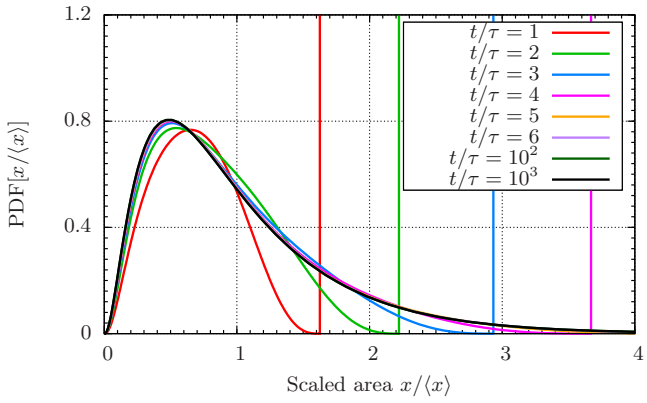


(c) $\alpha = 4.0$

Figure 3.19: The time evolutions of the PDFs of the scaled size $x/\langle x\rangle$ with the lifetime $\tilde{T}_b(x) = x^{-\gamma}$ and $\gamma = 1.0$. (a), (b) and (c) show the PDFs in the cases of $\alpha = 0.5$, 1.0 and 4.0, respectively.

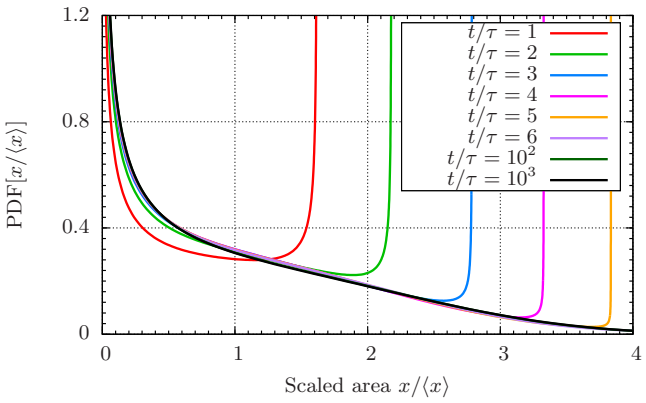


(a) $\alpha = 0.5$

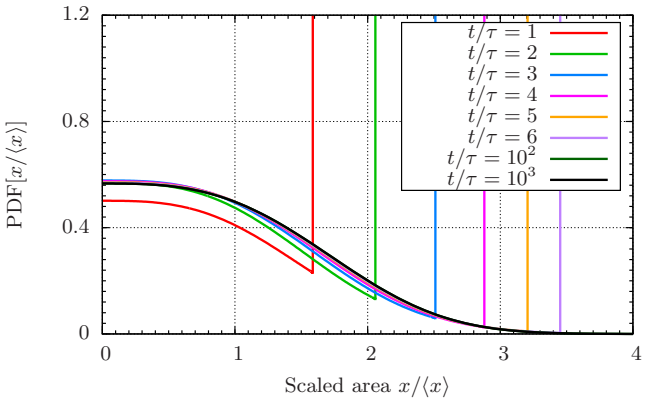


(b) $\alpha = 1.0$

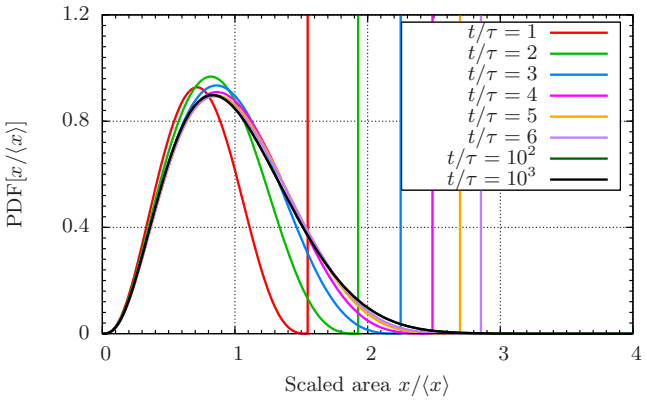


(c) $\alpha = 4.0$

Figure 3.20: The time evolutions of the PDFs of the scaled size $x/\langle x\rangle$ with the lifetime $\tilde{T}_b(x) = x^{-\gamma}$ and $\gamma = 3.0$. (a), (b) and (c) show the PDFs in the cases of $\alpha = 0.5$, 1.0 and 4.0, respectively.

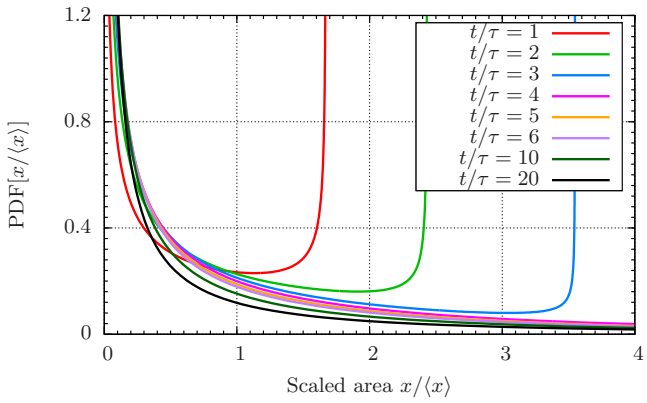


(a) $\alpha = 0.5$

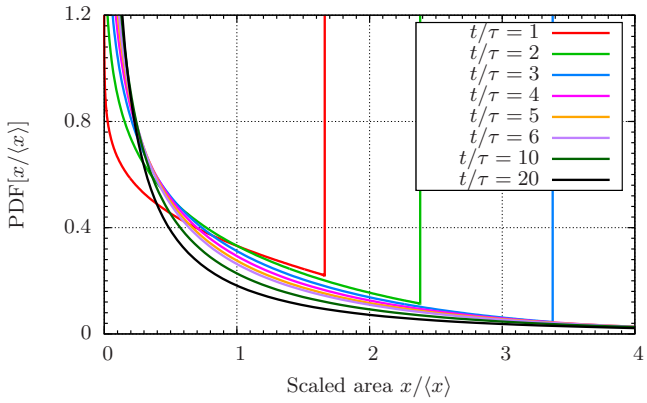


(b) $\alpha = 1.0$

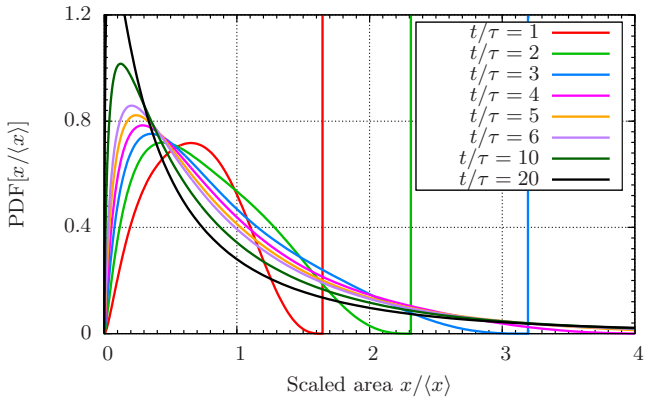


(c) $\alpha = 4.0$

Figure 3.21: The time evolutions of the PDFs of the scaled size $x/\langle x\rangle$ with the lifetime $\tilde{T}_b(x) = 1 - \log x$. (a), (b) and (c) show the PDFs in the cases of $\alpha = 0.5$, 1.0 and 4.0, respectively.

### 3.3.6 Asymptotic solution

In this section, we derive the asymptotic behavior of $\langle x \rangle$ and $P(x,t)$. It is difficult to solve the master equation (3.53) using general $g(r)$ or $\tilde{T}_b(x)$. Therefore we solve analytically the master equation in a simple case, $\tilde{T}_b(x) = x^{-\gamma}$ and $g(r) = 1$.

When $\tilde{T}_b(x) = x^{-\gamma}$ for a positive $\gamma$, according to the numerical results, the average size $\langle S \rangle$ should be

$$\langle x \rangle = \frac{1}{a}\left(\frac{t}{\tau}\right)^{-1/\gamma}, \tag{3.87}$$

asymptotically, where $a$ is a constant. We consider a variable transformation which are given by

$$\begin{cases} X = x/\langle x \rangle = a\,(t/\tau)^{1/\gamma}\,x \\ T = \dfrac{1}{\gamma}\log\dfrac{t}{\tau}. \end{cases} \tag{3.88}$$

Let $\mathcal{P}(X,T) = P(x,t)\dfrac{dx}{dX}$ denote the scaled size distribution. $\mathcal{P}(X,T)$ satisfies the obvious conditions which are given by

$$\int_0^\infty dx P(x,t) = \int_0^\infty dX \mathcal{P}(X,T) = 1, \tag{3.89}$$

and

$$\int_0^\infty dx\; xP(x,t) = \langle x \rangle \Leftrightarrow \int_0^\infty dX X\mathcal{P}(X,T) = 1. \tag{3.90}$$

Using the variable transformation, Eq. (3.88), Eq. (3.73) is described as

$$\begin{aligned} \frac{\partial \mathcal{P}(X,T)}{\partial T} &= -X\frac{\partial \mathcal{P}(X,T)}{\partial X} \\ &\quad - \left(\gamma\left(\frac{X}{a}\right)^\gamma + 1\right)\mathcal{P}(X,T) + \gamma\int_X^\infty \frac{dZ}{Z} g\left(\frac{X}{Z}\right)\left(\frac{Z}{a}\right)^\gamma \mathcal{P}(Z,T), \end{aligned} \tag{3.91}$$

where $\mathcal{P}(X,T) = \dfrac{e^{-T}}{a}P\left(Xe^{-T}/a, e^{\gamma T}\right)$. In the long time limit, $\mathcal{P}(X,T)$ is expected to be a $T$ independent function $\mathcal{P}(X)$ because of the dynamical scaling law. By taking the left-hand side of Eq. (3.91) to be zero, the similarity solution satisfies the following equation:

$$X\frac{\partial \mathcal{P}(X)}{\partial X} = -\left(\gamma\left(\frac{X}{a}\right)^\gamma + 1\right)\mathcal{P}(X) + \gamma\int_X^\infty \frac{dZ}{Z} g\left(\frac{X}{Z}\right)\left(\frac{Z}{a}\right)^\gamma \mathcal{P}(Z). \tag{3.92}$$

Let us solve Eq. (3.92) in a specific case. We assume $g(r) = 1$ and then Eq. (3.92) is reduced to

$$X\frac{\partial \mathcal{P}(X)}{\partial X} = -\left(\gamma\left(\frac{X}{a}\right)^{\gamma} + 1\right)\mathcal{P}(X) + \gamma\int_X^{\infty}\frac{dZ}{Z}\left(\frac{Z}{a}\right)^{\gamma}\mathcal{P}(Z). \quad (3.93)$$

Differentiating Eq. (3.93) by $X$, a second order ordinary equation is obtained as

$$X\frac{\partial^2 \mathcal{P}(X)}{\partial X^2} + \left(\gamma\left(\frac{X}{a}\right)^{\gamma} + 2\right)\frac{\partial \mathcal{P}(X)}{\partial X} + \frac{\gamma(\gamma+1)}{a}\left(\frac{X}{a}\right)^{\gamma-1}\mathcal{P}(X) = 0, \quad (3.94)$$

and the general solution is given by

$$\mathcal{P}(X) = C_1 e^{-\left(\frac{X}{a}\right)^{\gamma}} + C_2 e^{-\left(\frac{X}{a}\right)^{\gamma}}\Gamma\left(-\frac{1}{\gamma}; -\left(\frac{X}{a}\right)^{\gamma}\right), \quad (3.95)$$

where $C_1$ and $C_2$ are integral constants. $\Gamma(b;z)$ is an incomplete gamma function: $\Gamma(b;z) = \int_z^{\infty} y^{b-1}e^{-y}dy$. From an obvious condition, $\mathcal{P}(X) \geq 0$, $C_2$ in Eq. (3.95) should be zero, then

$$\mathcal{P}(X) = C_1 e^{-\left(\frac{X}{a}\right)^{\gamma}}. \quad (3.96)$$

The constants $C_1$ and $a$ are determined by Eqs. (3.89) and (3.90) as

$$C_1 = \frac{\Gamma(1+2/\gamma)}{2\Gamma(1+1/\gamma)^2}, \quad (3.97)$$

and

$$a = \frac{2\Gamma(1+1/\gamma)}{\Gamma(1+2/\gamma)}, \quad (3.98)$$

where $\Gamma(b)$ is a gamma function: $\Gamma(b) = \int_0^{\infty} y^{b-1}e^{-y}dy$. As a consequence, $\mathcal{P}(X)$ is given by

$$\mathcal{P}(X) = \frac{\Gamma(1+2/\gamma)}{2\Gamma(1+1/\gamma)^2}\exp\left[-\left(\frac{\Gamma(1+2/\gamma)}{2\Gamma(1+1/\gamma)}X\right)^{\gamma}\right], \quad (3.99)$$

and average size $\langle x\rangle$ is given by

$$\langle x\rangle = \frac{\Gamma(1+2/\gamma)}{2\Gamma(1+1/\gamma)}\left(\frac{t}{\tau}\right)^{-1/\gamma}. \quad (3.100)$$

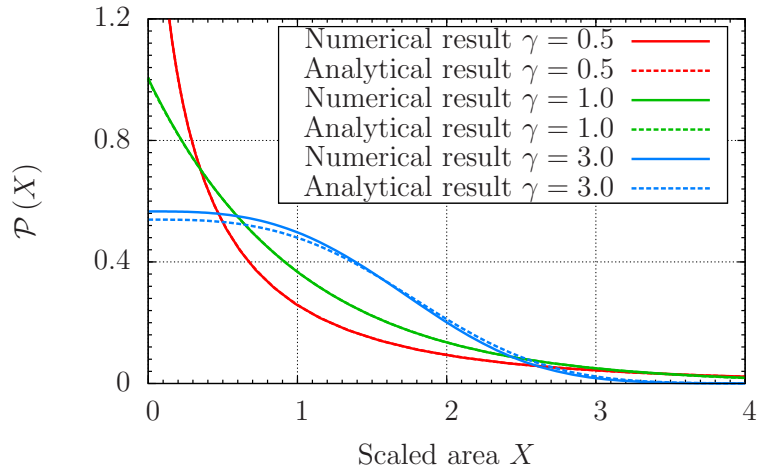


Figure 3.22: The comparison of analytical and numerical solutions of the scaled size distributions, $\mathcal{P}(X)$. The difference of color corresponds to the difference of $\gamma$. The solid lines correspond to $\mathcal{P}(X)$ solved numerically. The numerical solutions are same as that of $t/\tau = 10^3$ in Figs. 3.18b, 3.19b, and 3.20b, respectively. The dashed lines correspond to $\mathcal{P}(X)$ solved analytically. The analytical solutions are given by Eq. (3.99) in each $\gamma$.

Because Eq. (3.100) is an asymptotic behavior, the initial condition $\langle x \rangle (t = 0) = 1$ is not satisfied. We modify Eq. (3.100) to satisfy the initial condition by shifting the origin of the time. The result is

$$\langle x \rangle = \frac{\Gamma(1 + 2/\gamma)}{2\Gamma(1 + 1/\gamma)} \left[ \frac{t}{\tau} + \left( \frac{\Gamma(1 + 2/\gamma)}{2\Gamma(1 + 1/\gamma)} \right)^{\gamma} \right]^{-1/\gamma}. \tag{3.101}$$

Here we confirm the validity of Eqs. (3.99) and (3.101) by comparing with the numerical results in Figs. 3.22 and 3.23. Comparing the analytical solution with the numerical one, there is a slight difference between them; However, they accord with each other well.

## 3.4 Summary

The results of the stochastic modeling of time-dependent desiccation crack pattern is summarized here. In Sect. 3.1, we investigate the dynamics of a single fragment by the theoretical and numerical analysis. We have approximated the previous continuum model into the over-damped model to make it easy to calculate. Using a dimensional analysis, we have obtained a rough description of the lifetime. The functional form has the asymptotic behavior; When the characteristic length scale of fragment $L$ is much larger than the characteristic

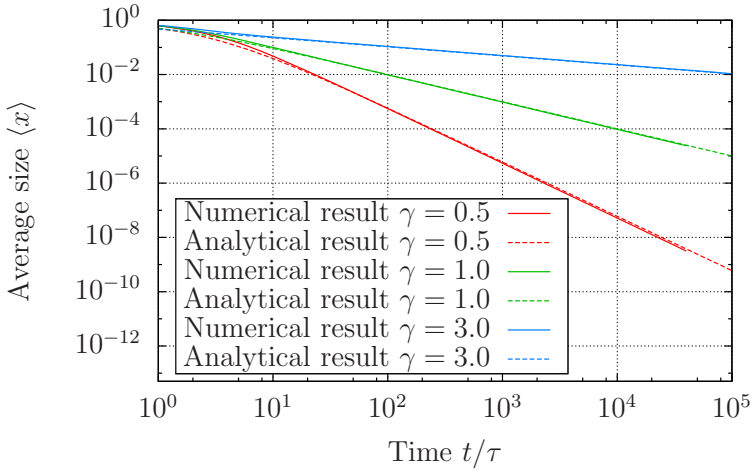


Figure 3.23: The comparison of analytical and numerical solutions of the average size, $\langle x \rangle$. The difference of color corresponds to the difference of $\gamma$. The solid lines correspond to $\langle x \rangle$ solved numerically. The numerical solutions are same as that of $\alpha = 1.0$ in Fig. 3.17. The dashed lines correspond to $\langle x \rangle$ solved analytically. The analytical solutions are given by Eq. (3.101) in each $\gamma$.

length scale $\lambda_D$, the lifetime becomes a constant value. Inversely, when $L$ is much smaller than $\lambda_D$, the lifetime depends on $L$. The validity has been confirmed by the investigation of the exact solution in the case that the fragment shape is given by a disk. Furthermore, we have carried out the calculation of Eqs. (3.19) and (3.20) by using the finite volume method, in order to investigate the lifetime of rectangular-shaped fragment with dimensions of $L_x \times L_y$. The results have shown the lifetime is characterized by $\lambda_D$ and the harmonic average of $L_x^2$ and $L_y^2$. This implies the lifetime is described by the area of fragment, the aspect ratio, and $\lambda_D$. This is consistent with the analysis the disk-shaped fragment.

In Sect. 3.2, we propose the modified Gibrat process by taking into account the lifetime of the fragment. The lifetime $T_b(S)$ depends on the size of fragment, $S$, and it is a decreasing function of $S$. As the functional form of the lifetime, we use a power function, $T_b(S) = \tau (S/\theta)^{-\gamma}$, characterized by the exponent $\gamma$, and a logarithmic function $T_b(S) = \tau [1 - \log (S/\theta)]$. The case of the power function with $\gamma = 0$ corresponds to the original Gibrat process. As the probability density function of the dividing ratio, $r$, we use the beta distribution $g(r) = r^{\alpha-1}(1-r)^{\alpha-1}/B(\alpha, \alpha)$, which is characterized by a single parameter $\alpha$. The time evolution of average size is investigated in each case of the lifetime. As a result, for the power function of lifetime, $T_b(S) = \tau (S/\theta)^{-\gamma}$, the average size is proportional to $t^{-1/\gamma}$ in large $t$. For the logarithmic life-

time, $T_b(S) = \tau[1 - \log(S/\theta)]$, it is proportional to $\exp\left(-C\sqrt{t}\right)$, where $C$ is a positive constant, in large $t$. The time evolution of average size is almost independent of $\alpha$. The behavior of time evolution of average size is investigated theoretically by an ordinary differential equation. The ordinary differential equation is derived by approximating all dividing ratios to 1/2. This is a daring approximation; However, the behavior that is obtained by solving the ordinary differential equation with an appropriate initial condition is quantitatively consistent with the numerical result. The time series of size distributions is investigated in each case of the lifetime. The size distributions take initially an obvious functional form depending on the functional form of $g(r)$. In the case of $T_b(S) = \tau(S/\theta)^{-\gamma}$, we find that the dynamical scaling law exists like the result of direct simulation of the continuum using the SPH. In the case of $T_b(S) = \tau[1 - \log(S/\theta)]$, we find that there is no dynamical scaling property in the time evolution of size distribution.

In Sect. 3.3, we have modeled the modified Gibrat process to be suitable for investigating it analytically by approximating to the Poisson process. The characteristic time of breaking events are represented by the lifetime depending on the fragment size $S$, $T_b(S)$, whereas the characteristic time is given by a constant in the original Poisson process. In the modeling, a master equation of the modified Gibrat process has been proposed and called the "markovianized modified Gibrat process". In the scaling analysis, we have confirmed the existence of the dynamical scaling property of the size distribution in the case that the functional form of lifetime is given by a power function. Furthermore, the analysis has predicted the scaling property is independent of the functional form of the probability density function of the dividing ratio, $g(r)$. The markovianized modified Gibrat process with a constant lifetime has been exactly solved and led to a lognormal distribution just like the original Gibrat process. However, the parameters characterizing the functional form is different form that of the original Gibrat process. We have investigated the time-dependent properties of the master equation numerically. The time-dependent behavior of the average size and the size distributions is consistent with the modified Gibrat process. The time evolutions of average size behave like the same functional forms in the modified Gibrat process. It has been also confirmed that the dynamical scaling law exists in the case that the functional form of the lifetime is given by a power function, whereas the dynamical scaling law does not exist in the case that the functional form of lifetime is given by a logarithmic function. The differences between the markovianized modified Gibrat process and the modified Gibrat process appear in the $\alpha$ dependency of the average size and the detail functional forms of size distributions; The $\alpha$ dependency in the same lifetime appears systematically, whereas it could not be observed in the modified Gibrat process. The positive correlation is observed between the

value of $\alpha$ and the value of average size at the same time in the same functional form of the lifetime. We have solved the master equation analytically in the specific case, $\tilde{T}_b(x) = x^{-\gamma}$ and $g(r) = 1$. The scaled size distribution and the average size have been derived analytically. They have been compered with the numerical results and consistent with each other.

# Chapter 4

# Experiment

In the previous works of the experiment of the desiccation crack pattern, the time-dependent statistical properties have not investigated so much. In the present work, we have investigated the time evolution of the size distributions theoretically and predicted the dynamical scaling property. In this chapter, we investigate the actual desiccation crack patterns in order to confirm the dynamical scaling property experimentally.

First, we explain the setup of the experiment of the desiccation crack pattern. Next, according to the interval photography of the crack pattern, we obtain the time series of the crack pattern. Finally, by the image processing, we investigate the time evolution of the average size of the fragments, the time series of the size distribution, and the dividing ratio of the fragments.

## 4.1 Experimental setup

The experiments of the desiccation crack patterns are carried out with the interval photography. We choose the paste composed of water and powder of magnesium carbonate hydroxide (Kanto Chemical, Tokyo, Japan). The density of the powder is 2.0 g/cm$^3$. We prepare a paste containing the powder of magnesium carbonate hydroxide with 6 % volume fraction. The paste is desiccated in the open acrylic container with dimensions of 400 mm $\times$ 400 mm. The initial thickness of the paste is 16.6 mm. The paste is kept in an air-conditioned room at 25 °C. The humidity is not controlled. The time evolution of the crack pattern is taken by the interval photography with the 2 minutes interval. The photos of the crack patterns are dealt with to be binarized pictures in order to analyze the fragments. For carrying out the binarization of the photos, we use ImageJ [97] which is the Java-based image processing program, in the public domain.

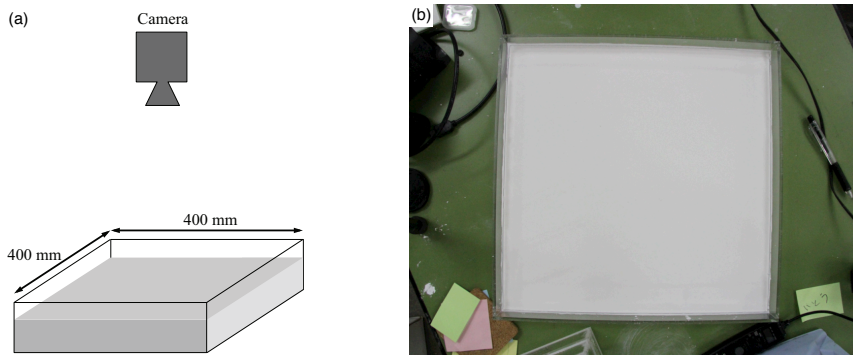


Figure 4.1: (a) Schematic figure of the experimental setup. The paste is desiccated in the open container with dimensions of 400 mm × 400 mm. The crack pattern is taken by the interval photography. (b) A snapshot we obtained. The time series of the snapshots is analyzed by the image processing.

## 4.2 Result

In this section, we show the results of the experiments. We first show the time evolution of the crack patterns, the average areal size of fragments, and the size distribution. Furthermore, we investigate the existence of the dynamical scaling law in the size distribution. In our theoretical work, the dividing ratio distribution has an important role to determine the functional form of the size distributions. In the previous work of the desiccation crack patterns, the dividing ratio distribution have never been investigated. Therefore, in order to confirm the consistency of the theoretical work, we investigate the dividing ratio distribution. Finally, we compare the experimental size distribution with the theoretical results.

### 4.2.1 Crack pattern

We show the time evolution of the crack patterns in Fig. 4.2. The patterns are binarized to black and white. Black regions correspond to fragments and white lines are cracks. In the following analysis, we use the fragments which are not attached to the container wall for avoiding that the influence of boundaries affects the results of analysis. We set the origin of time as when the number of fragments not attached to the container wall becomes greater than three. Figure 4.2 (a) shows the pattern when the initial crack runs on the bulk of the paste. (b) shows the the pattern at the origin of time. 4.3 hours passed between (a) and (b). (c) and (d) correspond to the patterns after 10 hours and 20 hours from (b), respectively. We find that the patterns change with time

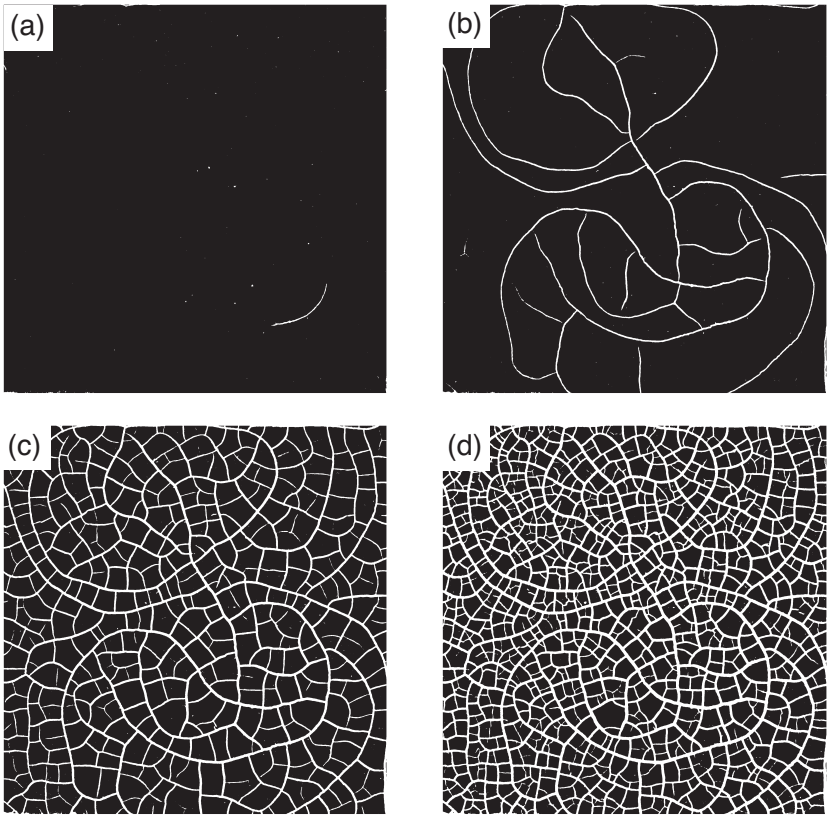


Figure 4.2: Binarized crack patterns we used for the analysis. (a) is the pattern at the time when the initial crack runs. (b) is the pattern at the time when the number of fragments which are not attached to the container boundary becomes greater than three. We set this time as the origin of time of the following analysis. The elapsed time between (a) and (b) is 4.3 hours. (c) is the pattern after 10 hours from (b). (d) is the pattern after 20 hours from (b).

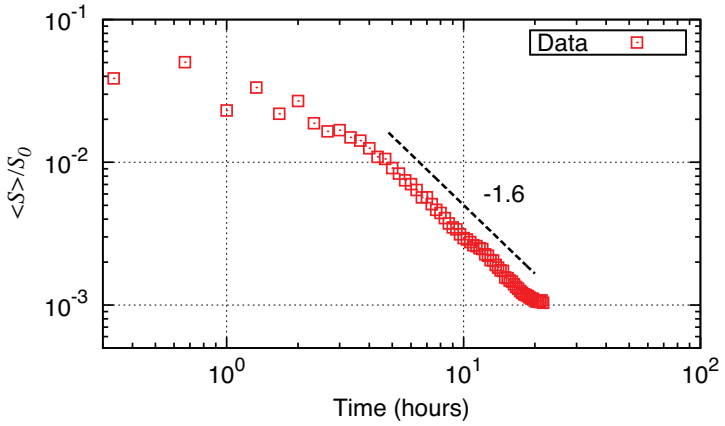


Figure 4.3: Time evolution of the average areal size. The horizontal axis indicates the elapsed time measured from the origin of time defined in Sect. 4.2.1. The vertical axis indicates the average areal size normalized by the initial size $S_0 = 400 \times 400$ mm$^2$. The square points indicates the raw data. The dotted line corresponds to the power function with the exponent $-1.6$.

and the characteristic areal size becomes small with time. We have confirmed that the time evolution of the pattern stops at 23.3 hours from the origin of time.

### 4.2.2 Average size

The fragment areal sizes are measured by counting the black pixels in the binarized images. In Fig. 4.3, we analyze the time evolution of the average areal size of the fragments, $\langle S \rangle$, which is made by averaging the sizes of the fragments not attached to the container boundary. The horizontal axis indicates the origin of time, which corresponds to Fig. 4.2 (b). The unit is an hour. The vertical axis indicates the average areal size normalized by the initial size $S_0 = 400 \times 400$ mm$^2$. We find that the average areal size decays with time. We find that the average size $\langle S \rangle$ obeys the power law as

$$\langle S \rangle \propto t^d, \tag{4.1}$$

where $t$ is the elapsed time and $d$ is a fitting parameter, except for the initial relaxation stage (i.e., less than 3 hours) and the stage in which the desiccation declines (i.e., greater than 20 hours). According to the result of the fitting, the value of $d$ is about $-1.6$.

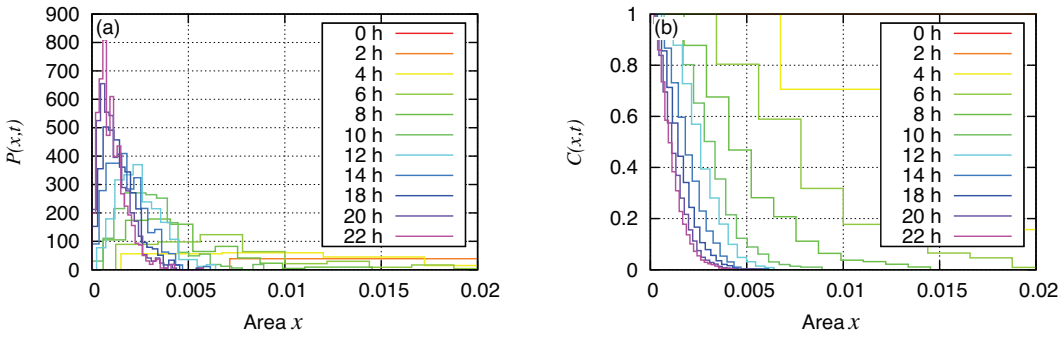


Figure 4.4: Time evolution of the areal size distribution of the fragments on the experiment of the desiccation crack pattern. The horizontal axis indicates the areal size $S$ normalized by the initial size $S_0 = 400 \times 400$ mm$^2$, $x = S/S_0$. The difference of colors corresponds to the difference of elapsed times. (a) shows the probability density function. (b) shows the cumulative distribution function.

### 4.2.3 Size distribution

We show the time evolution of the size distribution in Figs. 4.4 and 4.5. Figure 4.4 shows the time evolution of the raw size distribution. The horizontal axis indicates the size normalized by the initial size. The difference of colors corresponds to the difference of the elapsed times. (a) shows the probability density function $P(x,t)$ where $x = S/S_0$ and $t$ is the elapsed time. (b) shows the cumulative distribution function defined as

$$C(x,t) = \int_x^\infty dy P(y,t)\,. \tag{4.2}$$

We find that the distribution varies with time and shifts to the smaller areal side. Figure 4.5 shows the time evolution of the size distribution scaled by the average areal size. The horizontal axis indicates the scaled size $X = S/\langle S \rangle$. (a) shows the probability density function of $X$. (b) shows the cumulative distribution function. We find that the scaled size distribution seems to collapse into a single master curve except for the early stage (i.e., less than 2 hours).

### 4.2.4 Dividing ratio distribution

In this section, we investigate the dividing ratio distribution of the experimental crack patterns. When we count the breaking events of the fragments experimentally by the interval photography, the events in which the fragment breaks into more than two pieces may appear. This is not suitable to calculate the dividing ratios. Therefore we choose only the events in which the fragment

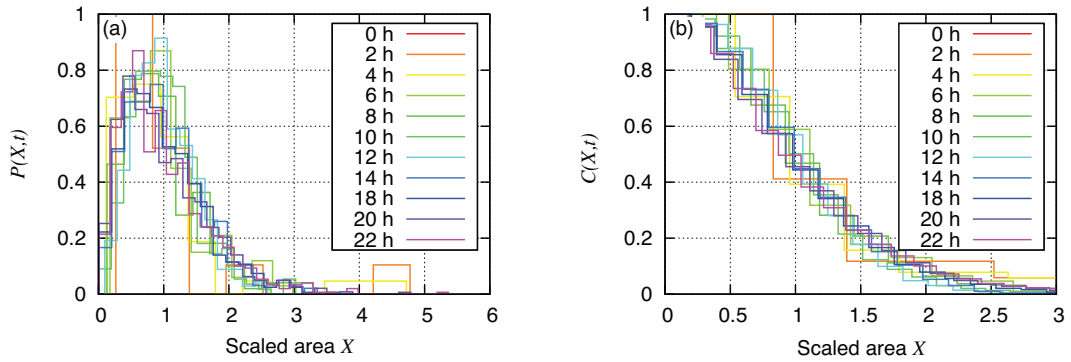


Figure 4.5: Scaled time evolution of the areal size distribution of fragments by the average size $\langle S \rangle$ on the experiment of desiccation crack pattern. The horizontal axis indicates the scaled size $X = S/\langle S \rangle$. Other conditions are the same as ones of Fig. 4.4.

breaks into two pieces and do not count other events. Furthermore, we count the breaking events in the whole experimental elapsed time. The dividing ratio may depend on time generally. However, as we know from the time evolution of the size distribution, the time evolution of the scaled size distribution can be collapsed except for the early stage. This may imply that the fragments follow to the same dynamical property except for the early stage. Moreover, the number of breaking events in the early stage is quite few and does not contributes to the dividing ratio distribution. We show the result in Fig. 4.6. It is exactly symmetry with respect to $r = 1/2$, because we choose only the events in which the fragment breaks into two pieces. We fit the data with the beta distribution

$$g(r) = \frac{1}{B(\alpha, \alpha)} r^{\alpha-1} (1-r)^{\alpha-1}, \tag{4.3}$$

where $B(\alpha, \alpha)$ is a beta function: $B(\alpha, \alpha) = \int_0^1 dr\, r^{\alpha-1} (1-r)^{\alpha-1}$. As a result, the value of $\alpha$ is about 2.3.

### 4.2.5 Shape of size distribution

In this section, we analyze the shape of the scaled areal size distribution on the final state (i.e., 23.3 hours). According to the theoretical result of the functional form of the size distribution, Eq. (3.86), we assume a fitting function given by

$$P(X) = \frac{b c^{a/b}}{\Gamma(a/b)} X^{a-1} \exp\left(-cX^b\right), \tag{4.4}$$

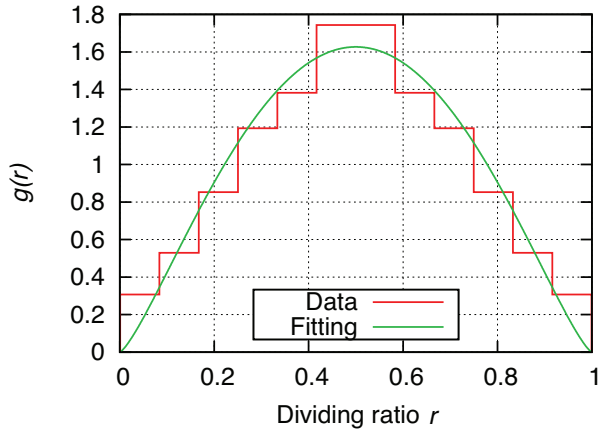


Figure 4.6: Dividing ratio distribution on the experimental desiccation crack pattern. The dividing ratios are obtained from the events in which the fragment breaks into exactly two pieces. The distribution is made from them in the whole experimental elapsed time. The red line indicates the dividing ratio distribution. The green line is obtained by fitting the data with Eq. (4.3).

where $a$, $b$, and $c$ are fitting parameters. $\Gamma(k)$ is a gamma function: $\Gamma(k) = \int_0^\infty y^{k-1}e^{-y}dy$. The cumulative distribution function of $X$, $C(X)$, is described as

$$C(X) = \int_X^\infty dx'\ P(x') = \frac{1}{\Gamma\left(a/b\right)}\Gamma\left(\frac{a}{b}; cX^b\right), \tag{4.5}$$

where $\Gamma(k;z)$ is an incomplete gamma function: $\Gamma(k;z) = \int_z^\infty y^{k-1}e^{-y}dy$. The final state of the cumulative scaled size distribution function is fitted by Eq. (4.5) as shown in Fig. 4.7. As a result, $a$, $b$, and $c$ are nearly 5.5, 0.77, and 4.1, respectively. The theoretical result of the relationship between $b$ and the exponent of the average size $d$ is given by $b \times d = -1$. The values of $b$ and $d$ are consistent with the relationship. The theoretical value of $a$ corresponds to the exponent of the beta distribution $\alpha$. The value of $a$ is not consistent with the value of $\alpha$ obtained by fitting the experimental data of the dividing ratio distribution.

## 4.3 Summary

The experimental results are summarized in this section. We have carried out the experiment of the desiccation crack patterns of the paste composed of water and powder of the magnesium carbonate hydroxide. By using the image

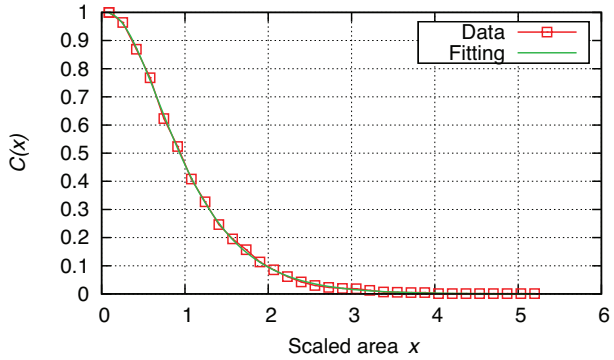


Figure 4.7: Fitting of the cumulative distribution function at the final state. The red square points indicate the cumulative scaled size distribution function of the crack pattern after 23.3 hours at the origin of time. The green solid line is obtained by fitting the data with Eq. (4.5).

analysis, we have investigated the time evolution of the average areal size of the fragments, the time series of the size distribution, and the dividing ratio distribution. First, we have investigated the time evolution of the average areal size of the fragments. We have found that the average size decays with time and obeys the power-law function of time except for the early stage and later stage. According to the fitting the data, the exponent $d$ is nearly $-1.6$. Next, we have investigated the time evolution of the areal fragment size distribution. We have observed that the size distribution varies with time and shifts to the smaller areal side. Furthermore, we have found that the time series of the scaled size distribution collapses into a master curve except for the early stage just like our theoretical results. In addition, we have investigated the dividing ratio distribution of the fragments, $g(r)$. The dividing ratios have been obtained from the events in which the fragment breaks into exactly two pieces. The distribution has been made from them in the whole experimental elapsed time. The dividing ratio distribution forms a bell-shape and becomes maximal at $r = 1/2$. The dividing ratio distribution has been fitted with a beta distribution; $g(r) = r^{\alpha-1}(1-r)^{\alpha-1}/B(\alpha,\alpha)$. As a result, the value of $\alpha$ is about 2.3. The cumulative distribution function of the scaled size at the final state has been fitted with a theoretical function obtained in Chapter 3; $C(x) = \Gamma\left(a/b; cx^b\right)/\Gamma\left(a/b\right)$. According to the theoretical results in Chapter 3, the value of $a$ corresponds to the exponent of the beta distribution $\alpha$, and the relationship between the value of $b$ and the exponent of the average size $d$ is given by $b \times d = -1$. The relationship between the values of $b$ and $d$ is consistent with the theoretical result; However, the value of $a$ does not accord with the value of $\alpha$ obtained by fitting the experimental data of the

dividing ratio distribution. We currently guess that the inconsistency of the relationship between $a$ and $\alpha$ results from the simplification of the functional form of the lifetime in the theoretical analysis. In Chapter 3, we have used the lifetime depending on the fragment size only for the simplification. In the actual fragmentation, the lifetime depends on not only the size but also the aspect ratio of the fragment as shown in Eq. (3.29). The aspect ratio dependency may contribute to the functional form of the size distribution.

# Chapter 5

# Conclusion

## 5.1 Summary of this study

### 5.1.1 Continuum model

In Chap. 2, we have proposed a three dimensional continuum model on the basis of the Kelvin-Voigt model in order to investigate the statistical properties of the desiccation crack pattern of the thin layer of paste. The constitutive equation of the model has been defined as the modified Kelvin-Voigt model where the desiccation stress is introduced as the effect of the contraction owing to the evaporation of the inner water. In the model, the desiccation stress is defined as the linear function of time. The three dimensional model has been reduced to the quasi two dimensional model under the approximation that the vertical motion is vanished. Using the smoothed particle hydrodynamics formulation, we have simulated the dynamics of the quasi two dimensional continuum model and obtained the realistic crack pattern (see Fig. 5.1).

Furthermore, we have investigated the statistical properties such as the average areal size of the fragments and the areal fragment size distribution. As a result, the average size decays in inverse proportion to time. The time series of the size distribution scaled with the average size is collapsed into a time independent curve except for the early stage of the fragmentation. We have called this phenomenon the "dynamical scaling law" of the size distribution of the desiccation crack pattern (see Fig. 5.2).

The qualitative behavior of the time evolution of the average size has expressed by the dimensional analysis of the over-damped model of the present continuum model; The duration of the initial relaxation of the average size, which is obtained by the dimensional analysis, is consistent with the result of the SPH simulations. In addition, it has been explained that the duration of the initial relaxation corresponds to the duration that size distribution can not

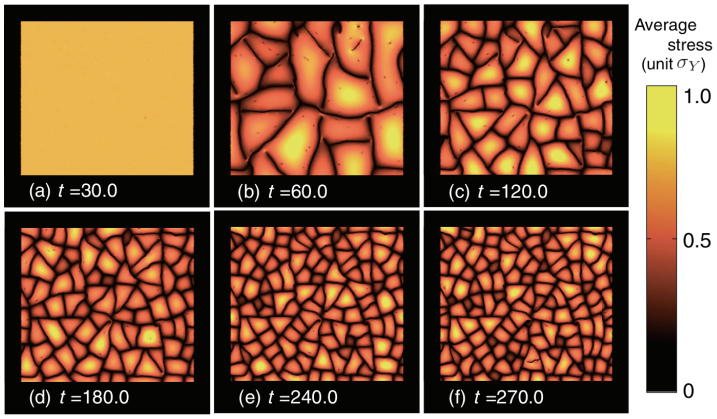


Figure 5.1: The Typical time evolution of the crack patterns obtained by the SPH simulation. The color indicates the magnitude of the averaged stress normalized by the yield stress. The time passes in the alphabetical order. This figure same as Fig. 2.2.

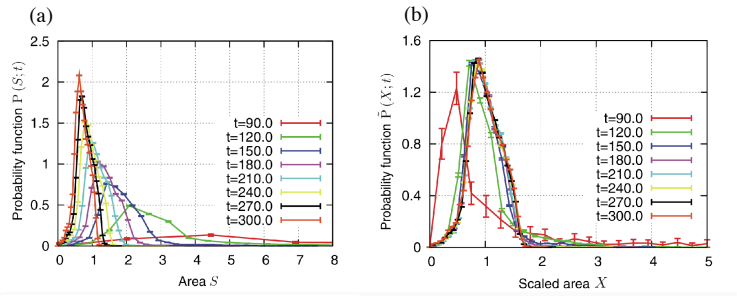


Figure 5.2: The fragment areal size distribution obtained by the SPH simulations. This figure is same as Fig. 2.4. The difference of colors indicates the difference of time. (a) shows the time evolution of the size distribution. (b) shows the time evolution of the scaled size distribution by average size. As time passes, the scaled size distribution collapses to a time-invariant curve. We call this property the "dynamical scaling law".

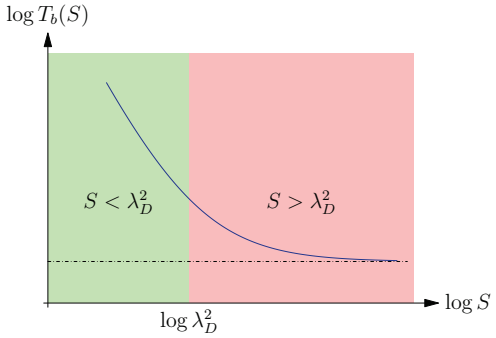


Figure 5.3: Schematic figure of the lifetime $T_b$ as a function of fragment size $S$. The green and red parts indicate the regions of $S < \lambda_D^2$ and $S > \lambda_D^2$, respectively. For $S \gg \lambda_D^2$, the lifetime becomes a constant value depending on the material constants. For $S \ll \lambda_D^2$, the lifetime behaves divergently with smaller $S$. If we choose the power function as the desiccation stress, the lifetime obeys the power law at the smaller $S$.

be scaled.

### 5.1.2 Stochastic model

In Chap. 3, we have investigated the statistical properties of the desiccation crack pattern in terms of the stochastic theory. First we have investigated the dynamics of a single isolated fragment in order to obtain the useful information for developing the stochastic model of the desiccation crack pattern. The previous continuum model has been approximated to the over-damped one and investigated by the theoretical and numerical analysis. As a result, we have found that the interval between the time when the desiccation starts and the time when the fragment is fractured depends on the size of the fragment. We have called this interval the "lifetime". When the size is greater than the square of a certain characteristic length scale, $\lambda_D$, the lifetime of the fragment is constant. Inversely, when the size is smaller than $\lambda_D^2$, the lifetime of the fragment depends on the size (see Fig. 5.3). Moreover, we have found that the lifetime depends on not only the size but also the aspect ratio of the fragment. It may depend on other quantities characterizing the fragment shape; However, we have not yet investigated the dependency. We have derived the functional form of the lifetime by using the inverse function of the desiccation stress. For instance, if the desiccation stress is given by the power (exponential) function, the lifetime is given by the power (logarithmic) function, respectively. The lifetime is described as the decreasing function of size; Therefore, the individual lifetime is increasing as evolving the fragmentation.

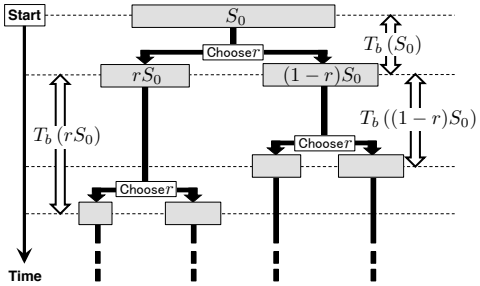


Figure 5.4: Schematic flow diagram of the modified Gibrat process. Initially there is a fragment whose size is $S_0$. The lifetime of the fragment is given by $T_b(S_0)$. When $T_b(S_0)$ has passed, the fragment breaks into two pieces with a random dividing ratio $r$. $r$ is chosen from the probability density function of fragment dividing ratio, $g(r)$. As a result, two fragments whose sizes are $rS_0$ and $(1-r)S_0$ are created. The procedure is iterated for the new fragments with size $rS_0$ whose lifetime is given by $T_b(rS_0)$, and size $(1-r)S_0$ whose lifetime is given by $T_b((1-r)S_0)$. This figure is same as Fig. 3.10.

Next, using the size-dependent lifetime, we have proposed a stochastic model on the basis of the Gibrat process. We have called the process the "modified Gibrat process". Fragments have the individual lifetime in the modified Gibrat process, whereas they have a common constant lifetime in the original Gibrat process (see Fig. 5.4). The modified Gibrat process exhibits the existence of the dynamical scaling law of the size distribution when the lifetime is given by a power function of size. The average size decays in the pawer law with the exponent which is the negative reciprocal of the exponent of the lifetime. The behavior of the average size have been expressed by the analytical calculation with the approximation that the fragments always break in half.

When we use a constant lifetime, the modified Gibrat process is completely equivalent to the original Gibrat process. Namely, if we use the lifetime characterized by $\lambda_D$, which is described as Eq. (3.30), in the modified Gibrat process, the property of the stochastic process changes gradually with the fragmentation; When the fragment size is greater than $\lambda_D^2$, the average size decays exponentially and the size distribution becomes the lognormal distribution. As the fragmentation progresses and the fragment size becomes smaller than $\lambda_D^2$, the decay of the average size changes from the exponential law to the power law, and the size distribution changes from the lognormal distribution to the distribution which has the dynamical scaling property. In the SPH simulations, we have observed that there is no dynamical scaling property in the early stage of the fragmentation. We consider that this is because the fragmentation in

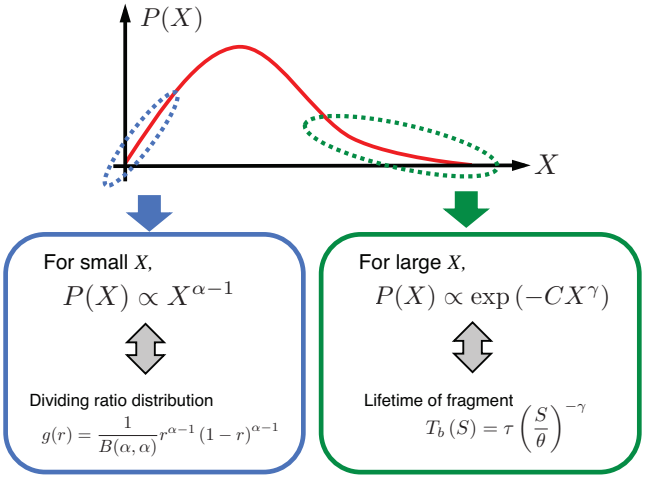


Figure 5.5: Schematic figure of the relationship among the asymptotic behavior of the scaled size distribution $P(X)$, the dividing ratio distribution, and the lifetime of fragment (Eq. (3.86)). For smaller scaled size $X$, $P(X) \propto X^{\alpha-1}$. The exponent $\alpha$ corresponds to the parameter of the dividing ratio distribution $g(r) = r^{\alpha-1}(1-r)^{\alpha-1}/B(\alpha,\alpha)$. For larger $X$, $P(X) \propto \exp(-CX^{\gamma})$. $C$ is a positive constant. The exponent $\gamma$ corresponds to the parameter of the lifetime $T_b(S) = \tau (S/\theta)^{-\gamma}$.

the early stage obeys the original Gibrat process.

Finally, we have proposed a master equation of the fragmentation process of the desiccation crack pattern on the basis of the modified Gibrat process. The master equation has been formulated as the Poisson process where the characteristic time scale is replaced with the lifetime of the fragment. The master equation enables us to investigate the dynamical scaling property analytically. By the scaling analysis of the master equation, it is found that the condition of the functional form of the lifetime for realizing the dynamical scaling law is that the lifetime is a power function. Actually, by the numerical analysis of the master equation, we have confirmed the condition. According to the numerical results, it is found that the average size decays in the power law with the exponent $-1/\gamma$ where $\gamma$ is the exponent of the power function of the lifetime. The numerical analysis has predicted that the functional form of the scaled size distribution $P(X)$ has the asymptotic behaviors; For smaller scaled size $X$, $P(X) \propto X^{a-1}$, and for the tail, $P(X) \propto \exp\left(-CX^{b}\right)$, where $a$, $b$, and $C$ are constant. Furthermore, by the fitting analysis of the numerical data, we have found two relations: $a = \alpha$, where $\alpha$ is a parameter of the dividing ratio distribution, $g(r)$, described as $g(r) = r^{\alpha-1}(1-r)^{\alpha-1}/B(\alpha,\alpha)$, and $b = \gamma$ (see Fig. 5.5).

### 5.1.3 Experiment

In Chap. 4, we have carried out the experiment of the desiccation crack pattern of the paste composed of water and powder of magnesium carbonate hydroxide for investigating the statistical properties. The time series of the crack pattern have been taken by the interval photography. Analyzing the time series of the images, we have obtained the time evolution of the average size of the fragments, the time series of the size distribution, and the dividing ratio distribution.

We have observed that the average size obeys the power law of time, that is, $\langle S \rangle \sim t^d$ except for the early stage of the fragmentation and the later stage of the desiccation. By the fitting analysis, $d$ is nearly $-1.6$. In the later stage of the desiccation, the time evolution of the average size stops. This phenomenon results from the stop of the fragmentation process. Our theoretical model can not reproduce the stop of the fragmentation. Our theory is based on the model of the two dimensional viscoelastic continuum attached to the bottom. The two dimensional model can not describe the stop of the fragmentation because the stress concentration always occur as far as we use the increasing function of the desiccation stress. We currently have no concrete idea for realizing the stop of the fragmentation process. The lifetime of the three dimensional fragment, or the slipping effect such as discussed in Ref. [65] may enable us to realize the stop of the fragmentation process.

We have observed that the size distribution obeys the dynamical scaling law except for the early stage (see Fig. 5.6). The absence of the dynamical scaling property in the early stage is consistent with the existence of non-power-law decay of the average size in the early stage. According to our theoretical results, it is expected that the Gibrat process is realized in the early stage; However, it is difficult to investigate whether the Gibrat process is realized. That is because the characteristic length scale which determines the cross-over from the Gibrat process to the modified Gibrat process with the size-dependent lifetime, $\lambda_D$, is difficult to measure. In our theory, $\lambda_D$ is determined by the thickness of the paste and the Poisson's ratio. The thickness of the paste is easy to measure; However, the Poisson's ratio is difficult to measure. Inversely, our theoretical result may use for the measurement of the Poisson's ratio. If we confirm the cross-over from the Gibrat process to the modified Gibrat process in the actual desiccation crack pattern, we can estimate $\lambda_D$. From $\lambda_D$, we can estimate the Poisson's ratio.

We have observed the dividing ratio $r$ and its distribution. The functional form of the distribution becomes a bell shape and has the maximum at $r = 0.5$. The functional form has been fitted with the beta distribution, $g(r) = r^{\alpha-1}(1-r)^{\alpha-1}/B(\alpha, \alpha)$. We have evaluated $\alpha$ is nearly 2.3.

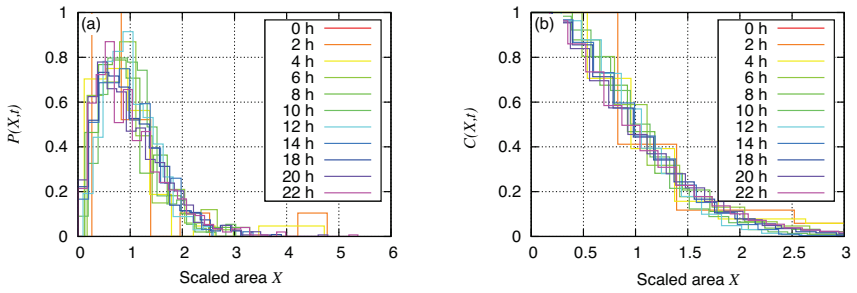


Figure 5.6: Time evolution of the scaled size distribution of fragments on the experiment of desiccation crack pattern. The color indicates the elapsed time. The horizontal axis indicates the size scaled by the average size, $X = S/\langle S \rangle$. (a) shows the probability density function. (b) shows the cumulative distribution function. We can observe that the size distribution obeys the dynamical scaling law except for the early stage. This figure is same as Fig. 4.5.

We have investigated the shape of the cumulative scaled size distribution $C(X)$. According to our theoretical results, we have assumed $C(X) = \Gamma\left(a/b; cX^b\right)/\Gamma\left(a/b\right)$. By the fitting analysis, $a$, $b$, and $c$ are nearly 5.5, 0.77, and 4.1, respectively. The relationship between $b$ and $d$ is consistent with the relationship our theory predicts; However the relationship between $a$ and $\alpha$ is not consistent with the theory. We currently guess that the inconsistency is due to what we have not taken into account the effect of the aspect ratio of the fragments to the lifetime. In the actual fragmentation, the lifetime depends on not only the size but also the aspect ratio of the fragment as shown in Eq. (3.29). The aspect ratio dependency may contribute to the functional form of the size distribution. If we formulate the lifetime using not only the aspect ratio but also other quantities characterizing the shape of the fragment, it may be possible to describe the detail of the functional form of the size distribution. When we formulate the stochastic process using the lifetime depending on the size and the aspect ratio, we must take into account not only the subdivision of the size but also the direction of the cracking, because the direction determines the aspect ratios of the fragments after the subdivision. Moreover, taking into account the other quantities characterizing the shape of the fragment, the elementary process may be more complicated. They may make us difficult to formulate the stochastic process; However, it is important for understanding the details of the shape of distribution.

## 5.2 Discussion

### 5.2.1 Characterization of crack structure

The crack structure has an important role for the material transport properties. The structure of the desiccation crack pattern in a paddy field is related with the diffusion of the water necessary to the growth of the young rice plant. The structure of the micro crack in the rock is related with the material transport in the rock.

In the fields of the geology, the characterization of the rock texture using the fractal geometrical analysis has been carried out. In the rock microstructure, the micro crack exists, and it has an important role for understanding the transport properties of the rock [98].

In the desiccation crack pattern, the fractal dimension has been also investigated in Ref. [15]. Colina and Roux have been analyzed the fractal dimension of the largest crack cluster in the binarized image of the clay crack patten by means of the density correlation method. They computed the density correlation function, $C(r)$, which was calculated by counting the number of pairs at a distance $r$ from each other which both belonged to the cluster. $C(r)$ obeys the power law if the pattern is a fractal, and the exponent of the power law characterizes the fractal dimension. They have observed the characteristic scale of length $r^*$ at which the fractal dimension changes quantitatively. Below $r^*$, the fractal dimension is nearly 1, which shows that the cracks are one-dimensional. On the other hand, above $r^*$, the fractal dimension is less than 2, and it is nearly 1.7. This result implies that the pattern is self-similar above $r^*$. They have interpreted $r^*$ as the length scale which the stresses are screened, so that the existence of a crack prevents the creation of a new crack. Furthermore, they have investigated the paste-thickness dependency of $r^*$, and they have reported that $r^*$ is proportional to the thickness.

In our desiccation crack pattern obtained by SPH calculation, by analysis using the box-counting method, the fractal dimension is nearly 1.1 [99]. This means that the cracks are nearly one-dimensional. Colina and Roux's result makes us expected that the fractal dimension of the SPH desiccation crack pattern may be nearly 1.7 in the simulation using the smaller thickness than the present one; However, we have not been confirmed it yet. If we were to observe it, the self-similarity could be explained by our model.

### 5.2.2 Crack generation

In the studies of fracture using the continuum, including our study, the crack generation is artificial. The crack generation is out of the continuum theory;

Therefore, it is often modeled by the two ways: First one is regarding the point where the characteristic stress exceeds a certain yield stress as the crack. This way is used in many studies of fracture using the continuum, including our study, and it is easy to model the generation and growth of crack; However, the physical meaning is unclear. The characteristic size scale of the crack seed is restricted to the size of the element in the calculation scheme, which corresponds to, for instance, the effective length in SPH. In this way, the generation of the crack seed and the crack growth are dealt with in the same way. The validity dealing them with in the same way is unclear. Second way is assuming that the crack seeds exist at the beginning in the material and the crack seeds which satisfy a certain condition, such as Griffith criterion [100], grow to the macroscopic cracks. The Griffith criterion is based on the elastic theory, and it is that the crack seeds grow to the macroscopic cracks, which satisfy that the loss of the elastic energy, owing to expanding of the crack, is greater than the gain of the surface energy, owing to the growth of crack (see Fig. 5.7). The physical meaning of this way is very clear; However, it is difficult to model due to some reasons. One of the reasons is how to model the distribution of crack seeds at the beginning. It is expected that the spatial distribution of crack seeds corresponds to the characteristic pore size of water domain in the paste; However, it is unclear. Even if the distribution is understood by the experimental measurement or the calculation of the molecular dynamics, how to introduce the distribution into the continuum theory is unclear. Recently, a study which may enable us to introduce the crack seeds into the continuum theory have been reported. Kitsunezaki [101] have been investigated the condition of the crack generation in the desiccated paste by using the elastic theory. The author have been introduced the spatial order parameter describing whether the point is wet or dry, and the author have been formulated the Griffith-like criterion including the order parameter. If we regard the point in the state of dry as the crack seed, we can naturally introduce the generation of the crack seed into the continuum theory. The Griffith-like criterion obtained by Kitsunezaki cannot be applied to our model directly; However, we may formulate the Griffith-like criterion suited to our model by the same way of formulation with Kitsunezaki's one.

### 5.2.3 Choice of material parameters

In our continuum model, there are many material parameters of the paste. However, most of them have never been measured exactly. That is because it is difficult to measure the material parameters of the paste in the critical cracking state which is defined as the state in which the initial crack begin to be created in the bulk (i.e., region of the top surface of the paste). In our model,

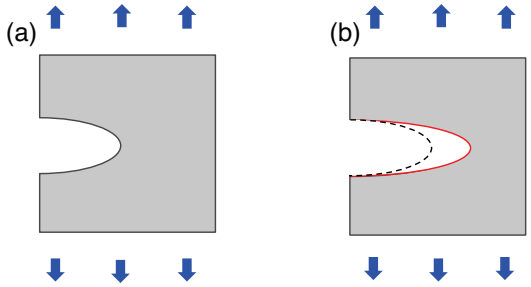


Figure 5.7: The illustration of the crack growth in the Griffith theory. The gray region describes the domain in a large two dimensional elastic body, including a crack tip. The elastic body suffers stresses which are described by blue arrows at the infinitely remote boundary. (a) shows the domain including a certain crack tip. (b) shows the same domain but the crack tip is grown a little, which is indicates the red line. The dotted line indicates the same crack tip with one in (a). If the crack is grown from the dotted one to the red one, the elastic energy is released due to the expanding of the crack, whereas the surface energy increases due to the increasing of the surface. If the loss of the elastic energy is greater than the gain of the surface energy, the crack grows. Inversely, if the loss of the elastic energy is smaller than the gain of the surface energy, the crack does not grow.

the most important parameters which characterize the rheological properties of the paste are the elastic constants and the viscosity. We have estimate the order of the elastic constants preliminarily by a compression test of the paste in the critical cracking state, and they has been used in the present simulation. However, the validity of the value of the viscosity we used is unclear. There are some studies investigating the viscosities of clay and soil [102, 103]; However, they depend on the kind of materials and the other quantities such as the temperature and the shear rate, and they take values in the wide range of the order ($10^2$ Pa$\cdot$s $\sim$ $10^6$ Pa$\cdot$s). The viscosity of the paste composed of water and powder in the critical cracking state is expected to be in the range; Therefore, we have chosen the value of the viscosity in the range.

In actual desiccating material, it is better to consider that the material parameters are time-dependent and spatially-dependent values rather than constant ones. The simulations of model which has constant material parameters may not be able to obtain the entire of the time evolution of the crack patterns. Actually, in the case that the thickness of the paste is greater than the size of linear dimension of the surface, the water content distribution along the depth direction becomes the nonlinear form, and thus the material parameters such as the elastic constants and the viscosity should be the depth-dependent value. There is a numerical study investigating the depth-dependent property of the

three-dimensional desiccation crack [68]; However, there are more parameters than that of our model.

To know all material parameters may be not realistic; Therefore, it may be necessary to try to new approaches. One of them is use of the data assimilation [104]. In the simulation of the desiccation crack pattern using the data assimilation, the material parameters are unknown variables rather than constants. Before the starting of the simulation, we prepare the experimental data of the time series of the pattern or the quantities possible to measure such as the weight of the paste, the thickness of the paste, and so on. The data assimilation method is to statistically estimate the spatial distribution of the unknown variables by searching the distribution which can reproduce the data most. The advantage of this method is that we can estimate the material parameters which are unknown, spatially distributed, and time-dependent by using the simple model of the paste desiccated. However, the disadvantage of the method is that a number of the simulations must be carried out in parallel in order to estimate the material parameters statistically. In order to overcome the disadvantage, we must choose the solver which enables us to calculate our model faster.

### 5.2.4 Material dependency

We have carried out the experiment of the desiccation crack pattern of the paste composed of water and powder of magnesium carbonate hydroxide. As the previous experiment, we also had carried out the experiment of the desiccation crack pattern of the paste composed of water and powder of calcium carbonate in the same condition of the experiment using the magnesium carbonate hydroxide. However, we could not conclude the existence of the dynamical scaling property in this case. That is because the size distribution is unclear due to the lack of the number of the fragments. In the experiment using calcium carbonate, the crack width is very narrow, and the subdivision process stops in a few stages. This causes the lack of the number of the fragments. In the experiment using magnesium carbonate hydroxide, as shown in Fig. 4.2, we can observe that the $4 \sim 6$ times of subdivisions seem to occur up to the end of time evolution. The number of the subdivisions can be estimated by the decrease of the average size of fragments. Let us assume that the number of fragments $N$ is given by $S_0/\langle S \rangle$. Let $N_{\mathrm{Fin}}$ and $N_0$ denote the numbers of fragments at the final stage and the origin of time, respectively. As shown in Fig. 4.3, the average size $\langle S \rangle / S_0$ at the final stage becomes about 2 % at the origin of time; Therefore, the ratio $N_0/N_{\mathrm{Fin}} \sim 0.02$. Assuming that the dividing ratios are always 1/2, the number of subdivisions which occur from the origin of time to the final stage can be estimated by $\log_2 N_{\mathrm{Fin}}/N_0 \sim 5.6$.

The number of the subdivisions of the paste composed of water and powder of magnesium carbonate hydroxide is greater than that of the paste composed of water and powder of calcium carbonate. We currently consider that the difference in the number of the subdivisions results from the difference of the electric property [105]. The particles of the power of magnesium carbonate hydroxide in water is not charged; Therefore, the particles precipitate. When the particles fall and lie thick on the bottom, it is expected that the network structure of particles is formed. The network structure can hold a lot of water. Once the network structure is formed, the structure is durable up to the beginning of the critical cracking state which is defined above. Then, when the material is desiccated, it shrinks well. As a result, many subdivisions occur, and the crack width can be wider. On the other hand, the particles of the power of calcium carbonate in water is charged; Therefore, there is the Coulomb force between the pair of the particles. When the particles fall and lie thick on the bottom, the Coulomb force prevents particles from forming the network structure. The final structure can not hold a lot of water, and the water content becomes small. Then, when the material is desiccated, it cannot shrink well. As a result, the subdivision process stops in a few stages, and the crack width becomes narrow.

In our study, if the material can shrink and break endlessly, the dynamical scaling property can be observed always. However, the real material cannot shrink and break endlessly; Therefore, in the case of some materials which does not shrink well, it is difficult to observe the dynamical scaling property. In order to observe the dynamical scaling property using the material which does not shrink well, it is necessary to prepare samples which are experimented at the same time and obtain the averaged size distribution. Currently, we have not yet carried out the experiment in which many samples of pastes are desiccated at the same time. We expect that the paste composed of water and powder of calcium carbonate can show us the dynamical scaling property if we carry out the experiments at the same time.

### 5.2.5 Application and generalization of our work

Our result can be applied to guess the history of the fragmentation process of the desiccation crack pattern. In the case that it is difficult to measure the dynamics, if we assume that the size distribution results from the fragmentation process in which the dynamical scaling law is obeyed, we can guess the desiccation stress from the functional form of the size distribution. The functional form of the tail of the size distribution corresponds to the functional form of the lifetime. Then we can know the desiccation stress from the functional form of the lifetime.

We have modeled the desiccation crack pattern by using the viscoelastic continuum including the contraction effect. This model can be applied to other phenomena because our model is very simple. In the following, we discuss the applicability of our study to other phenomena.

### Fragmentation owing to thermal contraction

Some material show the fragmentation patterns owing to the thermal contraction [61,106]. Our model can be directly applied to such kind of fragmentations by reinterpreting the desiccation stress as the stress owing to the thermal contraction. Especially, the viscoelastic layer fragmenting owing to the thermal contraction is equivalent to our model. The size distribution of the crack pattern of the layer of lava solidifying may show the dynamical scaling property just like our result.

The columnar joints of lava result from the fragmentation owing to the thermal contraction when the lava solidifies gradually from the top surface to the bottom. In the columnar joint, it is well-known that the shape of fragment becomes prismal and the sizes of the polygons of the top surface of the fragment seem to be uniform. The dynamical properties of the columnar joint have been investigated well, wheres it seems that the statistical properties have been not investigated well. If the modeling of the fragmentation process of the columnar joint can be realized by our stochastic model, the statistical properties can be understood deeply. For instance, the stochastic process taking the lifetime depending on the size and the aspect ratio into account helps us to understand the reason why the uniformly polygonal structure of the top surface of the fragment is formed.

### Aggregation process

Aggregation process is very ubiquitous phenomena such as the condensation and the particle aggregation in a colloidal suspension. It is important to investigate the statistical properties of the aggregation process. For instance, understanding the size distribution of the particle clusters in the colloidal suspension may be useful to understand the rheological property.

The dynamical scaling property is observed not only in the process of the desiccation crack pattern but also in the aggregation process such as cluster-cluster aggregation (CCA) process [107–111]. CCA is modeled by the random walkers who adhere to each other when they touch each other. The clusters composed of the random walkers distribute spatially, and they grow with time owing to the adhesion (see Fig. 5.8). The dynamical scaling property is observed in not only CCA but also various aggregation processes [112–120].

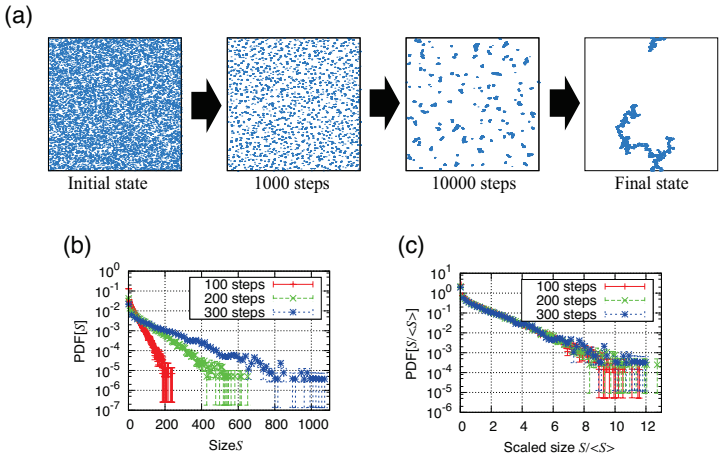


Figure 5.8: (a) Typical time evolution of the growth of the two dimensional CCA pattern. The blue points indicate the random walkers. The random walkers adhere to each other and form the clusters. As time step passes, the big clusters form, and finally one big cluster forms. (b) The time evolution of the raw cluster size distribution. The difference of colors indicates the difference of elapsed time. (c) The time evolution of the scaled size distribution by average size. We can confirm that the dynamical scaling law is obeyed.

Our stochastic model can be applied to the aggregation process. When we model the aggregation process by using the modified Gibrat process, we take into account the increasing ratio instead of the dividing ratio. The "lifetime" in the aggregation process can be interpreted as the characteristic time scale in which the size of cluster grow. Analogizing to our result, because the average size of clusters should increase with time, the lifetime of the clusters should be an increasing function of the size. It is necessary to understand the origin of the lifetime for modeling the aggregation process by the modified Gibrat process.

It is interesting that both the process of the desiccation crack pattern and the aggregation process exhibit the dynamical scaling law even though they are inverse phenomena. Using the modified Gibrat process, we may deeply understand the dynamical scaling property in both cases.

### Other fragmentation and/or aggregation processes

The modified Gibrat process was developed on the basis of the fragmentation process of the desiccation crack pattern. However, it can be applied to other fragmentation and/or aggregation processes by using the lifetimes correspond-

ing to the phenomena. It may be applied to not only the physical problems but also the social problems such as the size distribution of the family name, the municipalities, the wealth, and so on. Measuring the actual lifetime of the objects, we can make the model and analyze it. We hope that the modified Gibrat process is useful for understanding the various material fragmentation and/or aggregation phenomena.

## 5.3 Conclusion

We investigated the dynamical and statistical properties of the desiccation crack pattern. We first reproduced the time evolution of the desiccation crack pattern by performing the SPH simulation of the viscoelastic continuum model, and then we discovered the dynamical scaling property on the size distribution. Next, in order to understand the reason why the dynamical scaling property exists, we proposed the stochastic model on the basis of the Gibrat process. Finally, we carried out the experiment of the desiccation crack pattern of the actual paste in order to compare with our theory. Our main results of this study are as follows:

1. The realistic desiccation crack pattern is reproduced by the computer simulation.

2. The dynamical scaling law of the size distribution is observed theoretically and experimentally.

3. The dynamical scaling law results from the lifetime of the fragment, given by the power function of the size.

We hope that this study contributes the future works of the desiccation crack pattern and helps us to understand other phenomena.

# Acknowledgement

First of all, I am deeply grateful to Prof. Kawamura, Prof. Yukawa, Prof. Yoshino, and members of Kawamura laboratory for useful discussion and support. I could sophisticate and complete my study thanks to their help. I acknowledge Prof. Kitsunezaki, Prof. Ooshida, Prof. Mizuguchi, and Prof. Otsuki for useful discussions. I also acknowledge Prof. Nakahara, Dr. Matsuo, and Mr. Uchida for helpful support of experiment. My experimental studies have been done in Nakahara laboratory. The experimental results make my theoretical studies sophisticated. I also acknowledge Prof. Kikuchi, Prof. Nakashima, and Prof. Nagamine as the examiners of my Ph.D. thesis. Thanks to their advice, my thesis was sophisticated. My work was financially supported by Global COE Program (Core Research and Engineering of Advanced Materials-Interdisciplinary Education Center for Materials Science), MEXT and by Grant-in-Aid for JPSJ Fellows, Japan Society for the Promotion of Science. I am grateful to my family for spiritual support. Lastly, I express my gratitude for all people who I have ever met.

# Appendix A

# The markovianized modified Gibrat process with a constant lifetime

The master equation of markovianized modified Gibrat process with a constant lifetime is introduced in Chap. 2 as

$$\frac{\partial P(S,t)}{\partial t} = -P(S,t) + \int_0^1 \frac{dr}{r} g(r) P\left(\frac{S}{r}, t\right). \tag{A.1}$$

In this appendix, we derive an exact solution of Eq. (A.1) and asymptotic solution with an initial condition, $P(S,0) = \delta(S-1)$.

## A.1 Exact solution

We make a change of variable:

$$x = \log S. \tag{A.2}$$

Then $x$ is defined in the open interval $(-\infty, \infty)$. Equation (A.1) is also transformed to

$$\frac{\partial Q(x,t)}{\partial t} = -Q(x,t) + \int_0^1 dr g(r) Q\left(x - \log r, t\right), \tag{A.3}$$

where $Q(x,t)$ is a function defined as

$$Q(x,t) = P\left(e^x, t\right) e^x. \tag{A.4}$$

The Fourier transformation of Eq. (A.3) respect to $x$ is given by

$$\frac{\partial \tilde{Q}(k,t)}{\partial t} = (w(k) - 1)\,\tilde{Q}(k,t), \tag{A.5}$$

where $\tilde{Q}(k,t)$ is the Fourier transformation of $Q(x,t)$ which is given by

$$\tilde{Q}(k,t) = \int_{-\infty}^{\infty} dx \exp(-ikx)\, Q(x,t), \tag{A.6}$$

and its inverse Fourier transformation is given by

$$Q(x,t) = \frac{1}{2\pi} \int_{-\infty}^{\infty} dk \exp(ikx)\, \tilde{Q}(k,t). \tag{A.7}$$

$w(k)$ is given by

$$w(k) = \int_0^1 dr g(r) \exp(-ik \log r). \tag{A.8}$$

The initial condition of $P(S,t)$ gives the initial condition of $\tilde{Q}(k,t)$ as $\tilde{Q}(k,0) = 1$. Equation (A.5) can be solved easily and its solution is given by

$$\tilde{Q}(k,t) = \exp[(w(k) - 1)\, t]. \tag{A.9}$$

According to the inverse Fourier transformation, Eq. (A.7), the exact solution is given by

$$Q(x,t) = \frac{1}{2\pi} \int_{-\infty}^{\infty} dk \exp[ikx + (w(k) - 1)\, t]. \tag{A.10}$$

As a consequence, $P(S,t)$ is given by

$$P(S,t) = \frac{1}{2\pi S} \int_{-\infty}^{\infty} dk \exp[ik \log S + (w(k) - 1)\, t]. \tag{A.11}$$

## A.2 Asymptotic solution

Let us consider the asymptotic behavior of Eq. (A.11). In order to obtain it, we investigate the asymptotic behavior of Eq. (A.10). First, we derive the average and variance of $x$ by the calculation of the cumulant-generating function. Next, we assume a normalization of the variable using the average and the variance. Then we show that the normalized solution becomes a standard normal distribution under the limit $t \to \infty$. Finally, we show that Eq. (A.11) behaves as a lognormal distribution with $t \to \infty$.

### A.2.1 The moment and the cumulant of the exact solution

Let $c_n$ denote the $n$-th order moment of $x$. $c_n$ is calculated as

$$\begin{aligned} c_n &= \int_{-\infty}^{\infty} dx\ x^n Q(x,t) \\ &= \frac{1}{2\pi}\int_{-\infty}^{\infty} dx\ \int_{-\infty}^{\infty} dk\ x^n \exp\left[ikx + (w(k)-1)\,t\right] \\ &= \frac{1}{2\pi}\int_{-\infty}^{\infty} dk\ \exp\left[(w(k)-1)\,t\right] \int_{-\infty}^{\infty} dx\ \frac{\partial^n}{\partial\,(ik)^n}\exp\left[ikx\right] \\ &= \int_{-\infty}^{\infty} dk\ \exp\left[(w(k)-1)\,t\right] \frac{\partial^n}{\partial\,(ik)^n}\delta(k). \end{aligned} \tag{A.12}$$

Here, according to the formula of the differential of the delta function,

$$\int_{-\infty}^{\infty} dx\ f(x)\frac{d^n}{dx^n}\delta(x) = (-1)^n\ \left.\frac{d^n f}{dx^n}\right|_{x=0}, \tag{A.13}$$

Eq. (A.12) is reduced to

$$c_n = \frac{d^n}{d\,(-ik)^n}\left[\exp\left[(w(k)-1)\,t\right]\right]_{k=0}. \tag{A.14}$$

Furthermore, applying a change of variable $z = -ik$ to Eq. (A.14) and Eq. (A.8), we obtain

$$c_n = \frac{d^n}{dz^n}\left[\exp\left[(W(z)-1)\,t\right]\right]_{z=0}, \tag{A.15}$$

and

$$W(z) = \int_0^1 dr\ g(r)\exp\left[z\log r\right]. \tag{A.16}$$

Let $M(s)$ denote the moment-generating function. Using Eq. (A.15), we obtain $M(s)$ as

$$\begin{aligned} M(s) &= \sum_{n=0}^{\infty}\frac{s^n}{n!}c_n \\ &= \exp\left[(W(s)-1)\,t\right]. \end{aligned} \tag{A.17}$$

The cumulant-generating function $K(s)$ is obtained by using Eq. (A.17) and given by

$$\begin{aligned} K(s) &= \log M(s) \\ &= (W(s) - 1)\, t \\ &= \sum_{n=1}^{\infty} t m_n s^n, \end{aligned} \tag{A.18}$$

where $m_n$ is given by

$$m_n = \int_0^1 dr\ g(r) \left(\log r\right)^n . \tag{A.19}$$

As a result, we find that all cumulants of $x$ are proportional to $t$. Especially, we find that the average $\mu$ and the variance $\sigma^2$ are given by $tm_1$ and $tm_2$, respectively.

### A.2.2 The normalized solution

We consider a normalization of variable as

$$y = \frac{x - \mu}{\sigma}. \tag{A.20}$$

Under the normalization, $Q(x,t)$ is written to the distribution of $y$ as

$$\begin{aligned} R(y,t) &= \sigma Q(\mu + \sigma y, t) \\ &= \frac{\sigma}{2\pi} \int_{-\infty}^{\infty} dk\ \exp\left[ik\left(\mu + \sigma y\right) + \left(w(k) - 1\right) t\right]. \end{aligned} \tag{A.21}$$

### A.2.3 The moment and the cumulant of the normalized solution

Let $\hat{c}_n$ denote the $n$-th order moment of $y$. $\hat{c}_n$ is calculated as

$$\begin{aligned}
\hat{c}_n &= \int_{-\infty}^{\infty} dy\ y^n R(y,t) \\
&= \frac{\sigma}{2\pi}\int_{-\infty}^{\infty} dy\ \int_{-\infty}^{\infty} dk\ y^n \exp\left[ik\left(\mu+\sigma y\right)+\left(w(k)-1\right)t\right] \\
&= \frac{\sigma}{2\pi}\int_{-\infty}^{\infty} dk\ \exp\left[ik\mu+\left(w(k)-1\right)t\right]\int_{-\infty}^{\infty} dy\ \frac{\partial^n e^{ik\sigma y}}{\partial\left(ik\sigma\right)^n} \\
&= \sigma\int_{-\infty}^{\infty} dk\ \exp\left[ik\mu+\left(w(k)-1\right)t\right]\frac{\partial^n}{\partial\left(ik\sigma\right)^n}\delta(k\sigma) \\
&= \int_{-\infty}^{\infty} dl\ \exp\left[il\frac{\mu}{\sigma}+\left(w\left(\frac{l}{\sigma}\right)-1\right)t\right]\frac{\partial^n}{\partial\left(il\right)^n}\delta(l) \\
&= \frac{\partial^n}{\partial\left(-il\right)^n}\exp\left[il\frac{\mu}{\sigma}+\left(w\left(\frac{l}{\sigma}\right)-1\right)t\right]\Bigg|_{l=0},
\end{aligned} \tag{A.22}$$

where we have applied a change of variable $l = k\sigma$ at the second line from the bottom. Here, applying a change of variable $\zeta = -il$ to Eq. (A.22), $\hat{c}_n$ is reduced to

$$\hat{c}_n = \frac{\partial^n}{\partial\zeta^n}\exp\left[-\zeta\frac{\mu}{\sigma}+\left(\hat{W}\left(\zeta\right)-1\right)t\right]\Bigg|_{\zeta=0}, \tag{A.23}$$

(A.24)

where

$$\begin{aligned}
\hat{W}(\zeta) &= \int_0^1 dr\ g(r)\exp\left[\frac{\zeta}{\sigma}\log r\right] \\
&= \sum_{n=0}^{\infty}\frac{\zeta^n}{n!}\frac{m_n}{\sigma^n}.
\end{aligned} \tag{A.25}$$

Therefore, the moment-generating function $\hat{M}(s)$ is given by

$$\begin{aligned}
\hat{M}(s) &= \sum_{n=0}^{\infty}\frac{s^n}{n!}\hat{c}_n \\
&= \exp\left[-s\frac{\mu}{\sigma}+\left(\hat{W}\left(s\right)-1\right)t\right].
\end{aligned} \tag{A.26}$$

Furthermore, the cumulant-generating function $\hat{K}(s)$ is given by

$$\begin{aligned}
\hat{K}(s) &= \log\hat{M}(s) \\
&= -s\frac{\mu}{\sigma}+\left(\hat{W}\left(s\right)-1\right)t.
\end{aligned} \tag{A.27}$$

Here, we investigate the asymptotic behavior of Eq. (A.27). Using $\mu = tm_1$, $\sigma^2 = tm_2$, and Eq. (A.25), we obtain the $s$ series expansion of Eq. (A.27) as

$$\begin{aligned}\hat{K}(s) &= -s\frac{\mu}{\sigma} + \left(\hat{W}(s) - 1\right)t \\ &= -s\frac{\mu}{\sigma} + t\sum_{n=1}^{\infty}\frac{s^n}{n!}\frac{m_n}{\sigma^n} \\ &= \frac{s^2}{2!} + \sum_{n=3}^{\infty}\frac{s^n}{n!}\frac{m_n}{(m_2)^{n/2}}t^{1-n/2}.\end{aligned} \tag{A.28}$$

When $t \to \infty$, the terms of the third and higher order of $s$ are vanished, and then we obtain

$$\hat{K}(s) = \frac{s^2}{2}. \tag{A.29}$$

The form of $\hat{K}(s)$ is equivalent to that of the standard normal distribution. This result implies that, when $t \to \infty$, $R(y,t)$ behaves as the standard normal distribution given by

$$R(y,t) = \frac{1}{\sqrt{2\pi}}\exp\left(-\frac{y^2}{2}\right). \tag{A.30}$$

### A.2.4 The asymptotic behavior of $P(S,t)$

Changing the variable $y$ to $x$, we obtain the asymptotic behavior of $Q(x,t)$ as

$$\begin{aligned}Q(x,t) &= \frac{1}{\sigma}R\left(\frac{x-\mu}{\sigma}, t\right) \\ &= \frac{1}{\sqrt{2\pi}\sigma}\exp\left[-\frac{(x-\mu)^2}{2\sigma^2}\right] \\ &= \frac{1}{\sqrt{2\pi t m_2}}\exp\left[-\frac{(x-tm_1)^2}{2tm_2}\right].\end{aligned} \tag{A.31}$$

Moreover, changing the variable $x$ to $S$, we obtain the asymptotic behavior of $P(S,t)$ as

$$\begin{aligned}P(S,t) &= \frac{1}{S}Q(\log S, t) \\ &= \frac{1}{\sqrt{2\pi t m_2}S}\exp\left[-\frac{(\log S - tm_1)^2}{2tm_2}\right].\end{aligned} \tag{A.32}$$

This result implies that, when $t \to \infty$, $P(S,t)$ behaves as the lognormal distribution just like the original Gibtat process. However, the parameters characterizing the functional form are slightly different.

# Bibliography


[1] J. J. Gilvarry and B. H. Bergstrom, J. Appl. Phys., **32**, 400 (1961).

[2] A. Fujiwara and A. Tsukamoto, Icarus, **44**, 142 (1980).

[3] D. L. Turcotte, J. Geophys. Res., **91**, 1921 (1986).

[4] T. Matsui et al., J. Geophys. Res., **87**, 10968 (1982).

[5] L. Oddershede, P. Dimon, and J. Bohr, Phys. Rev. Lett., **71**, 3107 (1993).

[6] A. Meibom and I. Balslev, Phys. Rev. Lett., **76**, 2492 (1996).

[7] T. Kadono, Phys. Rev. Lett., **78**, 1444 (1997).

[8] H. Katsuragi, D. Sugino, and H. Honjo, Phys. Rev. E, **68**, 046105 (2003).

[9] T. Ishii and M. Matsushita, J. Phys. Soc. Jpn., **61**, 3474 (1992).

[10] J. H. Zhang and M. Xu, Cell Res., **10**, 205 (2000).

[11] E. Villermaux, Annu. Rev. Fluid Mech., **39**, 419 (2007).

[12] A. Tsuchiyama et al., Science, **333**, 1125 (2011).

[13] A. Groisman and E. Kaplan, EPL-Europhys. Lett., **25**, 415 (1994).

[14] C. Allain and L. Limat, Phys. Rev. Lett., **74**, 2981 (1995).

[15] H. Colina and S. Roux, Eur. Phys. J. E, **1**, 189 (2000).

[16] K. A. Shorlin et al., Phys. Rev. E, **61**, 6950 (2000).

[17] N. Lecocq and N. Vandewalle, Eur. Phys. J. E, **8**, 445 (2002).

[18] Z. Néda et al., Phys. Rev. Lett., **88**, 095502 (2002).

[19] S. Bohn et al., Phys. Rev. E, **71**, 046215 (2005).

[20] D. Mal et al., Fractals, **14**, 283 (2006).

[21] D. Mal et al., J. Phys. Soc. Jpn., **76**, 014801 (2007).

[22] S. Sadhukhan et al., J. Phys.-Condens. Mat., **19**, 356206 (2007).

[23] W. Benz, Icarus, **107**, 98 (1994).

[24] F. Kun and H. J. Herrmann, Comput. Method. Appl. M., **138**, 3 (1996).

[25] H. Inaoka and H. Takayasu, Physica A, **229**, 5 (1996).

[26] H. Inaoka, E. Toyosawa, and H. Takayasu, Phys. Rev. Lett., **78**, 3455 (1997).

[27] F. Kun and H. Herrmann, Phys. Rev. E, **59**, 2623 (1999).

[28] F. Wittel et al., Phys. Rev. Lett., **93**, 035504 (2004).

[29] J. A. Åström et al., Phys. Rev. E, **70**, 026104 (2004).

[30] B. Behera et al., J. Phys.-Condens. Mat., **17**, S2439 (2005).

[31] L. Goehring and S. W. Morris, EPL-Europhys. Lett., **69**, 739 (2005).

[32] L. Goehring, S. Morris, and Z. Lin, Phys. Rev. E, **74**, 036115 (2006).

[33] T. Mizuguchi et al., Phys. Rev. E, **71**, 056122 (2005).

[34] A. Toramaru and T. Matsumoto, J. Geophys. Res., **109**, B02205 (2004).

[35] G. Müller, J. Geophys. Res., **103**, 15239 (1998).

[36] G. Müller, J. Volcanol. Geoth. Res., **86**, 93 (1998).

[37] A. Nakahara and Y. Matsuo, J. Phys. Soc. Jpn., **74**, 1362 (2005).

[38] A. Nakahara and Y. Matsuo, J. Stat. Mech-Theory E., P07016 (2006).

[39] M. Otsuki, Phys. Rev. E, **72**, 046115 (2005).

[40] T. Ooshida, Phys. Rev. E, **77**, 061501 (2008).

[41] Y. Hayakawa, Phys. Rev. B, **53**, 14828 (1996).

[42] H. Katsuragi, D. Sugino, and H. Honjo, Phys. Rev. E, **70**, 065103 (2004).

[43] S. Elazzouzi-Hafraoui et al., Biomacromolecules, **9**, 57 (2008).

[44] E. L. Crow and K. Shimizu, *Lognormal Distributions, Theory and Applications* (M. Dekker, 1988).

[45] G. Timár et al., Phys. Rev. E, **86**, 016113 (2012).

[46] P. L. Krapivsky, I. Grosse, and E. Ben-Naim, Phys. Rev. E, **61**, R993 (2000).

[47] K. Yamamoto and Y. Yamazaki, Phys. Rev. E, **85**, 011145 (2012).

[48] G. K. Zipf, *Human Behavior and the Principle of Least Effort* (Addison-Wesley, Reading, MA, 1949).

[49] S. Miyazima et al., J. Phys. Soc. Jpn., **68**, 3244 (1999).

[50] S. Miyazima et al., Physica A, **278**, 282 (2000).

[51] D. H. Zanette and S. C. Manrubia, Physica A, **295**, 1 (2001).

[52] S. C. Manrubia and D. H. Zanette, J. Theor. Biol., **216**, 461 (2002).

[53] X. Gabaix and Y. M. Ioannides, *Handbook of Regional and Urban Economics, Cities and Geography* (Elsevier, 2004).

[54] C. H. Scholz, *The mechanics of earthquakes and faulting* (Cambridge university press, 2002).

[55] J. B. Rundle et al., Rev. Geophys., **41**, 1019 (2003).

[56] H. Kawamura et al., Rev. Mod. Phys., **84**, 839 (2012).

[57] L. A. Adamic and B. A. Huberman, Glottometrics, **3**, 143 (2002).

[58] S. Manrubia and D. Zanette, Phys. Rev. E, **59**, 4945 (1999).

[59] H. Takayasu, A.-H. Sato, and M. Takayasu, Phys. Rev. Lett., **79**, 966 (1997).

[60] K. Yamamoto, Phys. Rev. E, **89**, 042115 (2014).

[61] A. Aydin and J. M. DeGraff, Science, **239**, 471 (1988).

[62] W. Weibull, J. Appl. Mech., **18**, 293 (1951).

[63] E. C. Bingham, *An investigation of the laws of plastic flow* (Govt. Print. Off., 1917).

[64] A. Nakahara and Y. Matsuo, Phys. Rev. E, **74**, 045102 (2006).

[65] S. Kitsunezaki, Phys. Rev. E, **60**, 6449 (1999).

[66] P. Meakin, Thin Solid Films, **151**, 165 (1987).

[67] H. Colina, L. de Arcangelis, and S. Roux, Phys. Rev. B, **48**, 3666 (1993).

[68] A. Nishimoto, T. Mizuguchi, and S. Kitsunezaki, Phys. Rev. E, **76**, 016102 (2007).

[69] S. Sadhukhan et al., Eur. Phys. J. E, **27**, 391 (2008).

[70] S. Kitsunezaki, J. Phys. Soc. Jpn., **79**, 124802 (2010).

[71] A. I. Malkin, A. Y. Malkin, and A. I. Isayev, *Rheology, Concepts, Methods, and Applications* (ChemTec Publishing, 2006).

[72] L. B. Lucy, Astron. J., **82**, 1013 (1977).

[73] R. A. Gingold and J. J. Monaghan, Mon. Not. R. Astron. Soc., **181**, 375 (1977).

[74] J. P. Morris, P. J. Fox, and Y. Zhu, J. Comput. Phys., **136**, 214 (1997).

[75] X. Hu and N. Adams, J. Comput. Phys., **227**, 264 (2007).

[76] J. P. Gray, J. J. Monaghan, and R. P. Swift, Comput. Method. Appl. M., **190**, 6641 (2001).

[77] J. Fang et al., J. Non-Newton. Fluid, **139**, 68 (2006).

[78] M. Müller, D. Charypar, and M. Gross, in *Proceedings of the 2003 ACM SIGGRAPH/Eurographics symposium on Computer animation*, SCA '03 (Eurographics Association, Aire-la-Ville, Switzerland, Switzerland, 2003), 154.

[79] S.-i. Ito and S. Yukawa, Phys. Rev. E, **90**, 042909 (2014).

[80] W. G. Hoover, *Smooth particle applied mechanics, the state of the art* (World Scientific Publishing Co., Inc., 2006).

[81] A. K. Srivastava and P. C. Gope, *Strength of Materials* (PHI Learning Pvt. Ltd., 2013).

[82] J. J. Monaghan, J. Comput. Phys., **82**, 1 (1989).

[83] W. Benz and E. Asphaug, Comput. Phys. Commun., **87**, 253 (1995).

[84] J. Nocedal and S. J. Wright, *Conjugate gradient methods* (Springer, 2006).

[85] A. Jameson and T. J. Baker, AIAA paper 83-1929 (1983).

[86] K. Atkinson, W. Han, and D. E. Stewart, *Numerical Solution of Ordinary Differential Equations* (John Wiley & Sons, 2011).

[87] R. Cruz Hidalgo, Phys. Rev. E, **77**, 061305 (2008).

[88] R. Eymard, T. Gallouët, and R. Herbin, Finite volume methods. *Handbook of Numerical Analysis* (Elsevier, 2000).

[89] F. Bossen and P. S. Heckbert, in 5*th international Meshing Roundtable*, 63 (1996).

[90] B. N. Delaunay, Izv. Akad. Nauk SSSR. Otdel. Mat. Estestv. Nauk, **7**, 793 (1934).

[91] D. Lee and B. Schachter, Int. J. Comput. Inf. Sci., **9**, 219 (1980).

[92] O. C. Zienkiewicz and P. Morice, *The finite element method in engineering science* (McGraw-hill London, 1971).

[93] J. H. Bramble and M. Zlámal, Math. Comput., **24**, 809 (1970).

[94] S.-i. Ito and S. Yukawa, J. Phys. Soc. Jpn., **83**, 124005 (2014).

[95] H. Takahashi and M. Mori, Publ. Res. I. Math. Sci., Kyoto Univ., **9**, 721 (1974).

[96] K. E. Atkinson, *An Introduction to Numerical Analysis (2nd ed.)* (Wiley, New York, 1989).

[97] C. A. Schneider, W. S. Rasband, and K. W. Eliceiri, Nat. Methods, **9**, 671 (2012).

[98] S. Nakashima, J. Mineral. Soc. Japan, **24**, 125 (1995).

[99] S.-i. Ito, Master's thesis, Osaka University (2012).

[100] A. A. Griffith, Philos. T. Roy. Soc. A., **221**, 163 (1921).

[101] S. Kitsunezaki, Phys. Rev. E, **87**, 052805 (2013).

[102] J. B. Dawidowski and A. J. Koolen, Soil Till. Res., **9**, 169 (1987).

[103] M. J. Solomon et al., Macromolecules, **34**, 1864 (2001).

[104] E. Kalnay, *Atmospheric Modeling, Data Assimilation and Predictability* (Cambridge Univ. Press, 2003).

[105] Y. Matsuo and A. Nakahara, J. Phys. Soc. Jpn., **81**, 024801 (2012).

[106] D. R. Jenkins, Int. J. Solids Struct., **46**, 1078 (2009).

[107] W. Wen et al., Phys. Rev. E, **59**, R4758 (1999).

[108] H. See and M. Doi, J. Phys. Soc. Jpn., **60**, 2778 (1991).

[109] M.-C. Miguel and R. Pastor-Satorras, Phys. Rev. E, **59**, 826 (1999).

[110] H. Morimoto and T. Maekawa, J. Phys. A-Math. Gen., **33**, 247 (2000).

[111] J. Černák, G. Helgesen, and A. Skjeltorp, Phys. Rev. E, **70**, 031504 (2004).

[112] T. Vicsek and F. Family, Phys. Rev. Lett., **52**, 1669 (1984).

[113] P. Meakin, T. Vicsek, and F. Family, Phys. Rev. B, **31**, 564 (1985).

[114] D. A. Weitz and M. Y. Lin, Phys. Rev. Lett., **57**, 2037 (1986).

[115] F. Family and P. Meakin, Phys. Rev. Lett., **61**, 428 (1988).

[116] G. Helgesen et al., Phys. Rev. Lett., **61**, 1736 (1988).

[117] M. Y. Lin et al., Nature, **339**, 360 (1989).

[118] J. G. Amar, F. Family, and P.-M. Lam, Phys. Rev. B, **50**, 8781 (1994).

[119] J. G. Amar and F. Family, Phys. Rev. Lett., **74**, 2066 (1995).

[120] N. Yoshioka et al., Phys. Rev. E, **72**, 061403 (2005).

# List of papers

♢ Shin-ichi Ito and Satoshi Yukawa, "Dynamical scaling of fragment distribution in drying paste", Physical Review E **90**, 042909 (2014)

♢ Shin-ichi Ito and Satoshi Yukawa, "Stochastic modeling on fragmentation process over lifetime and its dynamical scaling law of fragment distribution", Journal of the Physical Society of Japan **83**, 124005 (2014)

♢ Shin-ichi Ito and Satoshi Yukawa, "Theoretical study of aspect ratio distribution on desiccation crack patten", in preparation.